GAN-BASED AND HIGH-SPEED METAL -SEMICONDUCTOR-METAL PHOTODETECTOR: GROWTH AND DEVICE STRUCTURES FOR INTEGRATION

A Dissertation
Presented to
the Academic Faculty

By

Sa Huang

In Partial Fulfillment
Of the Requirements for the Degree
Doctor of Philosophy in the
School of Electrical & Computer Engineering

Georgia Institute of Technology
[December, 2003]

GaN-Based and High-Speed Metal-Semiconductor-Metal Photodetector: Growth and Device Structures for Integration

Approved by:

Dr. April S. Brown, Advisor	Dr. Nan M. Jokerst, Advisor
Dr. W. Alan Doolittle	Dr. Ian T. Ferguson
Dr. William T. Rhodes	Dr. Zhonglin Wang

Date Approved ___11/24/2003_____

To our parents, my husband, daughter, and all the families.

ACKNOWLEDGEMENTS

I would like to thank my dissertation advisor, Professor April S. Brown, for her guidance and suggestions during my graduate course. I have learned considerably through her insight into problems. I appreciate her tremendous caring about students. I wish to express my sincere gratitude to Professor Nan M. Jokerst for her financial and spiritual support. I owe a debt of gratitude to Professor W. Alan Doolittle for his helpful discussions and wise advertisement through my research. I would thank Professors Rhodes, Ferguson, and Wang, for their service on my dissertation committee.

I appreciate the help from Gon Namkoong, Sangbeom Kang, Tong-Ho Kim, Changyhun Yi, Greg Triplet, Jeng-Jung- Shen, Terrance Brown, and Sang-woo Seo, who gave me the trainings, intrigued the discussion, and showed me support at the hard times. Special thanks to Walter Henderson for his kind help and discussion.

I would like to thank my friends at Georgia Institute of Technology for their warm friendship. As women Ph.D. students, we went through the journey of graduate school and enjoyed our stay in Georgia together.

I am grateful to my husband, Xin Liu, for his unlimited patience and understanding during the past four years. I cherish the happiness that my little daughter brought to me, and learn a lot from her besides the research. I appreciate the never-ending love, encouragement, and support from my parents. They created good education opportunities for me and sacrificed a lot to complete me. I also appreciate the help from my parents-in-law. I dedicate this thesis to all of my families, for their support.

TABLE OF CONTENTS

LIST OF TABLES

LIST OF FIGURES

SUMMARY

The objective of this research was to design semiconductor material structures for a number of different devices, including GaN metal-semiconductor-metal (MSM), InGaAs/InAlAs MSM, and InAs/GaAs quantum dot photodetectors, and to study the growth conditions for epitaxial material using molecular beam epitaxy (MBE) augmented with an rf-plasma nitrogen source.

GaN was grown on a $LiGaO_2$ substrate, which has multiple advantages over the most commonly used substrates for III-nitride growth. $LiGaO_2$ substrates have a small lattice mismatch of approximately 1% with GaN, which leads to high-quality epitaxy film by optimization of the growth condition. The combination of nitridation, buffer, super lattice, and Ga-rich condition is the key to improving the quality of GaN film grown by MBE on $LiGaO_2$. The first GaN MSM grown on $LiGaO_2$ was reported, which has the dark current in the range of 10^{-12}A. The device was then lift off and bonded on SiO_2/Si wafer. The performance of the device did not degrade after integration.

However, the orthorhombic crystal structure of $LiGaO_2$ results in the unusual asymmetric strains within GaN, causing changes in the microstructure of GaN and making integration difficult. The strains within GaN grown on $LiGaO_2$ were investigated using high resolution x-ray. It was found that the critical thickness of GaN on LGO was around 10nm, and the strains relieve with film thickness increasing. The dislocation densities were also calculated and confirmed by AFM, which can be as low as $2\times10^7/cm^2$.

Through studying of the strains with the insertion of AlGaN/GaN superlattice buffer, it was found that the strain of the epitaxial layer is dependent on the thickness and critical thickness of both epitaxy and buffer layer. For thin GaN films, $Al_{0.12}GaN$ superlattice buffer would relieve the strain most, and for the thicker layers, the $Al_{0.44}GaN$ superlattice buffer relieves the strain most. The dislocation density measurement shows that an insertion of buffer decreases dislocations significantly. Insertion of superlattice buffers does not decrease dislocation density further.

The material structure of InGaAs/InAlAs was studied. The device quality was improved by optimizing the material structure. Depends on the application as optical interconnects, the optimized material structure should insure the device with high speed but reasonable responsivity. Finally, devices were fabricated that achieve speeds as high as 50-70 GHz, comparable with the commercial ultra-fast MSM.

The research of quantum dots was focused on modification of the size, strains, and structures of quantum dots by annealing the spacer between quantum dot layers using As_4 and P_2, respectively, at different temperatures. It was found that the annealing under P_2 results in surface exchange, and the annealing under As_4 mostly changes dots' sizes, causing the changes of energy level.

CHAPTER 1

INTRODUCTION

The objective of this research is to design semiconductor material structures and study the growth conditions for epitaxial material for a number of different device-quality photodetectors. In this thesis, different materials, including GaN, InGaAs/InAlAs, and InAs/GaAs quantum dots, were studied and grown. Due to their different properties, they were fabricated into different types of photodetectors and were assessed, when possible, for integration with Si circuits.

High-speed, high-sensitivity photodetectors have been studied extensively for years [1], because of their applications in broad-band optical communications networks, optical generation of high-power microwave/millimeter waves, future high-speed chip-to-chip interconnections, high-speed sampling, and so on [2]. With the development of novel semiconductor growth and fabrication techniques, as well as the availability of femtosecond lasers, there has been much progress in photodetector technology in the last 30 years [3-5]. Photodetectors have been fabricated with many materials, such as GaAs, InAs, GaN, and Si [6-10]. Metal-semiconductor-metal (MSM) photodetectors have numerous advantages, including their vertical structure and high speed. The history of the MSM photodetector is introduced in Chapter 2. All of the materials in this thesis were grown by molecular beam epitaxy (MBE), a technology that has yielded detectors with high performance. Our objective is to articulate relationships between growth conditions

and device performance and to improve the device performance by optimization of the material structure and growth condition.

GaN photodetectors have been studied extensively in recent years. They are ideal for fabricating UV detectors with a bandgap of 3.4 eV. However, generally GaN photodetectors suffer from high dark currents, dc drift, and slow response time [11, 12]. It is, therefore, a challenge to improve the quality of GaN thin film for this application.

Many difficulties arise in the growth of GaN epitaxial layers because of the use of a highly mismatched substrate, such as sapphire or silicon carbide. $LiGaO_2$ (LGO) is a better lattice-match substrate to GaN [13]. In this thesis, we concentrated first on the improvement of the film quality of GaN on LGO by studying growth conditions, including nitridation, buffer and superlattice structure, and Ga/N flux ratio. The optimization of these conditions is the key to improving the quality of GaN films grown by MBE on LGO. Once high-quality GaN films were produced, MSM devices were fabricated. These were the first published GaN MSM devices on LGO, comparable to the best published GaN MSMs grown on sapphire [14]. The growth conditions and integratability of GaN MSMs are addressed in Chapter 3.

It was found that asymmetric strains existing in the GaN layer impact device integration. The strains within GaN grown on LGO were investigated using high resolution x-ray, as repoted in Chapter 4. It has been found that the asymmetric structure of LGO results in asymmetric strains in GaN. A mathematic model was established to determine the asymmetric lattice constants from x-ray measurement. It was found that the critical thickness of GaN on LGO is ~100Å. This value is much larger than the critical thickness of GaN grown on the other substrates. The growth of elastically strained

material mechanism is different from the plastically strained synthesis as determined by observations of Reflection-high Energy Electron Diffraction (RHEED) during growth. The dislocation densities were calculated by using the William-Hall approach from x-ray measurements, and confirmed by using AFM to count the etch pit density.

AlGaN superlattice buffers improve GaN film quality on LGO, presumably by inhibiting out-diffusion. However, insertion of such superlattice buffers complicates the strains within the film. We found that the strain of the epitaxial layer is not only dependent on its thickness and critical thickness, but also on the thickness and critical thickness of the buffer. These relationships are discussed in Chapter 5.

MSM photodetectors based on the InGaAs-InP material system have been studied over many years for use in long wavelength communications systems. InAlAs/InGaAs has optoelectronic applications at wavelengths of 1.3 and 1.55 μm. These devices hold great promise for optoelectronic integrated circuits (OEICs) [15]. The challenge is to improve the speed of the devices and concurrently maintain low dark current and high responsivity by optimizing the material structure. The relationships between material structure and device properties are discussed in Chapter 6. Finally, fabricated devices were made with speeds as high as 50-70 GHz.

Research on small quantum-dot photodetectors is relatively new. These structures are promising because of their inter-subband transitions of carriers in the infrared (λ= 4-20 μm) range of the optical spectrum [16]. There are many unanswered questions on how the material structures affect the formation of quantum dots and the wavelength, speed, and other characteristics of the devices. The size and density of self-assembled

quantum dots is a very complex topic that is not fully understood. We are exploring quantum-dot structures modified by P_2 anneals to exploit As/P exchange reactions.

More research is needed to optimize structures and growth conditions. We focus on the tuning of inter-subband absorption wavelengths. By annealing the spacer between quantum dot layers using As_4 and P_2 respectively at different temperature, we can modify structures. Photo luminescence (PL) measurement also shows that the energy level is changed. A top AlGaAs barrier is introduced to increase the barrier height. By annealing the AlGaAs top layer with As_4 and P_2 at different temperatures, PL data of the annealed samples are different from the non-annealed one. The theory and history of quantum-dots photodetector, and our experiments and results are described in Chapter 7.

These photodetectors have the differences in wavelength, speed, and material structure. Finally, we conclude in chapter 8 by comparing the integration of GaN MSM and InGaAs MSM. Progress made on quantum dot photodetector is also revived in Chapter 8.

1.1 References:

[1] K. Kato, IEEE Trans. Microwave Theory Tech., **47**, 1265-1281, (1999).

[2] S.Y. Chou, and M.Y. Liu, IEEE, J. of Quantum Electron., **28**, 2358-2368, (1992).

[3] S. M. Sze, D.J. Coleman Jr., and A. Loya, solid-state Electron, **14**, 1209-1218, (1971).

[4] C.H. Lee, Picosecond Optoelectronic Devices. New York: Academinc, (1984).

[5] F.E. Doany, D. Grischkowsky, and C.C Chi, Appl. Phys. Lett., **50**, 460-462, (1987).

[6] O. Wada, H. Hamaguchi, M. Makiuchi, and T. Kumai, J. Lightwave Technol., **LT-5**, 1694-1703, (1986).

[7] M. Ito and O. Wada, IEEE J. Quantm Electron., **QE-22**, 1073-1077, (1986).

[8] D. Soole, H. Schumacher, H.P. Leblanc, R. Bhat, and M.A.Koza, IEEE Photo Technol. Lett. **1**., 250-252, (1989).

[9] D. Soole, H. Schumacher, R. Eesagui, H.P. Leblanc, R. Hhat, and M.A.Koza, Appl. Phys. Lett. **55**, 2173-2175, (1989).

[10] M. Klingerstein, J. Khul, R. Notzel, K Ploog, and J. Rosenzweig etc., Appl. Phys. Lett. **60**, 627-629, (1992)

[11] S.J. Pearton, J.C. Zolper, R.J. Shul, and F. Ren, Appl. Phys. Lett., **50**, 1-78, (1999).

[12] J. C. Carrano, T. Li, P. A. Grudowski, C. J. Eiting, R. D. Dupuis, and J. C. Campbell, Appl. Phys. Lett., **72**, 542-544, (1998).

[13] S. Nakamura, S. Pearton, G. Fasol, The Blue Laser Diode, p12, Springer, (1997).

[14] J.C. Carrano etc., Appl. Phys. Lett., **72**, (1998).

[15] A. Ketterson, J.Seo, M.Tong, K. Nummila and J.Morikuni etc., IEEE Trans. On Electron. Dev. **40**, 1406, (1993).

[16]. I Vurgaftman, Y. Lam, and J. Singh, IEEE J. Quant. Electron., **50**, 14309, (1994).

C H A P T E R 2

OVERVIEW: ORIGIN AND HISTORY OF THE PROBLEM, AND GROWTH AND CHARACTERIZATION TECHNIQUE

For some applications, the optimal properties of all of the components in a substystem may not reside in a single material but in a variety of disparate materials. If different materials are heterogeneously integrated into one system, high performance semiconductor-based electronic and optoelectronic device design can be greatly enhanced.

In 1987 Yablonovitch et al. [45] invented a technique referred to as epitaxial lift-off (ELO), which is based on employing a high-etch selectivity between the substrate and the epilayer. The substrate is etched away; the epilayer is thereby released from the substrate, resulting in a single-crystal, device-quality semiconductor material. The thin films are then placed on a smooth host surface, such as silicon, and adhere through what is termed “Van der Waals bonding”. Water molecules in liquid water are attracted to each other by electrostatic forces, and these forces have been described as van der Waals bonds. The ability to transfer thin films of epitaxial material allows the integration of dissimilar materials without the need to rely on heteroepitaxy.

To create thin film devices for integration, selective chemical wet etching is an excellent non-stress alternative to chemical-mechanical polishing, which can often degrade device performance. In the integration process, the devices are patterned by

photolithography and mesa etched, and the devices are protected from the substrate removal etchant by a handling layer such as wax. The substrate is removed using a wet etch which selectively etches the substrate and not the epilayer. The devices are then bonded to a transfer diaphragm and are aligned and bonded to the host substrate.

Different materials and devices can be bonded into a single substrate system using heterogeneous integration without considering lattice match or chemical compatibility of the different materials. Thus, the best devices suitable for each function can be selected for a single system. The host substrate could be various, depending on the application. III-V and III-N materials can be integrated with advanced Si-based circuits. This combination can increase the performance, decrease the price, and even create a new system.

The application in this thesis focuses on GaN-based UV photodetectors and InGaAs-based high-speed photodetectors integrated with Si host substrates.

2. 1. GaN Growth and MSM Devices

Metal-semiconductor-metal (MSM) photodetectors are important devices because of their high electrical bandwidth, high sensitivity and performance, ability to generate ultra-short electrical pulses, simple processing, and compatibility with large-scale planar integrated circuit technology [1-5]. The MSM photodetectors are photodiodes in which incoming photons create electron-hole pairs that are subsequently separated by an applied electrical field and collected at contacts, thereby creating an electrical current. The implementation of the MSM differs from that of other photodetectors in that it has a

planar rather than a vertical device structure [6]. This is an advantage in applications where the photodetectors must be integrated with amplifiers or emitters [7].

The MSM photodetector is a planar device, made by forming Schottky diodes on a semiconductor layer. Two contact pads and interdigitated fingers form the metal structure and the active area of the device. When a bias voltage is applied to the contact pads, one of the diodes is forward biased and the other reverse biased. The structure is shown in Figure 2.1. The active area of the device is illuminated, and within this region carriers (electron-hole pairs) are generated. The carriers are transported to the contact pads under the applied voltage. Thus, the device detects photons by collecting electric signals generated by photo-excited electrons and holes in the semiconductor, which drift under the electrical field applied between the fingers. The important parameters of the MSM PDs are responsivity, speed, and dark current [8,9]. The relative importance of each parameter will depend on the application, and they are not independent of each other. For instance, by changing the absorbing layer width of a detector whose bandwidth is limited by transit time, one can increase the bandwidth at the expense of responsivity.

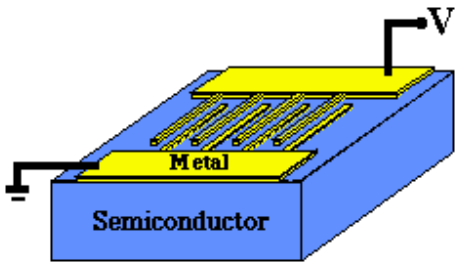

Figure 2.1. Top view of metal-semiconductor-metal photodetector.

Interest in developing ultraviolet (UV) photodetectors is driven by their application in military counter measures, aerospace, automotive, engine monitoring, flame detection, and solar UV detection. Progress in the area of GaN-based materials and devices shows that GaN-based materials have great potential in the area of UV optoelectronics. The leakage currents in GaN are substantially lower than those in GaAs, implying superior signal-to-noise levels and allowing device operation at higher temperatures [10, 11]. Since the first MSM fabricated on GaN with very low dark current was reported by Carrano in 1997 [12], there have been more achievements on n-type and p-type GaN, as well as AlGaN MSM [13-21].

The primary obstacle in developing nitride UV photodetectors has been the significant difficulties in obtaining device-quality material. Noise arising from the background dominates in faint UV observations. Therefore, UV detectors require low dark currents, which result from the defects in the film. It is important to reduce the defects within the film and improve GaN film quality. In the past several years, much progress has been made in developing GaN epitaxial growth techniques and in understanding the properties of GaN material. In the following sections, we introduce improvements in the substrate and growth condition.

2.1.1 The Key Parameters Governing the GaN Film Quality

Many difficulties arise in the growth of GaN epitaxial layers because of the use of a highly mismatched substrate, such as sapphire or silicon carbide. $LiGaO_2$ (LGO) has lattice constants between AlN and GaN, which make it a suitable substrate for the growth of AlGaN. as shown in Figure 2.2.

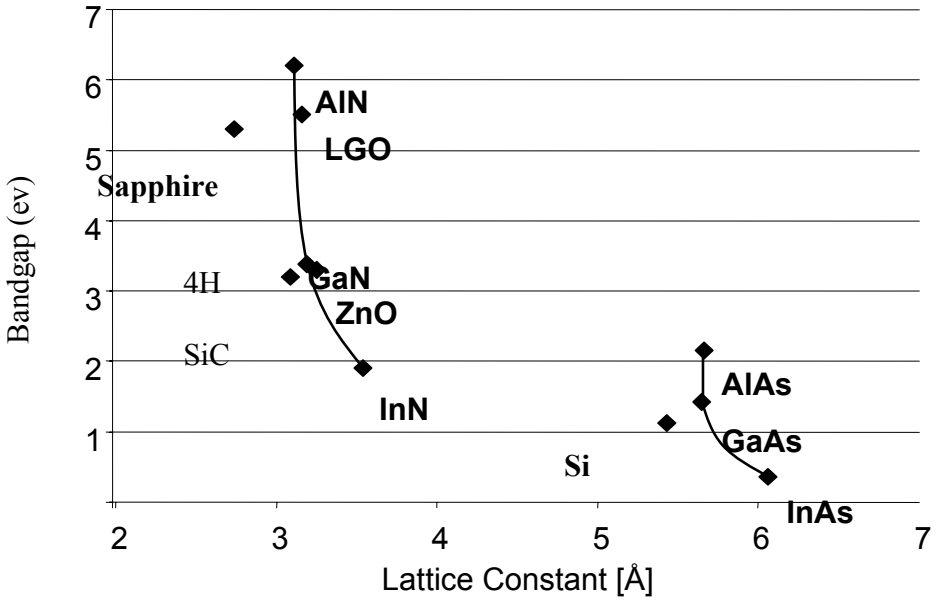

(a)

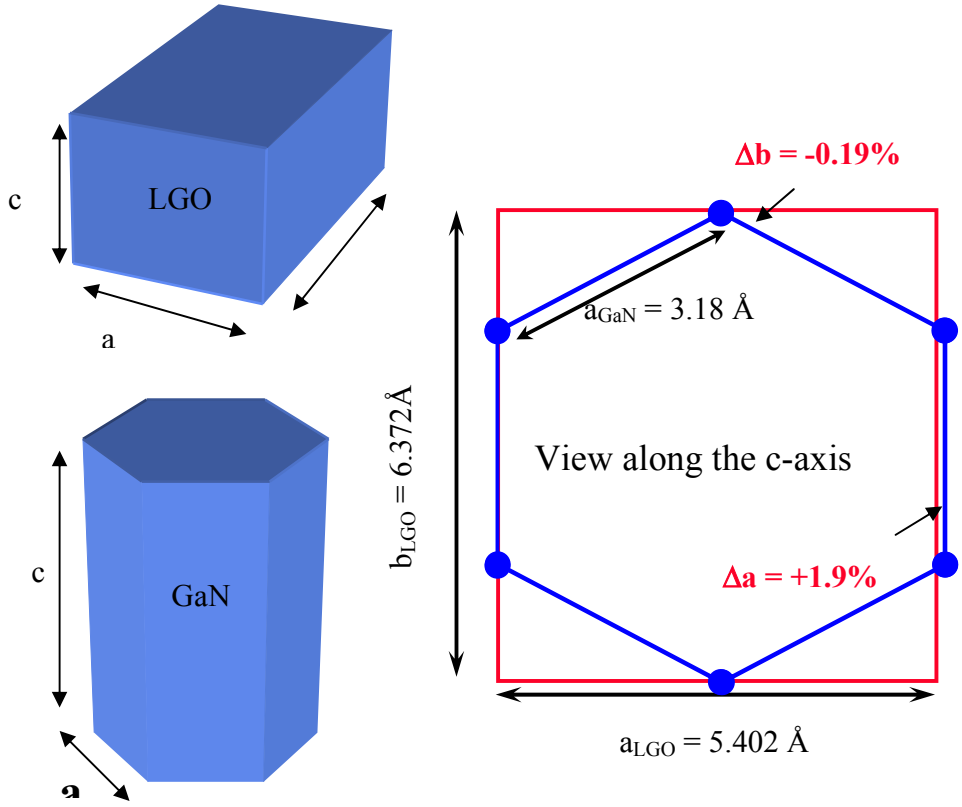

(b)

Figure 2.2 (a) Energy bandgap of compound semiconductors as function of lattice constant [22]. (b)Crystal structure and orientation relationship of GaN to LGO [24].

It is closer lattice-matched to GaN than sapphire, as shown in Figure 2.2 (a) [22]. The crystal structures of GaN and LGO are shown in Figure 2.2 (b) [24]. The average lattice mismatch is approximately 0.9%. LGO processes high resistivity, which reduces parasitic losses in RF circuits. Furthermore, LGO is easily etched in HF, making device integration easier. The structural and electrical properties of LGO have been studied for years [23, 24, 25]. There have been a few reports of FET [26] or MSM devices of GaN grown on LGO [21]. We achieved significant improvements in the GaN synthesis LGO based after studying of the growth conditions.

Many studies had reported that GaN films "peel off" from the LGO after growth and have attributed this phenomenon to poor adherence between the film and the substrate. The adherence also depends on the LGO surface, i.e., on whether growth occurs on the anion (oxygen) or cation surface [24]. Therefore, it is important to understand and investigate the interfacial properties of GaN on $LiGaO_2$ substrates.

Nitridation of the substrate surface before epitaxy has been exploited by many groups. It has been reported that nitridation prevents lithium diffusion into the GaN film [27]. Another report suggests that the nitridated surface of LGO by RF-frequency nitrogen plasma for 3 hours leads to the formation of a 10-20 nm chemically converted layer, which improves the optical and structural characteristics of GaN layers and enhances the lateral growth of GaN [28]. Little data are available on the LGO nitridation process [29]. A systematic investigation of the surface modification of LGO study is processed and reported by our group to optimize the LGO/GaN interface properties in order to avoid the peeling off [30], which will be introduced in Chapter 3.

For GaN grown on sapphire and SiC, a buffer layer must be inserted between the substrate and the active layer to decrease the effect of lattice mismatch between the bulk and substrate and to obtain high-quality GaN films [31,32]. The thickness of the buffer layer should be greater than the critical thickness to release the stress between the substrate and epitaxial film. For the case of LGO, the average lattice mismatch of GaN to LGO is 0.9%, and GaN is nearly lattice-matched along the b-axis of the LGO unit cell. However, it is still necessary to grow a nucleation buffer layer to accommodate the lattice mismatch between GaN and substrate. As a consequence, the buffer condition was also studied in this thesis.

A superlattice layer could stop carriers generated into the substrate from entering the detector active layer, and strained superlattice layers act as barriers for the propagation of threading dislocations originating from the mismatched interfaces [33, 34].

Depending on the effective Ga/N flux ratio, the morphology of the GaN changes dramatically. When the growth proceeds in Ga-rich conditions, the GaN layer becomes compact. While grown near Ga-rich conditions, the entire surface is not flat. Only under conditions of a slight excess of Ga, can very flat films be grown with streaky RHEED patterns, with a dramatic reduction of surface roughness and improvement in structural and electrical properties. If the Ga/N flux ratio is increased, the film is smoother. It should be noted that for high Ga/N flux ratios, the growth temperature should be maintained high enough to re-evaporate excess Ga and thus avoid the formation of Ga droplets. For Ga/N flux ratios less than one, the spotty wurzite transmission RHEED pattern is observed, indicating a three-dimensional surface. N-rich conditions lead to

highly columnar, whisker-like morphologies, independent of the buffer layer and substrate used. The low flux ratio gives rise to a nitrogen-terminated surface, which has a high sticking coefficient for Ga atoms but low surface mobility, and the morphology is rough. The net growth rate is low under these conditions, and the decomposition rate is high. The driving mechanisms seem to be related to the Ga atom diffusion, which is strongly reduced under N-rich conditions. An improvement in crystal morphology and quality can be achieved through a two-step growth method: an initial GaN growth at slow rate under N-rich condition that promotes the coalescence of 3D islands, followed a second step under Ga-rich conditions [35, 36].

The combination of nitridation, buffer, super lattice, and Ga-rich condition is the key to improving the quality of GaN film grown by MBE on LGO. We will study the effects on the quality of film made by these key factors.

2.1.2 Schottky Contact Formation and Fry Etching of GaN MSM

A number of reviews of GaN fabrication progress have been carried out [37, 38]. The measured Schottky barrier heights are, in most cases, a function of the difference between the metal work function and the electron affinity of GaN. For n-GaN, rectifying behavior was observed for Pt, Ni, Pd, Au, and Ti. Pt and Au appear to produce the highest consistent values (~1.0-1.1 eV and 0.91-1.15 eV, respectively) [39, 40], with Ti producing the lowest (0.1-0.6 eV) [41]. Research shows that the barrier height does vary with metal work function. The strategy is therefore to use a metal with a large work function, such as Pt or Au, on GaN to form a Schottky barrier.

There are still large variations in barrier heights reported by different workers for standard metals on GaN. The variability appears to result from the presence of several transport mechanisms, and to materials and process factors, such as 1) defects present in these films, 2) the effectiveness of surface cleans prior to metal deposition, 3) local stoichiometry variations, and 4) variations in surface roughness that could affect uniformity of the results. The influence of the surface cleanliness is obviously most important in determining the quality of the Schottky contact. A number of different acid solutions, including HF/H_2O and NH_4OH have been examined for removing the native oxide, [42, 43], and superior current-voltage characteristics are observed for the resultant rectifying contacts.

In this thesis, dry etching was used to form mesa structures, where high etch rates, anisotropic profiles, smooth sidewalls, and equirate etching of dissimilar materials are required. Inductively coupled plasma (ICP) is a high-density plasma etch system, which has uniform density and energy distributions to maintain fast etch rates with low damage to the surface. The first ICP etch results for GaN were reported in a $Cl_2/H_2/Ar$ ICP generated plasma with etch rates as high as ~6875 Å/min [44]. Etch rates increase with increasing dc bias, and etch profiles are highly anisotropic with smooth etch morphologies over a wide range of plasma conditions.

2.2 Molecular Beam Epitaxy (MBE)

Molecular beam epitaxy (MBE) is the epitaxial growth of compound semiconductor films by the reaction of thermal molecular beams of the constituent

elements with a crystalline substrate surface held at a suitable temperature under ultra-high vacuum (UHV) conditions [46]. The basic elements of an MBE growth system are UHV chamber, substrate heater block, individually shuttered and liquid nitrogen shrouded molecular beam effusion cells, and substrate exchange load-lock system, as shown in Figure. 2.3.

Atomic layer-by-atomic layer deposition is achieved by using low beam fluxes, which are controlled by varying the temperature of the source cells. The atomic mean-free path in the beams is generally larger than the distance between the source and the substrate. Typical growth rates of 0.1-1 μm/hr are obtained. Shutters in front of the sources are used to control growth time. Uniform growth is obtained by rotating the substrate during deposition. In order to obtain low impurity levels, a background pressure of less than 5×10^{-10} Torr is maintained. The UHV environment allows for in-situ monitoring of growth conditions and growth rate by RHEED.

Layer-by-layer epitaxy of lattice-matched materials is possible within a range of growth rates and substrate temperatures. The mechanics of this growth mode are described by the Burton-Cabrera-Frank theory. According to this model, growth proceeds according to the following steps: (1) Atoms impinge on the sample surface, where they are adsorbed, (2) The atoms migrate along the surface towards atomic steps, where they are stabilized by the increased number of atomic bonds, (3) The atoms migrate along the step edges to a kink site, where they are incorporated into the lattice. Deposition involves the lateral motion of step edges or the growth of two-dimensional islands until an atomic layer is completed.

Compared to the more established methods of thin-film growth, the most distinguishing characteristics of MBE are low growth rate, low growth temperature (<1000^{0}C), the ability of abrupt cessation or initiation of growth, a smooth surface of the growing crystal during growth down to atomic steps, and the facility for in-situ analysis [47]. As a result of these favorable features, the MBE technique provides reproducible control over composition, thickness, and doping profile at an atomic scale. In our research, all of the samples are grown by MBE.

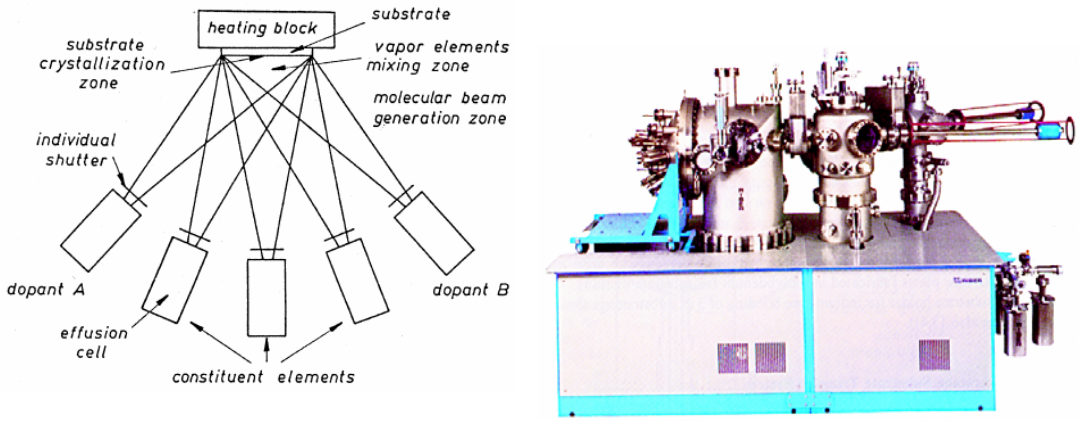

(a) (b)

Figure 2.3. Schematic (a) and out view (b) of a MBE system [46].

2.3 X-ray Characterization

High resolution x-ray (HXRD) is an important tool for analyzing the microstructure of semiconductors. A Philips Materials Research Diffractometer (MRD) X-ray system was used to obtain measurements.

X-ray scattering data were collected with a range of methods on a single diffractometer with exchangeable beam conditioning modules, as shown in Figure.2.4. The sample was mounted on the goniometer, and the data was collected in the high-resolution multi-crystal mode, which is the common method in this thesis for reciprocal space mapping and ω-2θ scans, used to determine film relaxation, defect density, thickness, and composition [48].

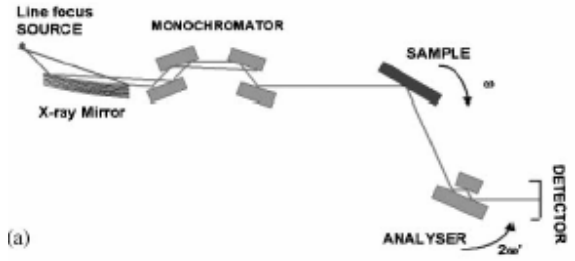

Figure 2.4. Geometrical arrangement of high-intensity multiple-crystal diffractometer for analyzing materials [48].

The x-ray system works by projecting light in the x-ray range on a material. As shown in Figure 2.5, an electron is ejected from its atomic orbit by the absorption of the photon, which should have a greater energy than the energy with which the electron is bound to the nucleus of the atom. When an inner orbital electron is ejected from an atom, an electron from a higher energy level orbit will transfer into the vacant lower energy orbital. During this transition a photon may be emitted from the atom. This fluorescent light is called the characteristic X-ray of the element. The energy of the emitted photon will be equal to the difference in energies between the two orbits occupied by the electron making the transition.

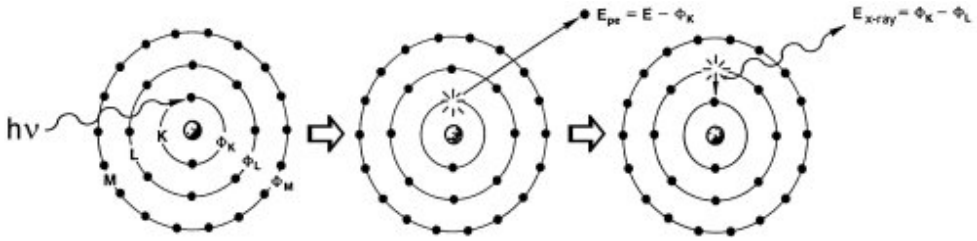

Figure 2.5 Absorption and radiation mechanisms of photon in an x-ray system [49].

For a particular energy (wavelength) of fluorescent light emitted by an element, the number of photons per unit time (generally referred to as peak intensity or count rate) is related to the amount of atoms in the sample. The data for all detectable elements within a sample are usually calculated by counting, for a set time, the number of photons that are detected for the various elements' X-ray energy lines. Therefore, by determining the energy of the X-ray peaks in a sample's spectrum, and by calculating the count rate of the various elemental peaks, it is possible to establish the elemental composition of the sample and to measure the concentration of these elements.

When X-ray radiation passes through crystalline materials, the radiation interacts with the electrons in the atoms, resulting in scattering of the radiation. For the atoms, which are organized in planes and the distances between the atoms are of the same magnitude as the wavelength of the X-rays, constructive and destructive interference will occur, resulting in diffraction where X-rays are emitted at characteristic angles based on the spacing between the atoms. Each atom can belong to many sets of crystal planes. Each set of planes has a specific interplanar distance and will give rise to a characteristic angle of diffracted X-rays. The relationship between wavelength, atomic spacing (d), and angle is the Bragg Equation, as shown in Figure 2.6. Depending on the type of X-ray tube used, with a known illuminating wavelength, the angle can be measured with a

diffractometer, and then the inter planar distance can be calculated from the Bragg equation. A set of d-spaces obtained from a single compound will represent the set of planes that can be passed through the atoms and can be used for comparison with sets of d-spaces obtained from standard compounds.

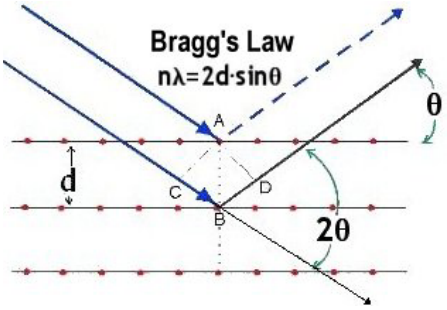

Figure 2.6 X-ray diffraction mechanism [49].

As shown in Figure 2.7, when X-rays are applied to a material's flat surface at grazing angles of incidence, total reflection will occur at or below a certain angle, θ_c, which is called the critical angle and is exceedingly small (less than 1^0). The angle varies depending upon the electronic density of the material. The higher the incident X-ray angle relative to the critical angle, the deeper the X-rays transmit into the material. With a material whose surface is perfectly flat, the reflectivity suddenly decreases at angles above the critical angle in proportion to θ^{-4}. If the material surface is rough, it causes a more dramatic decrease in reflectivity. When the substrate is evenly overlaid with another material having a different electronic density, the reflected X-rays from the interface between the substrate and the thin film as well as from the free surface of the thin film will either constructively or destructively interfere with each other, resulting in an interference induced oscillation pattern. To a first order approximation, the intensity of

lights scattered by a sample is proportional to the square of the modulus of the Fourier transform of the electron density. Thus the electron density profile can be deduced from the measured intensity pattern, and subsequently the vertical properties (layer thicknesses) as well as the lateral properties (roughnesses and correlation properties of interfaces or lateral layer structure) characterizing multilayer can be determined. Specifically, film thickness can be determined from the periodicity of the oscillation and information on the surface and interface from the angular dependency of the oscillation pattern's amplitude.

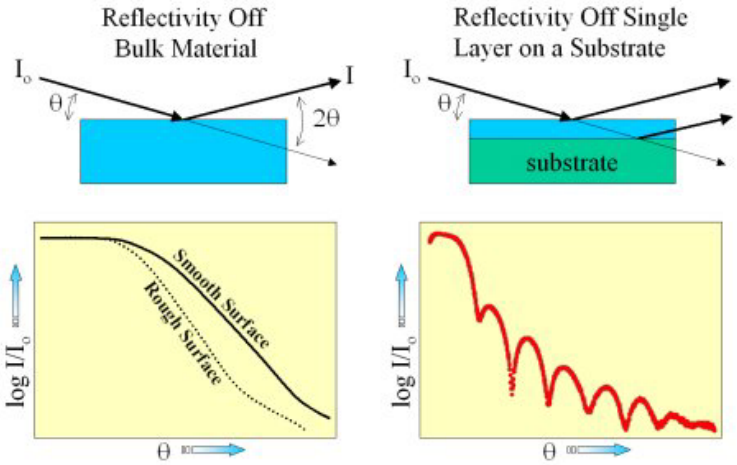

Figure 2.7 Mechanism of x-ray reflectivity to determine the film thickness [49].

In summary, the history and theory of MSM photodetector, the growth of GaN, fabrication progress, MBE system, and x-ray characterization were reviewed in this chapter.

2.4 References:

[1] F. W. Smith, H. Q. Le, V. Diadiuk, M. A. Hollis, A. R. Calawa, S. Gupta, and M. Frankel etc., Appl.Phys. Lett. , **54**, 890-892, (1989).

[2] J. F. Holzman, F. E. Vermeulen, and A. Y. Elezzabi, IEEE J. Quantum Electron. , **36**, 30-136, (2000).

[3] W. Roth, H. Schumacher, J. Kluge, H.J. Geelen, and H. Beneking, IEEE, Trans. Electron. Devices, **ED-32**, 1034-1036, (1985).

[4] B. J. Van Zeghbroeck, W. Patrick, J. M. Halbout, and P. Vettiger, IEEE Electron Device Lett., **9**, 527-529, (1988).

[5] W.C. Koscielniak, J. L. Pelouard, and M.A. Littlejohn, Appl. Phys. Lett., **54**, 567-569, (1989).

[6] O. Wada, H. Nobuhara, H. Hamaguchi, T. Mikawa, A. Tackeuchi, and T. Fujii, Appl. Phys. Lett., **54**, 1617 (1989).

[7] K. Litvin, J. Burm, D. Woodward, W. Schaff, and L. F. Eastman, IEEE Microwave and Millimeter-wave Monolithic Circuits Symp., Atlanta, Georgia, (1993).

[8] Bart J. Van Zeghbroeck, Principles of Electronic Devices 5.32 © Bart J. Van Zeghbroeck (1996).

[9] S. M. Sze, Wiley and Sons, Physics of Semiconductor Devices, 2nd edition,

[10] R. P. Joshi and A. N. Dharamsi, and J. McAeloo, Appl. Phys. Lett., **64** 3611-3613, (1994).

[11] H. Morkoc, S. Strite, G.B. Gao, M.E. Lin, B. Sverdlov, M. Burns, J. Appl. Phys., **76**,1353, (1994).

[12] J. C. Carrano, P. A. Grudowski, C. J. Eiting, R. D. Dupuis, and J. C. Campbell, Appl. Phys. Lett. **70**, 1992 (1997).

[13] Z. C. Huang, D. B. Mott, and P. K. Shu, AIP Conf. Proc. **420**, 39 (1998).

[14] J. C. Carrano, T. Li, P. A. Grudowski, C. J. Eiting, R. D. Dupuis, and J. C. Campbell, Appl. Phys. Lett. **72**, 542 (1998).

[15] J. C. Carrano, T. Li, P. A. Grudowski, C. J. Eiting, R. D. Dupuis, and J. C. Campbell, J. Appl. Phys. **83**, 6148 (1998).

[16] J. C. Carrano, T. Li, D. L. Brown, P. A. Grudowski, C. J. Eiting, R. D. Dupuis, and J. C. Campbell, Appl. Phys. Lett. **73**, 2405 (1998).

[17] D. Walker, E. Monroy, P. Kung, J. Wu, M. Hamilton, F. J. Sanchez, J. Diaz, and M. Razeghi, Appl. Phys. Lett. **74**, 762 (1999).

[18] E. Monroy, F. Calle, E. Muñoz, and F. Omnès, Appl. Phys. Lett. **74**, 3401 (1999).

[19] Z. M. Zhao, R. L. Jiang, P. Chen, D. J. Xi, Z. Y. Luo, R. Zhang, B. Shen, Z. Z. Chen, and Y. D. Zheng, Appl. Phys. Lett. **77**, 444 (2000).

[20] G. Chen, F. Chang, W. Chuang, H. Chung, K. Shen, and W. Chen etc., Jpn. J. Appl. Phys., Part 2 **40**, L660 (2001).

[21] S. W. Seo, K. K. Lee, Sangbeom Kang, S. Huang, W. A. Doolittle, N. M. Jokerst, and A. S. Brown, Appl. Phys. Lett. **79**, 1372-1374 (2001).

[22] S. Nakamura, S. Pearton, G. Fasol, The Blue Laser Diode, p12, Springer, (1997).

[23] S. Kang, W. A. Doolittle, April S. Brown, and Stuart R. Stock, Appl. Phys. Lett. **74**, 3380 (1999).

[24] W. A. Doolittle, Nan M. Jokerst, S. Kang, K. K. Lee, G. May, and A. S. Brown *et al.,* J. Vac. Sci. Technol. B **16**, 1300 (1998).

[25] M. Losurdo, P. Capezzuto, G. Bruno, E.A. Irene, Phys. Rev. B, **58** (1998) 15878.

[26] P. Kung, A. Saxler, X. Zhang, D. Walker, R. Lavado, and M. Razeghi, Appl. Phys. Lett. **69**, 14 (1996).

[27] O. Kryliouk, M. Reed, T. Dann, T. Anderson, and B. Chai, Mater. Sci. Eng. B **59**, 6 (1999).

[28] T. S. Cheng, C. T. Foxon, and S. V. Novikov, *Semiconductors*, **30**, 603, (1996).

[29] D. Kisailus, F.F. Lange, and J. Mater. Res. **16**, 2077 (2001).

[30] M. Losurdo, D. Giuva, G. Bruno, S. Huang, T. Kim, and A. S. Brown, unpublished paper.

[31] H. Amano, N. Sawaki, I. Akasak,i and Y. Toyoda, Appl. Phys. Lett **48**, 353, (1986).

[32] S Nakamura, T. Mukai, and M. Senoh, J. Appl. Phys. **71**, 5543 (1992).

[33] I.J. Fritz, P.L. Gourley, L.R. Daxson, and J.E. Schirber, Appl. Phys. Lett. **53**, 1098 (1988).

[34] N.A. El-masry, J.C.L.Tarn, and S.M. Dedair, Appl. Phys. Lett. **55**,1442, 1989].

[35] O. A., S. K.S. and D. Beresford, *Applied physics Letter*, **65**, p.61-65, (1994).

[36] M.A Sanchez-Garcia., E. Calleja, F.B. Naranjo, F. J. Sanchez, F. Calle, E. Munoz, S. I. Molina, A.M. Sanchez, and F. J. Pacheco, *Journal of Crystal Growth*, **201/202**, p.415-422, (1999).

[37] S. J. Pearton, J.C. Zopler, R.J. Shul, and F. Ren, *Appl. Phys. Rev.,* **86**, p. 1-78, (1999).

[38] J. I. Pankove, *Mat. Sci. Eng.,* **B61-62**, p. 305-309, (1999).

[39] S. N. Mohammad, Z.-F.Fan, W.Kim, O. Aktas, A.E. Botchkarev, A. Salvador, and H. Morkoc, Electron. Lett. **32**, 598 (1996).

[40] R. Sporken, C. Silien, F. Malengreau, K. Grigorov, R. Cauduno, F. J. Sanchez, E. Calleja, E. Munoz, B. Beaumont, and Pierre Gibart, MRS Internet J. Nitride Semicond. Res. 2.23 (1997).

[41] S.C. Binari, H.B. Dietrich, G. Kelner, L.B. Rowland, K. Doverspike, and D. K. Gasill, Electron. Lett. **30,** 909 (1994).

[42]Q.Z. Liu, S.S. Lau, N.R. Perkins, and T. F. Kuech, Appl. Phys. Lett. **69**, 1722 (1996).

[43] N.V. Edwards, M.D. Bremser, T.W. Weeks, R.S. Kern, R.F. Davis, and D.E.Aspnes, Appl. Phys. Lett. **69** 2065 (1996).

[44] R.J. Shul, GaN and Related Materials, edited by S.J. Person , Gordan and Breach, The Netherlands, (1997).

[45] E. Yablonovitch, Phys. Rev. Lett., **58**, 2059 (1987).

[46] E. H. C. Parker, editor. The Technology and Physics of Molecular Beam Epitaxy. Plenum Press, New York, (1985).

[47] K. Ploog, and K. Graf, " Molecular Beam Epitaxy of III-V compounds, Spring-verlag Berlin Herdelberg, New York, (1984).

[48] P.F. Fewster, N.L. Andrew, and C.T. Foxton, Journal of Crystal Growth, **230**, 398-404 (2001)

[49] http://www.rigakumsc.com

C H A P T E R 3

OPTIMIZATION OF GaN GROWTH CONDITIONS AND INTEGRATION OF GaN MSMs

It has been said that the obstacles for GaN MSM are the defects inside the film, which produced noise in the background. The pre-growth and growth conditions need to be optimized to improve the film quality and minimize the defects to further improve the performance of the devices. It was found that a few key parameters affect the film quality, including the substrate preparation, growth temperature, nitridation, buffer, and flux ratio. The study of these parameters will be introduced in this Chapter. The device fabrication process was also studied. The first GaN MSM grown on $LiGaO_2$ was made and integrated as a UV detector.

The primary equipment used in the experiments on the growth of GaN was a Riber 32 MBE system. The nitrogen source was a nitrogen plasma generated by a radio frequency power source. Conventional solid source Knudsen cells are used for the Group III metal sources. The fluxes are measured by an ion flux gauge in units of Torr as beam-equivalent pressure. The substrate temperature was monitored by a thermo-couple and a pyrometer. Surface morphology was monitored during growth by watching the streakiness and the reconstruction of the RHEED pattern. Nitrogen temperature was set at about 4.6×10^{-6} Torr, with a nitrogen flow rate of 0.5 sccm and rf power of 350W.

3.1 Substrate Preparation: Polishing

We chose LGO as the substrate because of reduced lattice mismatch and ease of integration. It has been found that the films grown on the anion side of the substrate peeled shortly after exposure to air. GaN films grown on the cation side of the substrate adhered very well [1, 2]. The determination of the cation face of the LGO substrate is performed by etching the LGO in a buffered solution of PH9.2 that is 0.01 N borate. This solution leads to a faster etch rate on the cation side than the anion side.

The LGO substrates from vendors are two-side polished. However, the surface morphology is not good enough. Under the microscope, some defects are observed over the entire substrate, as shown in Figure 3.1, which result in rough surface morphology of the thin GaN film, as shown in Figure 3.2 (a). The scratches in the film would short the devices in IV measurement or made the integration difficult. The dark current of devices fabricated on such films was very high, indicating high defect densities in the film, as shown in Figure 3.2(b).

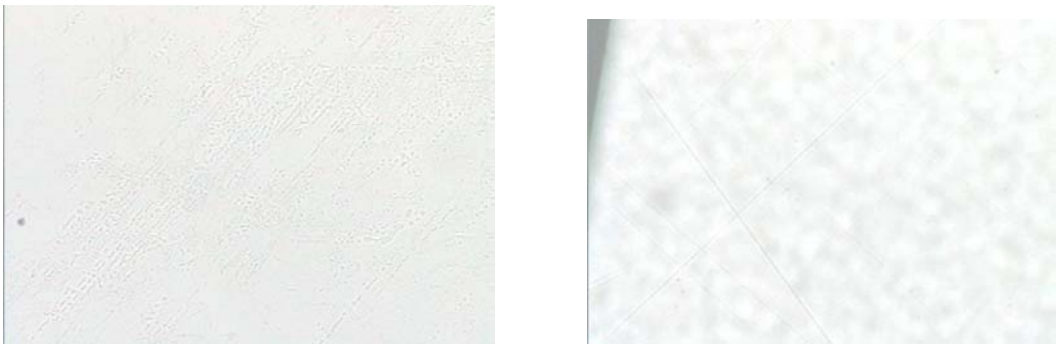

Figure 3.1 Defects on the substrate.

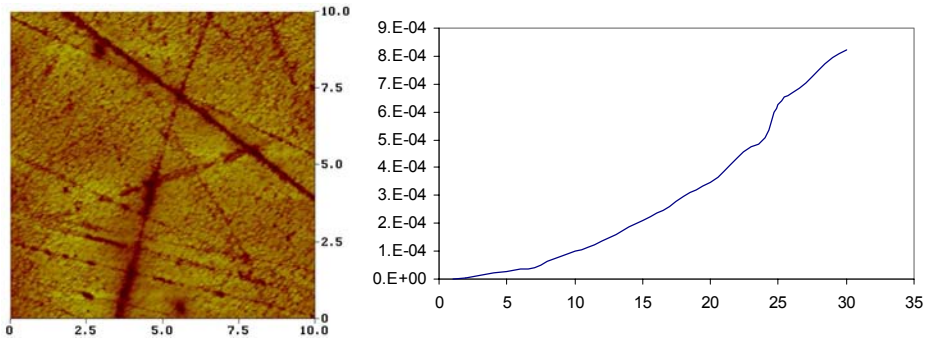

(a) (b)

Figure 3.2 (a) AFM of GaN grown on unpolished LGO with roughness of 6.98nm. (b)Devices fabricated on this film has a very high dark current

We developed a chemical-mechanical polishing procedure to polish the substrates using a 20 inch plate Lap Master Polisher. The solution was a mixture of powder of Al_2O_3 with water. The sizes of Al_2O_3 are 9 μm, 3 μm, 1μm, and 0.3 μm. The polishing process includes five steps, each taking 0.5-1 hour: (1) 9 μm Al_2O_3: H_2O (~30g: 1200ml) (2) 3μm Al_2O_3: H_2O (~20g: 1200ml); (3) 1μm Al_2O_3: H_2O (~30g: 1200ml); (4) 0.3μm Al_2O_3: H_2O (~30g: 1200ml); (5) H_2O: Ethylene Glycol (2:1).

During polishing, the force on the substrate, the rotation speed, and solution ratio are all important. On a 1cm ×1cm substrate, the force was ~1.5kg, the rotation speed was 15 rounds per minute, and the solution ratio was given above. Too much force and excessive speed may cause permanent damage to the surface. Too dense solution results in "orange peel" to the surface (as shown in Figure 3.3). To repair it, the substrate must be re-polished with the particle size larger than the one causing the orange peel and with the correct solution ratio to reduce the surface texture. Less force and solutions will take longer time and more effort to remove the defects.

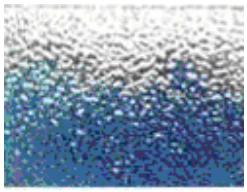

Figure 3.3 Orange peels on the surface caused by too dense solution.

After polishing, the samples were scanned with an atomic force microscopy (AFM). The roughness of the surface could be measured in the range of less than 1 nm. The AFM images of unpolished and polished substrates are shown in Figure 3.4. The surfaces of epitaxial GaN films that were grown on the unpolished and polished substrate respectively are also shown.

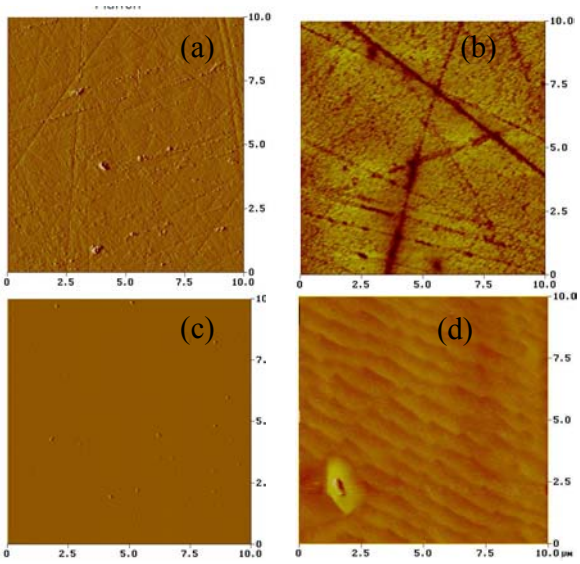

Figure 3.4 AFM images of (a). unpolished LGO substrate, roughness=4.52nm; (b). GaN thin film grown on unpolished LGO, roughness =6.98nm; (c). polished LGO substrate, roughness = 0.04nm; (d). GaN thin film grown on polished LGO, roughness = 0.61nm.

The roughness (RMS) of the substrate decreased from 4.52 nm (unpolished) to 0.04 nm (polished). The GaN films have the same thickness, around 0.3 μm. The roughness of the GaN film decreased from 6.98 nm (grown on unpolished substrate) to 0.61 nm (grown on the polished substrate). These pictures show that polishing not only improves substrate morphology, but also improves film smoothness.

The substrates were cleaned in trichloroethylene, acetone, and methanol. The back surface of the LGO was metalized with a 200 nm Al layer, followed by a 3 μm indium layer for the purpose of uniform heating during the growth. The samples were then mounted on 3 inch silicon wafers in a modified EPI-uniblock sample holder.

3.2 The Optimization of the Growth Condition

As we have mentioned, growth temperature, nitridation, buffer, superlattice, and the ratio of III-V are the important growth conditions to affect growth quality. We have to find the suitable conditions for achievement of high quality film.

3.2.1 Growth Temperature

The lattice constants of GaN and LGO are varied with temperatures. We found that when the film is grown at higher temperatures, the average lattice mismatch between GaN film and LGO is smaller, as shown in Figure 3.5. The lattice constants of GaN are projected on LGO. Thus, the lattice mismatch is calculated as

$$\varepsilon = \frac{a_{LGO} - a_{GaN}}{a_{GaN}} \tag{3.1}$$

where ε is the lattice mismatch between GaN and LGO. This function also works on lattice constant b and c. Growth at temperatures from 590 to 890 ^{0}C was examined to find an optimal growth temperature for GaN growth on LGO. The results showed that at 600^{0}C-700^{0}C, the film has the best crystal quality [2]. This growth temperature is nearly 400 ^{0}C lower than that used for MOCVD-produced GaN of similar structural quality on sapphire, suggesting a potential advantage in producing films containing In and Mg. Generally, In and Mg have relatively low incorporation at high growth temperature due to desorption and phase segregation. The substrate temperature was thus set at 600^{0}C during growth. The temperature was measured by a thermal couple and pyrometer.

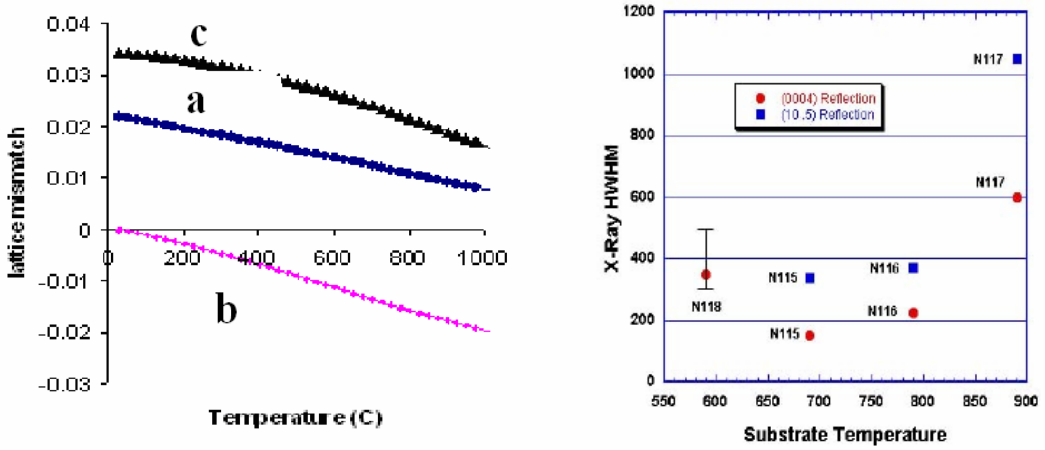

(a) (b)

Figure. 3.5. (a) Lattice mismatch of GaN on LGO as a function of temperature.(b) Symmetric and asymmetric x-ray diffraction FWHM as a function of substrate temperature [3].

3.2.2 Nitridation

Substrate surface pretreatment before nucleation layer growth process is necessary for GaN growth on sapphire to produce device-quality GaN. A report on the nitridation of LGO [4] suggested that the nitridated surface of LGO by rf-frequency nitrogen plasma for 3 hours would lead to the formation of 10-20 nm chemically converted layer, which is speculated to be thin GaN on a Li-Ga-O matrix, or a mixed Li-Ga-ON compound. This layer resulted from the change of surface chemistry, such as replacement of oxygen atoms with nitrogen.

S. Kang has conducted a few experiments varying the nitridation time from 2 minutes to 30 minutes [3]. An EPI nitrogen source was used for this experiment. The nitrogen pressure was set to 4.6×10^{-6} Torr with a nitrogen flow rate of 0.5 sccm and an rf-power of 350 W.

Figure 3.6 (a) shows the O/Ga+Li ratio as a function of nitridation time. The longer the nitridation time, the lower the O-content because of the inclusion and replacement by N. It was also found that during nitridation some Li was lost by Ga-N bonds formation. GaN films were grown on LGO with varying nitridation times under Ga-rich growth conditions after the buffer growth on the nitridated surface. The crystalline quality did not show much variation in X-ray rocking curve measurements. The FWHM values of the x-ray rocking measurements of all the films are in the range of 100 arcsec, as shown in Figure 3.6 (b). Accordingly, the function of nitridation is to reduce impurity diffusing from LGO to the film, but it is not important to the film quality. Therefore, we set the nitridation time at 2 minutes.

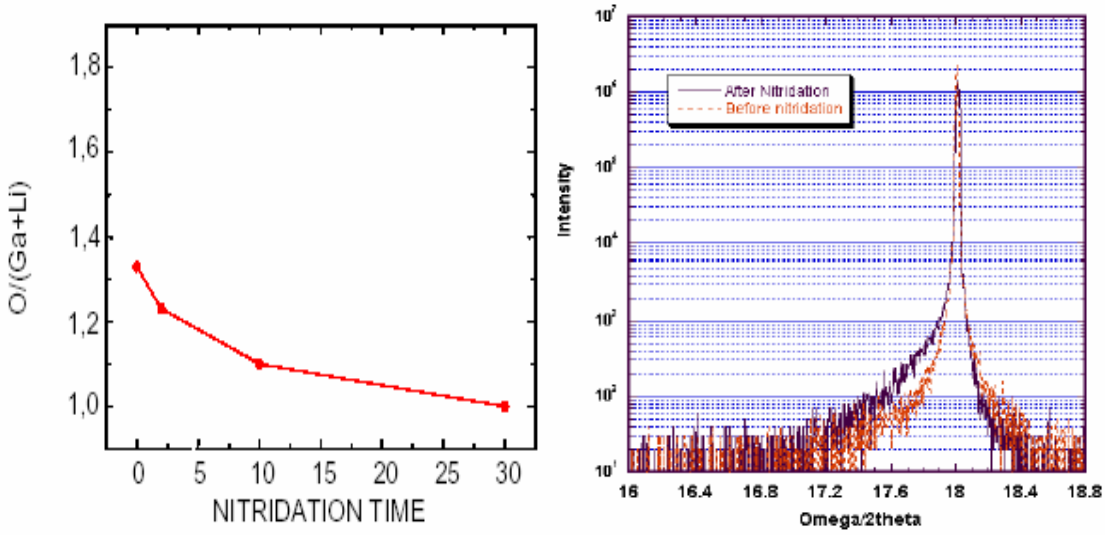

(a) (b)

Figure 3.6 (a) Impurities ratio varied with nitridation time. (b) The x-ray measurements for the film grown with and without nitridation. [3]

3.2.3 Buffer and Superlattices

The buffer was grown as thick as ~16 nm, because from the RHEED observation, the film was relaxed beyond this thickness. Detailed research of GaN buffer is discussed in the next chapter. The superlattice is composed of five periods of AlGaN/GaN. GaN films grown without a buffer and superlattice (SL) layer exhibited high background electron concentration and low resistivity in Hall measurements. The electron concentration of the sample grown without buffer and SL was $1.03\times10^{18}/cm^3$, and the resistance was a few ohms. The electron concentration of the film grown with buffer was as low as $-1.25\times10^{11}/cm^3$, and the resistance was approximately 1MΩ. For the sample grown with both buffer and superlattices, the resistance was too high to measure. The

background concentration was estimated to be roughly $10^{10}/cm^3$. In general, low background electron concentration and high resistivity are required for MSM.

AFM images of above samples are shown in Figure 3.7. All of the samples have the same thickness of 0.4 μm. The first sample grown without a buffer/superlattice has the roughness of 6 nm, the roughest surface. The second grown with a buffer only has the roughness of 1.15 nm. This film shows certain of step-flow growth. The third grown with a buffer, followed by a superlattice, has the roughness of 0.55 nm. It has the smoothest surface among these three samples.

The three samples were scanned with an x-ray along the symmetric (0 0 2) direction. The rocking curves of the 2θ-ω scan are shown in Figure 3.8. The full width at half maximum (FWHM) of the film grown without a buffer/superlattice was 214 arcsecond, the one grown with the buffer only was 50 arcsecond, and the sample grown with a buffer/superlattice was 45 arcsecond. The asymmetric (104) scan showed almost the same trend: N637 has the biggest FWHM value, 360 arc seconds; 220 arc seconds for N902, and 200 arc seconds for N874. The structure and electrical characterization are listed in Table 3.1.

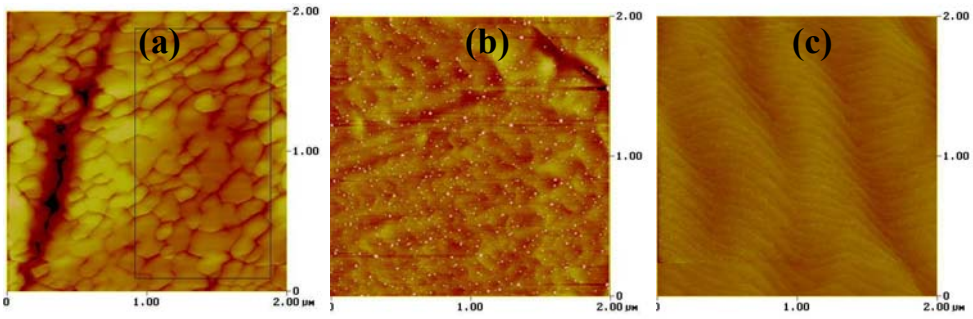

Figure 3.7. AFM images of 0.4μm GaN grown (a) without a buffer/superlattice; (b) with a buffer only; (c) with a buffer/superlattice; (d) the relative rocking curves of the above three samples.

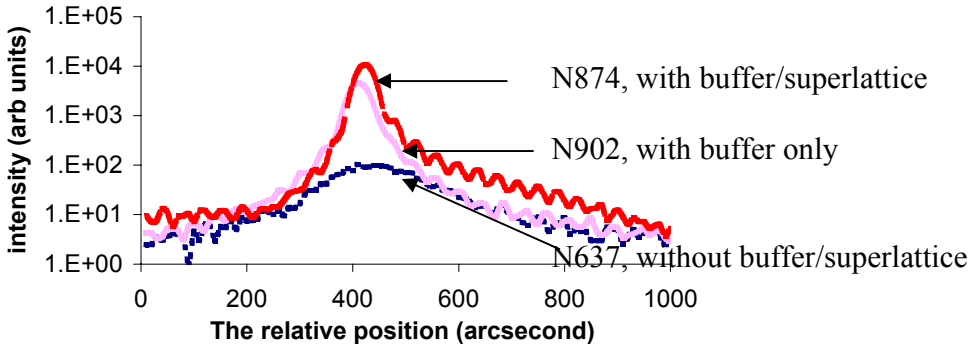

Figure 3.8. Rocking curves of three samples with different buffer/superlattice condition.

TABLE 3.1 Structural and electrical characterization results for the film grown with and without buffer.

Buffer & SL condition	With Buffer/SL	Buffer only	No buffer/SL
Thickness (μm)	0.4 μm	0.4	0.4 μm
Size	1cm×1cm	1cm×1cm	1cm×1cm
Bulk Resistance (Ω/cm)	*	9.77×10^{5}	2.40
Mobility (cm2/vs)	*	51.28	2.54
Bulk concentration (/cm^3)	*	-1.25×10^{11}	-1.03×10^{18}
AFM roughness (nm)	0.55	1.15	6
XRD FWHM (002)	45	50	214
XRD FWHM (104)	200	220	360

*The resistance is too high to measure.

The difference between GaN films grown with and without the buffer is seem to be huge. However, the effect of the superlattice on the crystalline is not obvious from theAFM and x-ray FWHM.

Secondary Ion Mass Spectrometry (SIMS) profiles of the impurities Li, O, and C in the GaN films are shown in Figure 3.9.

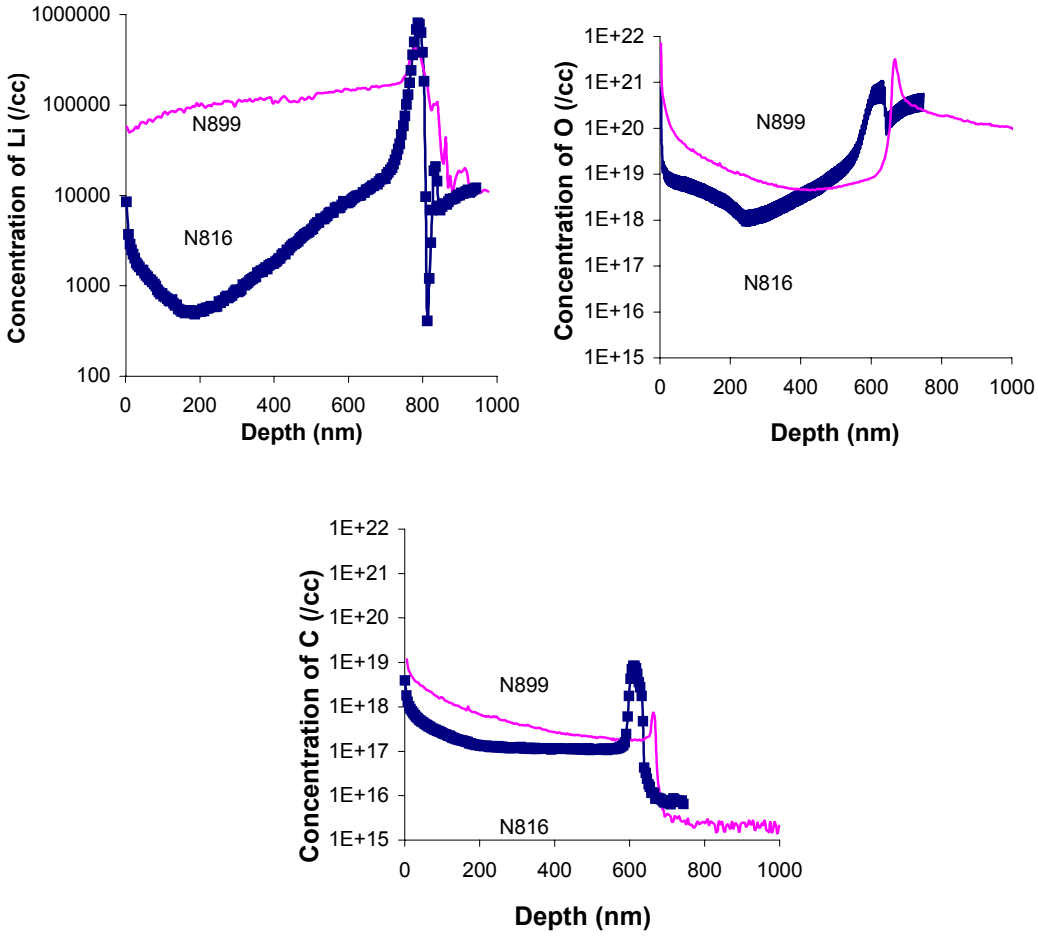

(c)

Figure 3.9. SIMS profile of the impurities inside the films grown with the buffer only (N899) and the one grown with both the buffer and superlattice (N816): (a) Li, (b) O, (c) C.

Both of the samples used in obtaining Figure 3.9 have an epitaxial layer of GaN as thick as ~0.7 μm. N899 was grown on a buffer layer; N816 was grown on a buffer and a superlattice layer. The composition of Li, O, and C is lower inside the film of N816 than in N899. This shows that the superlattice stops the impurities from diffusing from the substrate into the film, while the function of a buffer is to relax the stress. It has been concluded by our group that the buffer thickness should be less than 20 nm. Both the buffer and superlattice are grown under N-rich conditions.

3.2.4 The Ga/N flux ratio and film thickness

The bulk is grown under Ga-rich conditions. As we have noted in Chapter 2, when Ga/N ratio is larger than 1, Ga droplets appeared on the surface of the film, step-flow growth is observed with AFM, and a high-resistivity device is achieved. If the ratio is less than 1, the surface is rough. As shown in Figure 3.10, the GaN film grown under N-rich conditions has a surface roughness of 10.8 nm, while the one grown under Ga-rich conditions has a surface roughness of 0.55 nm.

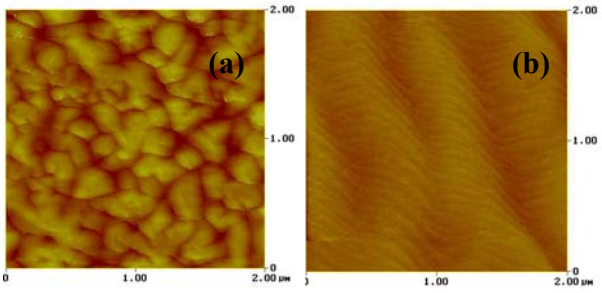

Figure 3.10. AFM of samples grown under (a) N-rich and (b) Ga-rich conditions.

We also grew a series of samples with different thickness. We found that the FWHM decreases when film thickness increases, as shown in Figure 3.11, indicating that the quality of the thicker film is better. Thicker film is also preferable for fabrication and integration. However, it takes a long time to deposit a thick film, and for unknown reasons, thick films are easily cracked on LGO. Therefore, the film thickness for device is targeted at around 1 μm.

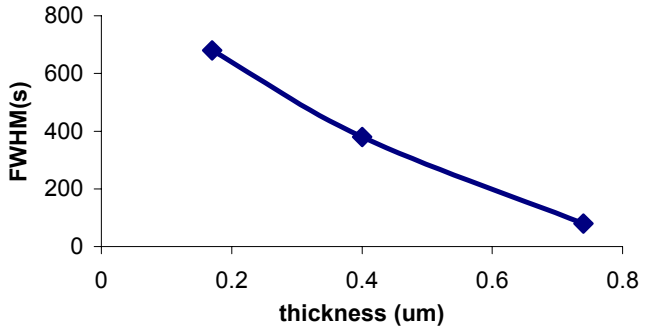

Figure 3.11. The FWHM of x-ray rocking curves vs sample thickness.

Finally, the quality of GaN thin films grown on LGO was significantly improved with the combination of optimized pre-growth and growth conditions: well-polished substrate, 600^0C growth temperature, 2-minute nitridation, buffer and superlattices, Ga-rich epitaxy film, and 0.7-1μm thickness. The estimated dislocation density was about $10^7/cm^2$, and the estimated carrier concentration was $10^{10}/cm^3$. The surface was atomically flat, and the FWHM of asymmetric (104) x-ray scan was 180 arc second, as shown in Figure 3.12.

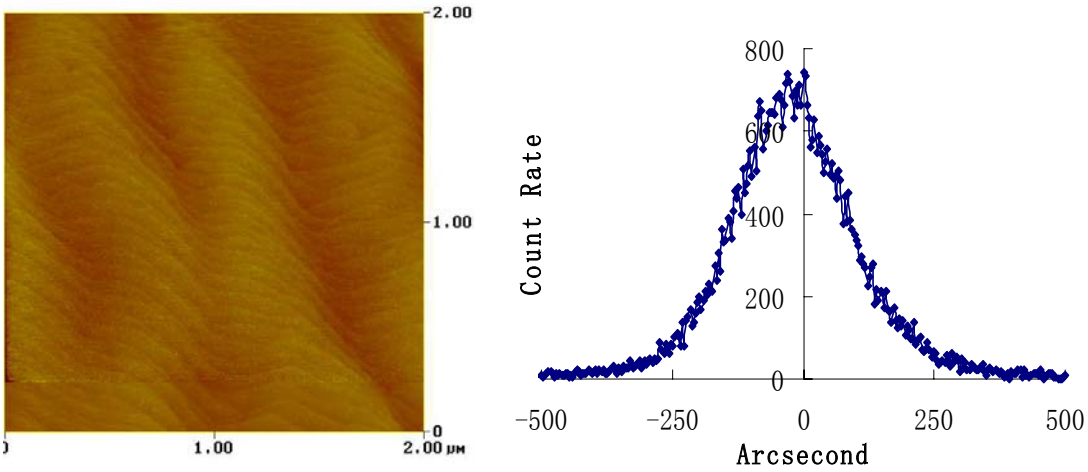

Figure 3.12 AFM image and asymmetric x-ray scan of the sample with optimized growth condition.

3.3 The Fabrication and Integration of GaN MSM

Once high-quality GaN films were produced, the MSM device was fabricated and tested. The interdigitated finger of MSM device was 47 mm long, with 2 mm finger width and 2-10 mm finger spacing, and a detection area of 50 ×50 μm^2. The devices were fabricated using standard photolithography to pattern photoresist for subsequent metallization of metal Schottky contacts on the GaN. Pt and Au were used as the Schottky contacts for their high metal work function, as mentioned in Chapter2, and the good adhesion with GaN. Schottky contacts were 450 Å Pt/1500 Å Au, deposited using electron beam evaporation. A pre-cleaning step was used to remove the oxide on the GaN surface to improve the Schottky characteristics, using hydrofluoric (HF) acid for 1 min and warm ammonium hydroxide (NH_4OH) for 15 min prior to metallization. The cross-section view of the MSM structure and the plane view of a fabricated device are shown in Figure 3.13.

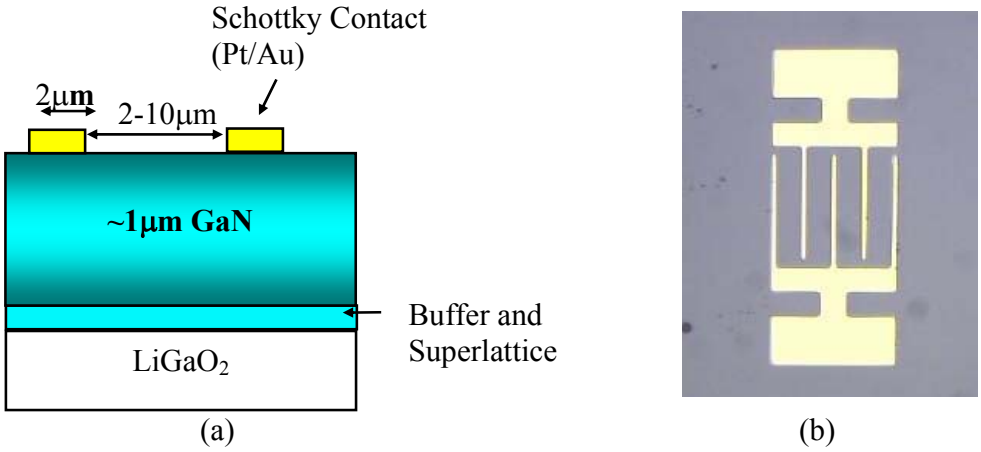

Figure.3.13 (a) Cross view of MSM structure. (b) The fabricated device.

The dark current and photoresponse of the GaN MSMs were measured. A Keithley 617 electrometer was used for measuring the current–voltage (*I–V*) performance of the MSM detector. The measured dark current and photocurrents are shown in Figure 3. 14 The high bias 7.88 pA dark current at a 60 V reverse bias condition is comparable to the best recorded dark current value of 20 pA at 100 V obtained with GaN grown on a sapphire substrate [5]. The 10 V low bias dark current of 0.9 pA is comparable to the best reported low bias dark current of 0.8 pA at 10 V [5].

A 250 W tungsten lamp was used for photoresponse measurements. The light from the source was colliminated and focused onto the MSM using calcium fluoride lenses. A laser line filter with spectral bandwidth at 308 nm was used to filter the incident optical beam. The UV light power density incident on the detector at 308 nm was 24.8 mW/cm^2. The optical system utilized in this study was calibrated with a UV-enhanced Si photodetector and a Newport 1853 optical power meter [6]. The responsivity as a function of applied voltage is shown in Figure 3.14 (b). The measured responsivity values of 0.105 A/W at 20 V and 0.268 A/W at 60 V are also comparable to

the best reported responsivity values of 0.15 A/W at a 10 V reverse bias condition [5]. The dependence of the responsivity data on voltage indicates the existence of photoconductive gain, which is generally attributed to electron tunneling enhanced by hole accumulation and image force lowering at the cathode [7-9].

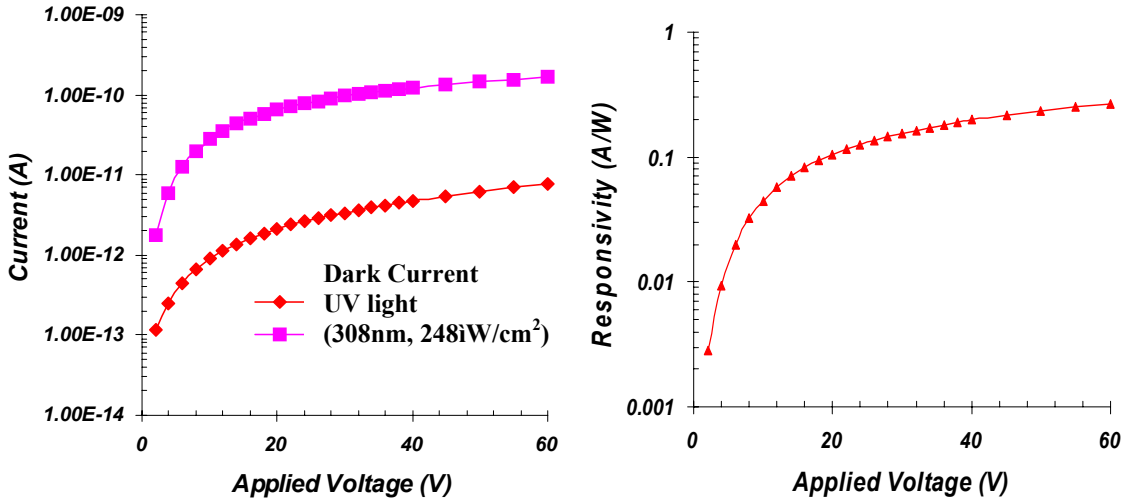

(a) (b)

Figure 3.14 (a) Dark current, photocurrent and (b) responsivity of GaN grown on LGO.

The integration process is shown in Figure 3.15 (a). After device fabrication, the devices were mesa etched by ICP. The gas composition and ratio were: 22.5 Cl_2: 2.5 H_2: 4Ar_2, the etching rate for GaN was ~1000Å per minute with the RF power of 500W, and pressure was 5mτ. The surface was protected in black wax, and the substrate was etched off using a solution of HF:H_2O (1:10), which is selective only to the substrate. The etching rate for LGO of this solution is ~10 μm per minute and for GaN is much less than this value. The devices were then flipped over and bonded on proposed host substrate, Si.

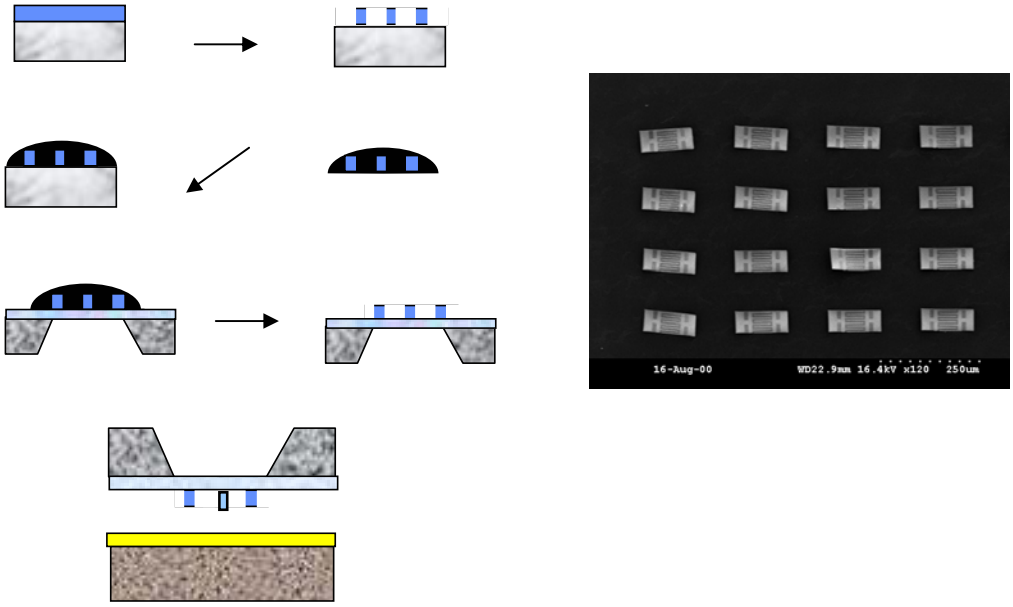

(a) (b)

Figure 3.15. (a) The lift-off process of GaN MSM. (b) SEM picture of device bonded on SiO_2/Si wafer. The maximum device size 50μm × 150 μm, the film thickness was 0.7 μm.

The integration process was performed by Prof. Nan Jokerst's group. The SEM picture of bonding devices is shown in Figure 3.15 (b). From the graph, the bonding devices are seen to be well aligned on the substrate. The maximum device size for successful bonding is 50μm × 150 μm. The Si wafer surface was passivated by coating a SiO_2 layer. The characteristics of bonding devices are shown in Figure 3.16 and are compared with these devices grown on LGO. It shows that the characteristics of the devices after bonding are slightly different from the devices on LGO. When the applied bias is larger than 40 V, the dark current increased slightly higher than before bonding. The property change after bonding may be due to surface states, deep traps in the semiconductor bulk material, or a thin insulating layer between the metal and the semiconductor. The spectral characteristics of the devices were tested and are shown in

Figure 3.17. The photocurrent reached a peak when the wavelength of the incident light was around 360nm, indicating our GaN MSM is a good photodetector in the UV range.

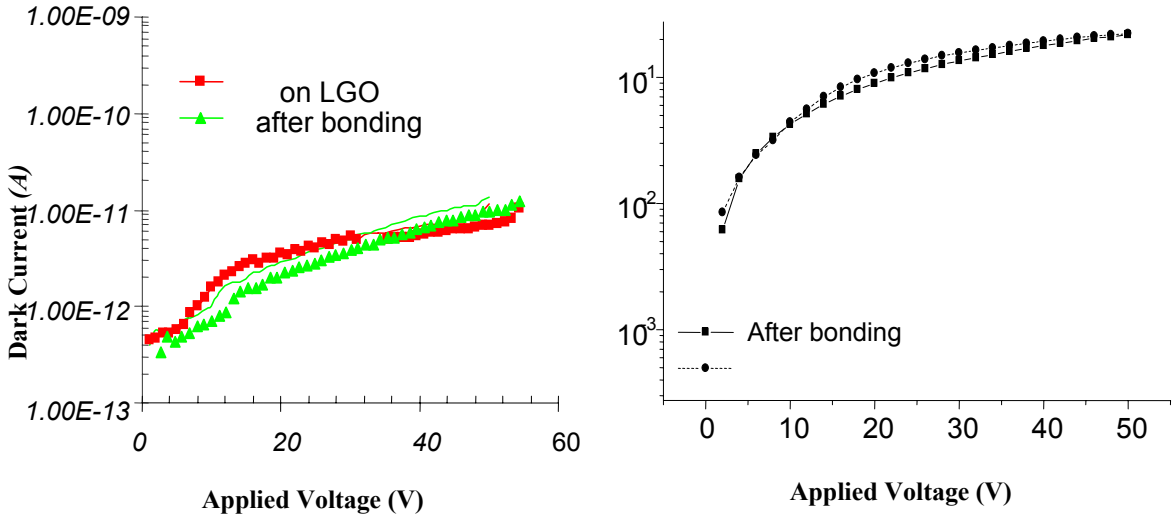

Figure 3.16 Dark current and responsivity of the devices before and after bonding.

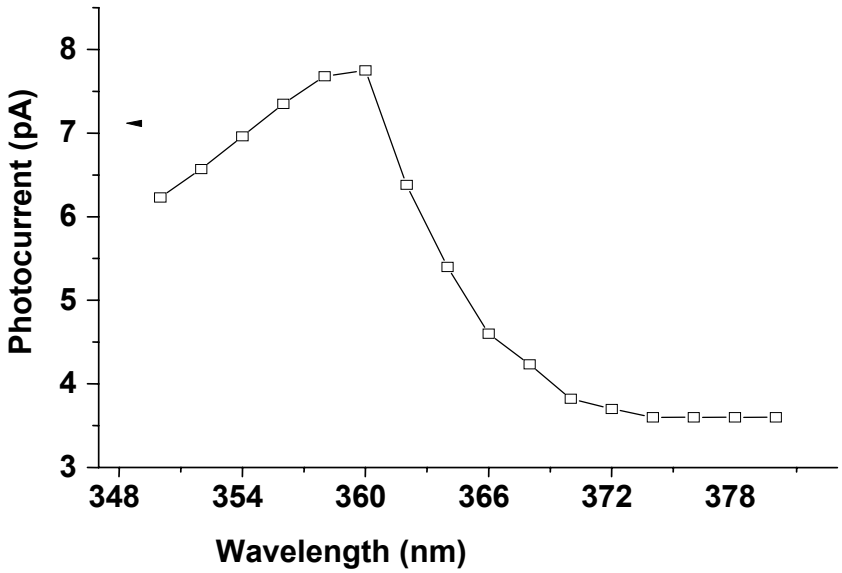

Figure 3.17 Spectral characteristic of GaN MSM versus the wavelength of the incident light.

Finally, the GaN MSM was expected to be integrated into a multispectral imaging system using three-dimensional stacking of photodetectors to detect different wavelengths. One of the approaches of multicolor detection uses intersubband transitions in a stacked series of multiple quantum well detectors, which have multiple detection regions and are voltage tuned to different wavelength sensitivities. The drawback of this kind of photodetector is the difficulty in process technology to electrically contact each independent photodetector to separate the signals for different wavelength.

In summary, the polishing technique on LGO substrate was studied, which significantly improved the film quality. The growth condition of GaN on LGO was optimized. The first GaN MSM on LGO was made and integrated, which has the quality comparable to the best GaN MSM grown on sapphire. The device was applied as UV photodetector.

3.4 References:

[1] T. Kropenwicki, W. A. Doolittle, C. Carter-Common, S. Kang, P. Kohl, A. S. Brown, *J. Elec. Chem. Society*., **45**, L88, (1998).

[2] W. A. Doolittle, S. Kang, T. J. Kropewnicki, S. Stock, P. A. Kohl, and A. S. Brown, *J. Electron. Mater*. **27**, L58, (1998).

[3]. S. Kang, Ph.D. Thesis, "The Epitaxial Growth of GaN and AlGaN/GaN Hetero -structure Field Effect Transistors (HFET) on Lithium Gallate (LiGaO2) Substrates ", (2002).

[4] T. S. Cheng, C. T. Foxon, S. V. Novikov, *Semiconductors*, **30**, 603, 1996.

[5]J. C. Carrano, T. Li, P. A. Grudowski, C. J. Eiting, R. D. Dupuis, and J. C.Campbell, J. Appl. Phys. **83**, 6148 (1998).

[6] S. W. Seo, K. K. Lee, Sangbeom Kang, S. Huang, William A. Doolittle, N. M. Jokerst, and A. S. Brown, Appl. Phys. Lett. **79**, 1372-1374 (2001).

[7]K. S. Stevens, M. Kinnibugh, and R. Beresford, Appl. Phys. Lett. **66**, 3518, (1995)

[8] S. F. Soares, Jpn. J. Appl. Phys., Part 1 **31**, 210, (1992)

[9] J. Burm and L. F. Eastman, IEEE Photonics Technol. Lett. **8**, 113 (1996).

C H A P T E R 4

ASYMMETRIC STRAIN AND MICROSTRUCTURE CHARACTERIZATION OF GaN ON $LiGaO_2$

Much research has reported the primary factors that influence the growth of device-quality GaN films. $LiGaO_2$ (LGO) is a useful substrate for GaN because of its smaller lattice mismatch in comparison to sapphire and SiC. However, it has been found that after thin-film integration, devices can delaminate and curl in one direction (as shown in Figure 4.1.), indicating that there must be strain in the film. There are three potential sources of strain: metallization-based stresses introduced in fabrication, internal stress gradients resulting from GaN microstructure, and thermal stress resulting from the thermal expansion differences between the LGO and GaN. A group at the University of Wisconsin has done some research on the first stress and found that the metallization-based stress was not significant [1]. And since the substrate has been lifted off, the thermal stress should not be counted for the reason to cause the curl. Our research focused mainly on the second potential source.

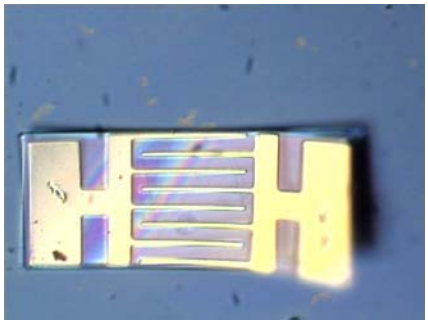

Figure 4.1 Curled lift-off device.

It is therefore important to characterize the lattice constants of GaN for different film thicknesses and to obtain the stress and strains in the structure and the related critical thickness. By definition, when the epilayer is thicker than the critical thickness, the mismatch strain is partially or fully relaxed through the introduction of dislocations. The lattice mismatch between GaN and AlN is about 3%, larger than that between GaN and LGO (1% for average), and the critical thickness of GaN on AlN is only 3 nm [2]. Thus, a larger critical thickness of GaN on LGO was expected because of the significantly smaller lattice mismatch of GaN on LGO, and it offers a unique opportunity to examine growth kinetics on elastically strained thin GaN films.

The determination of strains in semiconductors needs either rocking curves or reciprocal space maps [3]. The rocking curve method assumes that the lattice parameters of the substrate provide a good reference, whereas the reciprocal space maps can be analyzed on a similar relative scale or absolute scale. The advantage of the latter approach is that the substrate distortions and uncertainties in the substrate database values are irrelevant, and it is particularly important for heavily relaxed layers. Fewer defects are assumed to be introduced into GaN thin films due to the smaller lattice mismatch

between GaN and $LiGaO_2$ than that between GaN and sapphire. The strains and dislocation density were analyzed in this chapter. The analysis was dependent on the high-resolution x-ray measurement.

4.1 Experiment and Characterizations of GaN on LGO

The crystal structures of GaN and LGO are shown in Figure. 2.1. GaN has a symmetric hexagonal structure, whereas LGO has an asymmetric orthorhombic structure. The asymmetry of the crystalline structure of LGO results in an asymmetry of the strains in GaN, which complicates the analysis. This asymmetry in strain is technologically significant for the substrate removal and epitaxial lift-off processes [4] utilizing GaN grown on LGO in that it introduces bending in only one direction.

GaN thin films with thicknesses from 5 nm to 1 μm were grown on LGO by molecular beam epitaxy (MBE). A Philips MRD X-ray system was used to obtain measurements from multiple reflections, allowing the film lattice constants to be calculated. The LGO was polished prior to growth to achieve a smooth surface. The roughness of the surface after polishing was typically less than 1 nm. The substrates were solvent cleaned before loading into the MBE system. Six samples were grown at a temperature of 600^0C. The temperature was determined by a thermocouple and pyrometer. A two-minute nitridation preceded the initiation of growth. The thicknesses of the samples were 5nm, 10nm, 15nm, 20nm, 50nm, and 1μm. For the first five thin samples, the Ga flux was 7×10^{-8} Torr, significantly within the N-rich growth regime. The thicknesses of these samples were determined from glancing angle x-ray reflection data, which is accurate to within ±0.5 nm for a 5 nm film. The reflectivity x-ray measurement

for the 50nm sample is shown in Figure 4.2. The final 1μm sample was grown with a Ga flux of 4×10^{-7} Torr, known to yield a slightly Ga-rich growth condition in our system. The thickness of this thicker sample was measured with a profilometer, with an error of ±0.015μm. Since the growth temperature is the same in all cases, the thermal expansion mismatch is identical in all samples.

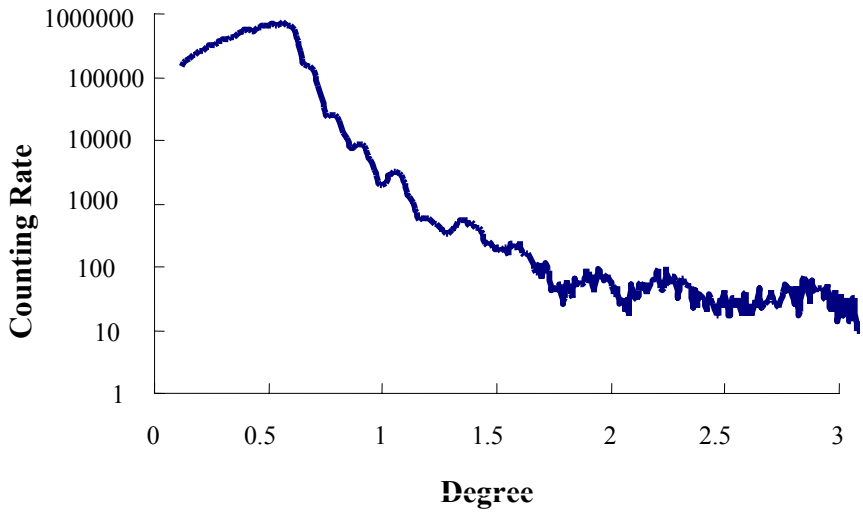

Figure 4.2. Reflectivity measurement of GaN, from which a thickness of 50nm was obtained.

The X-ray 2θ-ω curves of these six samples are shown in Figure 4.3 for the (0002) reflection. The distances between the GaN peak and the LGO peak are different for different thicknesses, indicating that the strains are different. When the film is 1 μm, the film is relaxed, as evidenced by the peak separation consistent with bulk GaN and bulk LGO. Because of the small lattice mismatch between LGO and GaN, the FWHM is ~60 arcsec along (002) direction for the 1 μm sample, with ~180 arcsec for the (104) asymmetric peak. These data also highlight the significance of LGO as the substrate for

GaN growth: a relatively thick film can be grown before relaxation, allowing elastically strained GaN to be investigated.

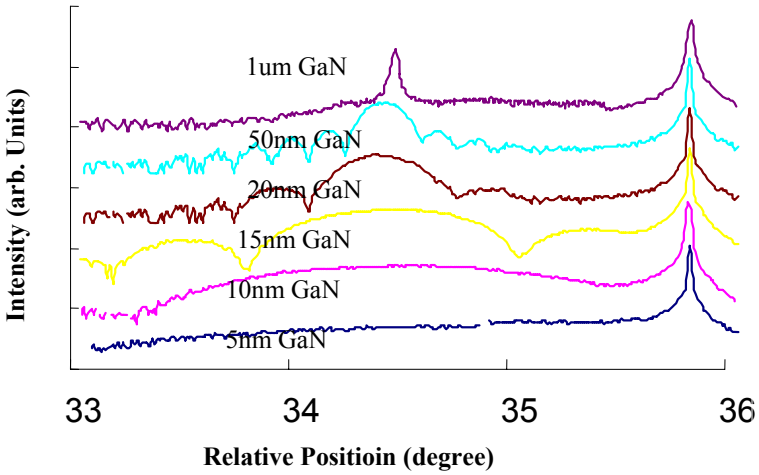

Figure 4.3. X-ray Rocking curves of GaN grown on LGO with different thicknesses.

One method for determining the overall strain in a layer is to measure in-plane (a) and perpendicular (c) lattice constants via a reciprocal space map (RSM) [5]. A two-dimensional map of the diffraction intensity at each lattice point is obtained from a series of coupled ω-2θ scans at incrementally increasing values of ω. The lattice constants for a Bragg reflection (h k l) are calculated using the following relationship:

$$a = \frac{\lambda}{2Q_x}\sqrt{\frac{4}{3}(h^2 + k^2)} = \frac{\lambda}{2Q_x}\tan 30^0 \quad \text{(h k l) = (1 0 3, 1 0 4, 1 0 5)}$$
$$c = \frac{l\lambda}{2Q_y} \quad \text{(hkl)= (0 0 2, 0 0 4, 0 0 6)} \qquad (4.1)$$

where Q_x, is the in-plane component of reciprocal lattice vector, Q_y is the vertical component of reciprocal lattice vector, λ is the wavelength of x-ray, which is 1.5406Å in

the present case. Reflections from $\{1\ 0\bar{1}5\}$ and {0 0 0 2) family planes were used due to their strong intensity. However, Equation. 4.1 is useful for the symmetric hexagonal structure only.

The (001) plane of LGO possesses a quasi-hexagonal structure with slight asymmetry in bond-angle and atomic distance from a perfect hexagonal structure. The strains between the GaN film and the substrate create asymmetry in the GaN atomic displacements. Thus, the peak positions in the RSM obtained from reflection of each member of $\{10\bar{1}5\}$ family plane are not the same. Accordingly, the asymmetric strain that is present in the GaN film grown on LGO can be expressed by looking at the GaN peak position dependence on each reflection from the $\{10\bar{1}5\}$ family plane. As shown in Figure 4.4, an in-plane vector, v, was determined from the x-ray measurement along $\{10\bar{1}5\}$ direction, using this equation:

$$v = \frac{\lambda}{2Q_x} \qquad (4.3)$$

The strained GaN structure is half symmetric, resulting in two vectors that are the same, indicated by v_{-2}, and four vectors that are the same, indicated by v_{-4}. The angles between the vectors, φ, is not 60^0. Equation (4.1) is for the hexagonal structure and is thus not strictly suitable for calculating in-plane lattice constants in the present case. Since the angles between the vectors experimentally determined from our experiments are different from 60^0 by less than 1 degree, the error associated with this deviation from the ideal case is statistically insignificant. Thus, the lattice constants could be calculated from the vectors and the angles. The calculation process is shown in the Appendix.

Finally, using the procedure outlined in the appendix, the two-fold symmetric in-plane lattice constants of GaN, labeled a_{-2}, and four-fold symmetric lattice constants, a_{-4}, were calculated. It is noted that lattice vectors v_{-2} and v_{-4} are measured quantities whereas lattice constants a_{-2} and a_{-4} are calculated quantities dependent on the measured lattice vectors v_{-2} and v_{-4}. Lattice constants a_{-2} are related to the strain within GaN along the b direction of the LGO. Vectors v_{-2} are related to the strain along the direction of a-axis. Lattice constant c is calculated from Equation. (4.2).

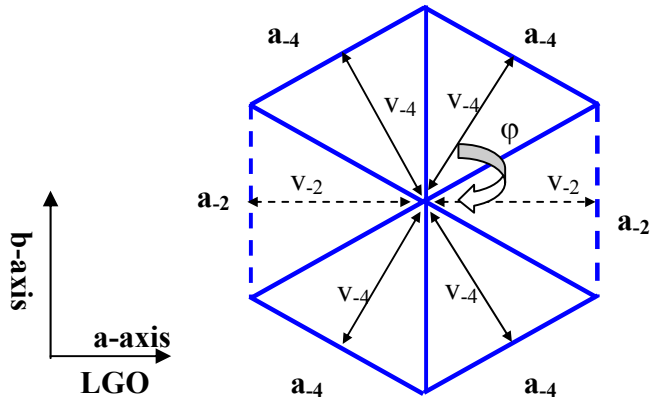

Figure 4.4. Schematic showing definitions of lattice vector and lattice constants of GaN, in which φ indicates the angle between the two vectors, which is not 60^0 in an asymmetric structure.

The resultant asymmetric strain in GaN is due to both lattice mismatch and thermal expansion. The lattice constants of GaN and LGO from recent published papers are listed in Table 4.1 [6,7]. The average coefficients of thermal expansion (CTE) of GaN and LGO from growth temperature to room temperature are listed in Table 4.2. The strain in the GaN layer caused by the difference in thermal expansion between the substrate and GaN is calculated from [8]:

$$\varepsilon = (\alpha_{LGO} - \alpha_{GaN}) \times (T_{GT} - T_{RT}) \tag{4.4}$$

where α_{LGO} and α_{GaN} are the CTE of LGO and GaN, shown in Table 4.2. From this equation, we obtain the thermal strain: $\varepsilon_a = 0.5\%$, $\varepsilon_b = 0.9\%$, $\varepsilon_c = 0.51\%$.

TABLE 4.1. The published lattice constants of GaN and LGO at room and growth temperature [6,7].

	LGO			GaN			
	a (Å)	b (Å)	c (Å)	a (Å)	$2a\cos 30^0$ (Å)	2a (Å)	c (Å)
RT (298K)	5.407	6.379	5.011	3.1880	5.521	6.376	5.186
GT (900K)	5.451	6.455	5.048	3.197	5.538	6.395	5.199

TABLE 4.2. The calculated CTE of LGO and GaN in the temperature range of 298K-900K.

α (10^{-6}/K) / Material	α_a	α_b	α_c
GaN [2]	5.11	5.11	4.47
LGO [3]	13.56	19.86	10.7

4.2 Asymmetric Strain in Elastic Strained and Plastically Deformed GaN Resulting from a Substrate without Planar Symmetry

The calculations of lattice constants of the GaN films are plotted in Figure 4.7 as a function of thickness. In all data, the values of fully strained and fully relaxed GaN at room temperature is also shown taking into account the CTE effect on lattice constants. When the GaN film is fully strained at room temperature, the lattice constants should be equal to that of LGO. When the GaN film is fully relaxed, the lattice constants are 3.188 Å [6]. However, a film fully relaxed at the growth temperature is strained due to the thermal mismatch strain. The fully relaxed lattice constant is thus calculated from the fully relaxed value of GaN and LGO at the growth temperature modified by the thermal strain, by $a=a_0-a_s\times\varepsilon$ where a_0 is the lattice constant of GaN, a_s is the lattice constant of the substrate, and ε is the CTE. Therefore, after cooling to room temperature, the fully relaxed lattice constant of GaN would be $a_{-2GaN} = 3.1615$ Å, $a_{-4GaN} = 3.1702$ Å.

The resulting lattice constants depend slightly on which Bragg peaks are used in the calculation as well as on the accuracy of the experiment, which is determined to be less than 0.4%. The 4-fold symmetric and 2-fold symmetric lattice constants are not exactly the same, resulting in an experimental error less than 0.3%. Finally, as indicated in the Appendix, our calculation neglects an error in the angle variation (less than a degree) resulting in an error less than 0.15%. Thus, the overall error in the measurement of the lattice constants was determined to be less than 0.85%. The thicker films have lower errors.

In setting up the experiment, the LGO $\{1\ 0\bar{1}5\}$ peak was also scanned to confirm the identity of the GaN peak, which is usually about 3^0 (2ω) away from the GaN peak as was previously determined [9]. Figure 4.5 shows the reciprocal maps of 15nm GaN along the direction of v_{-2} (left) and v_{-4} (right). It has been found that the relative peak positions

of GaN to LGO were different along different directions. Along the direction of v_{-2}, the GaN peak is on the left side of the LGO peak, indicating a tensile strain existed. Along the direction of $v_{-4,}$ GaN is on the right side, indicating a compressive strain.

Figure 4.6 shows the average peak positions in reciprocal maps for vectors v_{-2} and v_{-4} respectively. The peak positions for LGO and fully relaxed GaN are also shown.

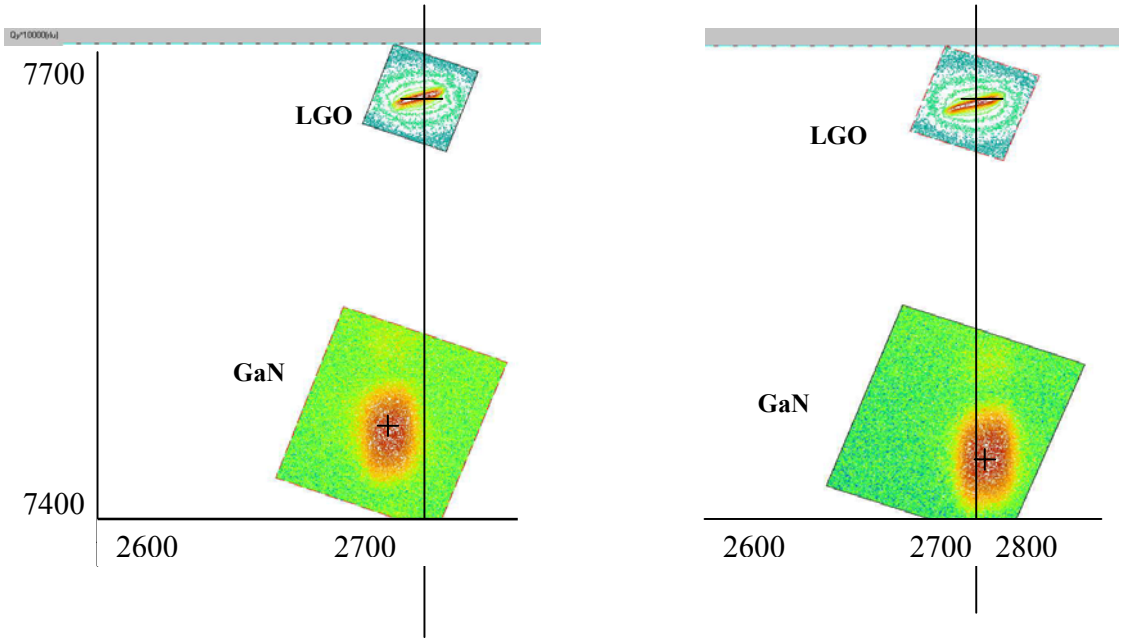

Figure 4.5 Reciprocal space maps of 15nm GaN on LGO along v_{-2} (left) and v_{-4} (right).

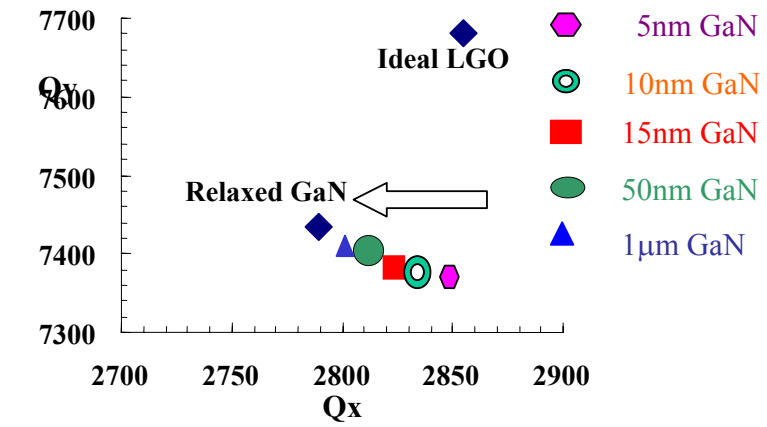

(a)

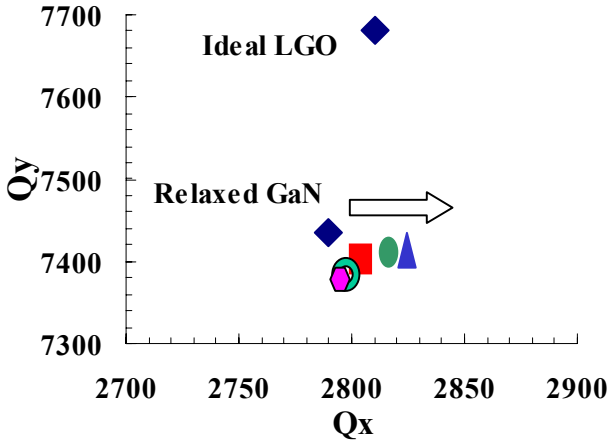

(b)

Figure 4.6 $\{1\ 0\ \bar{1}\ 5\}$ reciprocal lattice points of LGO and unstrained GaN are marked with ◆, and the measured peak positions for GaN with the thickness from 5nm to 1μm for v_{-2} (a) and v_{-4} (b).

From the relative peak position of GaN to LGO, we could identify the peaks and determine v_{-2} and v_{-4}. Also shown are the measured peaks for all samples. The Q_X value of all the epitaxial GaN films are larger than those of unstrained GaN, it is noted that both v_{-2} and v_{-4} are smaller than that of fully relaxed GaN, indicating that there exists residual compressive strain in all GaN films along both the a-axis and b-axis of LGO. The Q_Y values for the strained GaN peak positions at any rotational angle are almost the same

and smaller than that of unstrained ideal GaN, implying that the perpendicular lattice parameter c of GaN is independent of rotational position and larger than that of unstrained GaN owing to the tensile expansion in the c-axis direction due to the compressive in-plane strain.

The calculations of lattice constants of the GaN films are plotted in Figure 4.7 as a function of thickness. In all data, the values of fully strained and fully relaxed GaN at room temperature is also shown taking into account the CTE effect on lattice constants. When the GaN film is fully strained at room temperature, the lattice constants should be equal to that of LGO. When the GaN film is fully relaxed, the lattice constants are 3.188 Å [6]. However, a film fully relaxed at the growth temperature is strained due to the thermal mismatch strain. The fully relaxed lattice constant is thus calculated from the fully relaxed value of GaN and LGO at the growth temperature modified by the thermal strain, by $a=a_0-a_s\times\varepsilon$ where a_0 is the lattice constant of GaN, a_s is the lattice constant of the substrate, and ε is the CTE. Therefore, after cooling down to room temperature, the fully relaxed lattice constant of GaN would be $a_{-2GaN} = 3.1615$ Å, $a_{-4GaN} = 3.1702$ Å.

From Figure 4.7 (a), the in-plane lattice constant $a_{-2,GaN}$ is close to the strained value of GaN when the film thickness is less than 15nm. The lattice constant decreased with increasing film thickness as expected. Furthermore, when the film thickness is 1 μm, the lattice constant is close to the relaxed value, which indicates that the film is almost fully relaxed at this thickness. From Figure 4.7 (b), the other in-plane lattice constant, $a_{-4,GaN}$, increased with increasing the film thickness. When the film is thin, $a_{-4,GaN}$ is closed to the fully strained value of 3.1702 Å. However, it is close to the relaxed value when the film thickness is 1μm.

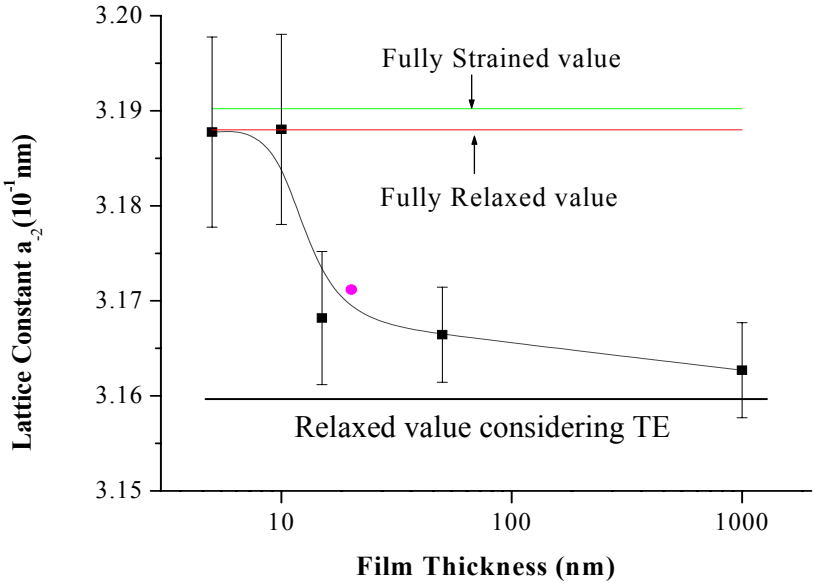

(a)

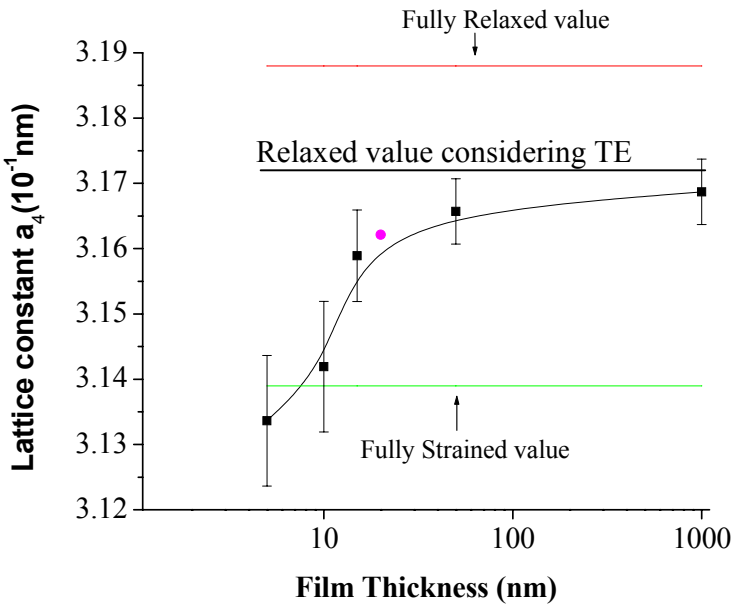

(b)

Figure 4.7 Lattice constants (10^{-1}nm) versus film thickness (nm). (a) lattice constant a_{-2}, (b) lattice constant a_{-4}.

When the film is strained, the lattices along the b-axis are extended and the lattice along the a-axis is compressed (see Figure 2.2), causing different changes of lattice constants along two different directions. Thus, when film is relaxed, the lattice constant a_{-2} is shorter compared with the strained lattice constant a_{-2}; the lattice constant a_{-4} is longer compared with the strained lattice constant a_{-4}.

Figure 4.8 shows the out-plane lattice constant c decreases with increasing the film thickness toward the relaxed value, as expected.

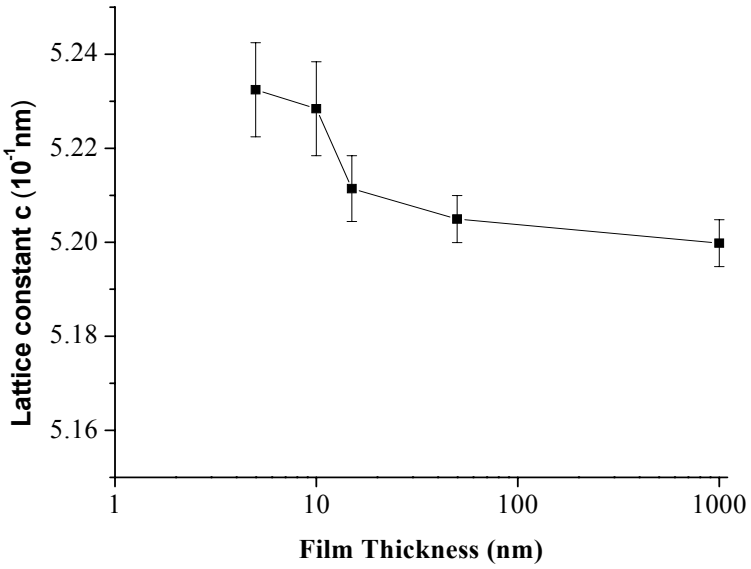

Figure 4.8 Lattice constant c versus film thickness.

The filled circle in Figure 4.7 (a) and (b) is the thickness/lattice constant of the sample where growth was halted when the RHEED pattern transitioned from a streaky, two-dimensional growth mode pattern at the beginning of the growth to a spotty pattern, indicating that the growth became three dimensional, as shown in Figure 4.9. The growth was terminated when the RHEED pattern became spotty. X-ray measurements indicated

that the film has partially relaxed with a thickness of ~20 nm. This relaxation behavior is similar to that observed for GaAs, indicating that strain plays a key role in the surface morphology of the initial GaN nuclei. Additionally, it is noted that the GaN grown under extremely N-rich conditions is normally highly faceted on other highly mismatched substrates resulting in a very spotty RHEED image. Contrarily, GaN elastically grown N-rich on LGO shows a smooth RHEED pattern, indicating a significantly different growth mode for elastically strained material (before relaxation occurs) verses plastically deformed material (after relaxation). Additionally, a very weak 2x2 reconstruction is observed in the elastic regime even for extremely N-rich growth conditions. Clearly the elastically grown GaN has significantly different growth kinetics than its plastically-deformed counterpart.

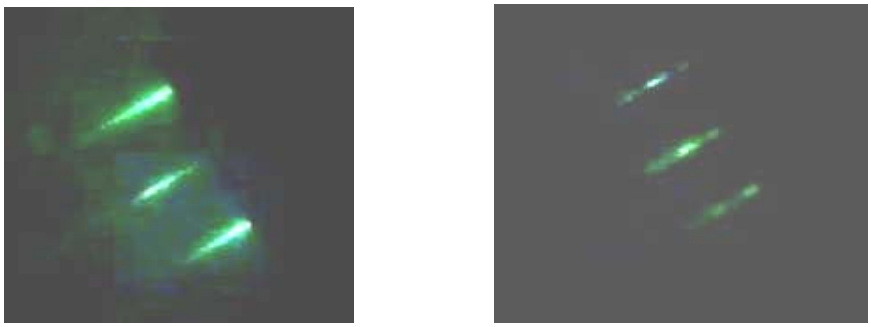

(a) (b)

Figure 4.9. RHEED pattern of GaN on LGO, (a) at the beginning of the growth, (b) when the film thickness is 20nm.

In thermodynamic equilibrium, misfit dislocations appear at the interface of strained layer heterostructures, when the strained layer is thick enough that it is energetically favorable for the mismatch to be accommodated by a combination of elastic

strain and interfacial misfit dislocations, rather than by elastic strain alone. Therefore, when the film is below the critical thickness, GaN is expected to grow pseudomorphically on LGO. Above the critical thickness, the strain begins to relax by spontaneous creation of dislocations at the GaN/LGO interface. Subsequently, the lattice constant begins to approach the bulk value as the thickness of GaN increases further.

There have been many papers that define and determine critical thickness [2, 10-12]; however, most of them are based on a symmetric substrate. If we assume the difference resulting from the asymmetric structure is small in comparison to a symmetric structure, we can use the equations that relate lattice constant and critical thickness. A functional form based on Van der Merwe's equilibrium theory is given by[1]:

$$a_{GaN} = a_0 + \frac{h_c}{h}(a_{LGO} - a_0) \qquad (4.5)$$

where a_0 is the lattice constant of unstrained GaN considering the thermal strain, h is the thickness of the film, and h_c is the critical thickness. Therefore, h_c could be obtained from this function and a fit of data given as the solid line through the data points in Figure 4.7 (a) and (b). The critical thickness derived from such a fit results in $h_c = 93 \pm 10$Å. All data for the fit are within the calculated error for this experiment.

Another simple equation which expresses the relation of h_c with lattice constant was derived by Fischer [11]:

$$\frac{(a_0 - a_{LGO})}{a_{LGO}} = \left(\frac{b\cos\delta}{2h_c}\right) \times \left(1 + \frac{1-(\gamma/4)}{4\pi(1+\gamma)\cos^2\delta}\right) \ln(h_c / b) \qquad (4.6)$$

where δ is the angle between the Burgers vector and the direction in the interface, which is equal to $\pi/3$; γ is the poison's ratio, 0.38; and b is the Burgers vector, which is taken to

be 3.084Å from reference [12]. The theoretical critical thickness of GaN based on equation 6 is 102 Å for $a_{-4,GaN}$, which is in agreement with our result.

Figure 4.10 shows the volume of GaN crystal calculated from our lattice constant at different thicknesses. The volume of a solid is constant independent of the applied stress. Considering the error, the calculated volumes are within a reasonable range. This supports the assertion that our measurements and calculations are consistent.

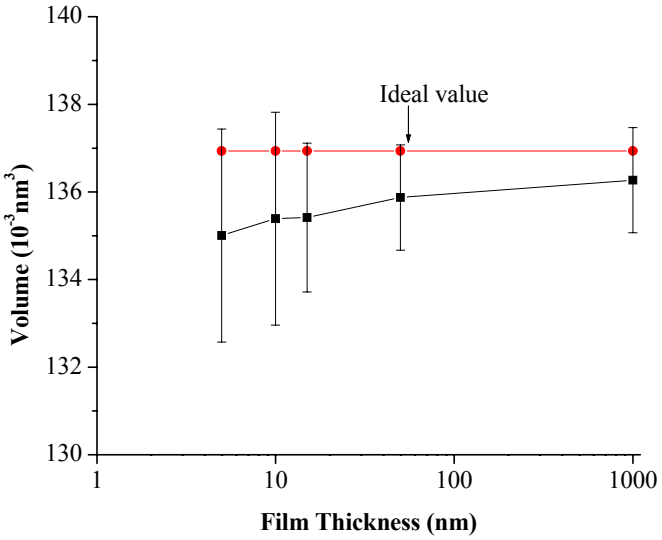

Figure 4.10. Volume of GaN crystal calculated from the lattice constants.

Kim et al. have reported the critical thickness of GaN on AlN/sapphire [1]. The lattice mismatch between GaN and AlN is about 2.43%, which is larger than the lattice mismatch between GaN and LGO. The critical thickness of GaN on AlN is ~30 Å, thinner than that of GaN on LGO, as would be expected.

The calculation of strain in GaN from measured lattice constants can be determined by

$$\varepsilon_{\text{a-axis}} = (v_{\text{-2, unstrained}} - v_{\text{-2}}) / v_{\text{-2, unstrained}} \quad (4.7)$$

$$\varepsilon_{\text{b-axis}} = (a_{\text{-2, unstrained}} - a_{\text{-2}}) / a_{\text{-2, unstrained}} \quad (4.8)$$

$$\varepsilon_{\text{c-axis}} = (c_{\text{unstrained}} - c) / c_{\text{unstrained}} \quad (4.9)$$

where $\varepsilon_{\text{a-axis}}$ and $\varepsilon_{\text{b-axis}}$ are the in-plane strain in GaN along the a-axis and b-axis of LGO, and $\varepsilon_{\text{c-axis}}$ is the strain in GaN along the c-axis of LGO. Figure 4.8 shows that the strain along the a-axis is compressive and is decreased with increasing film thickness. When film thickness is 1μm, the film is relaxed and the thermal strain dominates. Along the b-axis, the compressive strains increased with increasing film thickness. Along the c-axis, the strains are tensile, as is expected from a net biaxial compressive strain in plane.

Poisson's ratios were calculated using the relation of the strains along c- and a-axis [13]:

$$\varepsilon_{\text{c-axis}} / \varepsilon_{\text{a-axis}} = -2\upsilon/(1-\upsilon) \quad (4.10)$$

Along the a-axis, υ_a is in the range of 0.2-0.35. Along the b-axis, υ_b is in the range of 0.16-0.5. These calculated values of Poisson's ratio are comparable with values reported in other publications [14, 15].

Finally, a 1μm GaN film with a 16nm buffer layer was grown on LGO. The lattice constants were measured as $a_{\text{-2}}$ =3.1715Å, $a_{\text{-4}}$=3.1804Å, which is different and higher than those of the 1μm GaN grown without the buffer. This indicates that a buffer layer with thickness larger than critical thickness could relieve the strain.

4.3 The Dislocation Density Derived from X-ray Analysis

The mosaic structure of the epilayers is determined by the size and the angular distribution of the mosaic blocks. A set of four parameters would reflect the mosaic structure: lateral coherence length, vertical coherence length, twist, and tilt. The tilt and twist describe the angular distribution of the crystallographic orientation of the mosaic blocks perpendicular to and within the growth plane. The lateral and vertical coherence length determine the mosaic block size. The coherence lengths and the twist and tilt angle are correlated with different kinds of dislocations. For GaN grown on c-plane sapphire, two major kinds of threading dislocations are observed: screw dislocation with Burgers vector b_c=<0001>, and edge dislocation with Burgers vector b_a=1/3<11$\bar{2}$0> [16].

Using a triple-axis diffractometer for the measurements, the broadening of the rocking curve (angular scan or ω-scan) is influenced only by the tilt (out-of-plane misorientation) and the small correlation length parallel to the substrate surface in symmetric reflections 0002, 0004, and 0006 of GaN grown on c-plane sapphire. Wafer bendings or heterogeneous strains do not influence the peak broadening owing to the small acceptance angle of the detector. As the broadening in reciprocal space due to tilted crystallites is proportional to the scattering order and the broadening in reciprocal space due to a small correlation length is independent of the scattering vector, a graphical separation of these two effects is possible by recording higher order reflections. If a linear supposition of both effects is assumed, a separation analogous to the Williamson-Hall plot can be performed. When $\beta_\omega(\sin\theta)/\lambda$ is plotted against $(\sin\theta)/\lambda$ for each reflection and fitted by a straight line, β_Ω is the integral width of the measured profile, λ is the X-ray

wavelength, and 2θ is the scattering angle [17]. From the y-intersection y_0 of the fitted line the correlation length $L_{\parallel}$ can be estimated by

$$L_{\parallel} = \frac{0.9}{2y_0} \qquad (4.11)$$

The slope is a direct measure of the tilt angle α_ω.

If one assumes that both screw dislocations (b_c=[0001]) are related to an edge-type misfit dislocation in the interface with the same Burgers vector that leads to a corresponding tilt of single crystallites, the density of these screw dislocations $N_{[0001]}$ can be obtained using the following equation[18] as modified by Dunn and Koch [19]:

$$N_s = \frac{\alpha_\omega^2}{4.35 b_c^2} \qquad (4.12)$$

where b_c is the Burgers vector of the c-type threading dislocation ($|b_c|$=0.5185nm).

In the radial-scan direction (ω-2θ scan) of the symmetric reflections 0002, 0004, 0006, a small correlation length normal to the substrate surface and a heterogeneous strain along the c-axis causes a broadening of the Bragg reflections. Again these two effects can be separated owing to either their different dependency on the diffraction vector. In the Williamson-Hall plot, $\beta_\omega(\cos\theta)/b$ is plotted against $(\sin\theta)/\lambda$ for each reflection and fitted by a straight line. From the y-intersection y_0, the correlation length $L_\perp$ can be estimated by

$$L_\perp = \frac{0.9}{2y_0} \qquad (4.13)$$

The strain $\varepsilon_\perp$ is obtained directly from the slope of the line, which is $4\varepsilon_\perp$.

a-Type threading dislocations (b_a=1/3<11$\bar{2}$0>) mediate an azimuthal rotation of crystallites around the surface normal. This twist angle α_ϕ can be measured by performing ϕ-scans on asymmetric reflections (surface normal and diffraction vector are not parallel), where the sample is rotated with respect to the surface normal. When the broadening due to small correlation length $L_\parallel$ can be neglected, the measured broadening β_ϕ of the ϕ-scans is equal to α_ϕ. If dislocations are piled up in small angle grain boundaries, the following formula is used [18, 20]:

$$N_E = \frac{\alpha_\phi}{2.1\left|b_E L_\parallel\right|} \tag{4.14}$$

which describes the formation of subgrains with an average size $L_\parallel$, where b_E is the Burgers vector of the edge dislocations. (In our case $|b_E|=|b_a|$=0.3189nm).

We measured these two kinds of dislocations for the GaN grown on c-plane LGO. The ω-scan and ϕ-scan were performed on the samples grown on LGO, the screw and edge dislocation densities were calculated, and confirmed with the etch pit density measurement. It has been found that the error caused by the alignment of the machine, the scan method, and the estimation on the integral width can be very large, but if all of the materials are measured under the same conditions, the data is reasonable and comparable.

Shown in Figure 4.11 are the Williamson-Hall plots for the samples grown directly on LGO, with thicknesses of 5nm (N900), 10nm (N898), 15nm (N897), 50nm (N05), and 1μm (N901). From this plot, the tilts for these samples were estimated to be 409, 1416, 810, 474, and 160 arcsec, respectively. This translates to screw dislocation

densities of $3.38\times10^{8}/cm^{2}$, $1.65\times10^{10}/cm^{2}$, $4.03\times10^{9}/cm^{2}$, $1.30\times10^{9}/cm^{2}$, and $5.50\times10^{7}/cm^{2}$, respectively. The corresponding coherence lengths for these samples are estimated to be 2.432μm, 0.0715μm, 0.126μm, 0.215μm, 0.687μm. When the film thickness is 10nm, around the critical thickness, the dislocation density becomes larger than the 5-nm thick film, for the reason that the defects are introduced to release the strain. After that, the screw dislocation density decreased with increasing film thickness and the coherence length increased. These data are consistent with our assertation that the critical thickness for GaN grown on LGO is around 10nm. The dislocation density of the 1μm sample significantly decreased. One reason is that the film is relaxed; another reason is that this thick sample was grown under Ga-rich conditions with lower dislocation densities generated than the thin samples grown under N-rich condition.

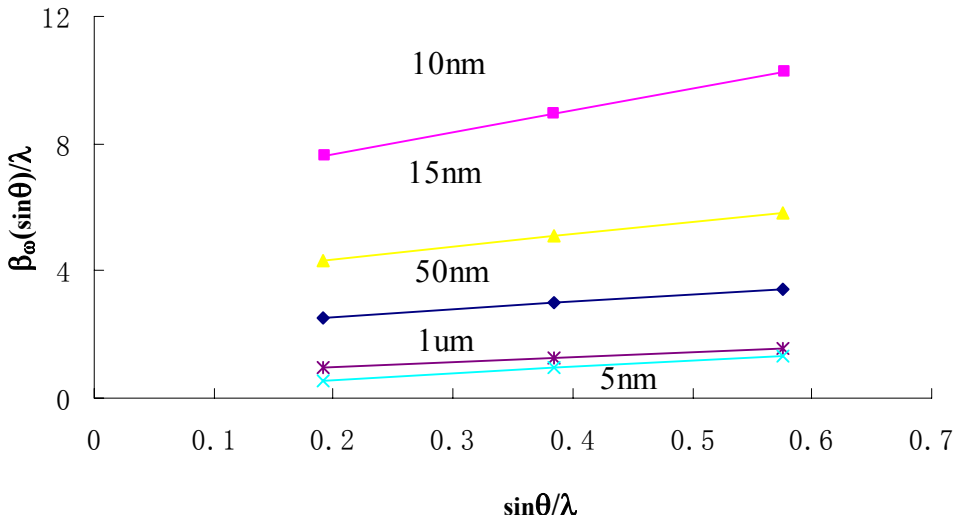

Figure 4.11 Williamson-Hall plots of the films grown directly on LGO with different thickness.

Figure 4.12 shows the Williamson-hall plot of the film with a thickness of 1 μm, grown without (N901) and with buffer (N999). Here, the buffer means an N-rich GaN layer of 16nm, inserted between the bulk and substrate. For N999, the tilt angle decreased to 30 arcsec, and the dislocation density is as low as $1.6\times10^{6}/cm^{2}$, and the coherence length increased to 3.393 μm. It clearly demonstrates that the GaN layer grown on LGO without the buffer has a high mosaicity. The buffer filters the threading dislocations and enhances the lateral coalescence, thereby enlarging the grain size. The data also proves that LGO is a suitable substrate for GaN because of the low dislocation density, which is two degrees lower than GaN grown on sapphire.

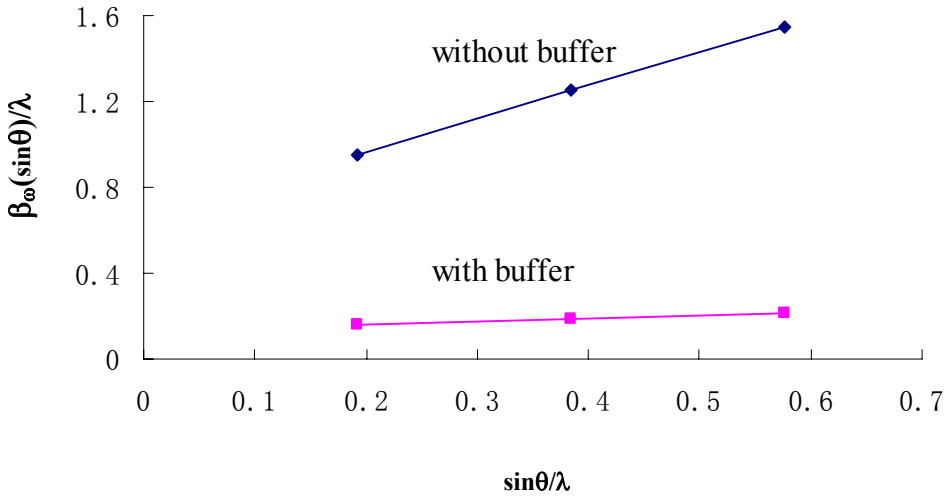

Figure 4.12. Williamson-Hall plots of the 1μm GaN films grown with and without buffer.

To estimate the twist angle and edge dislocation density, asymmetric $(10\bar{1}5)$ ϕ scans were preformed. The ϕ scan of 15 nm GaN is shown in Figure 4.13. It clearly shows six peaks in each ϕ scan, indicating the six directions of a GaN crystal structure.

The widths of the ϕ scans (α_ϕ) were used to calculated the edge dislocation density according to Eqn.4.14. The highest peak was used to measure the width, for the reason of machine alignment.

The twist angles from the ϕ scans for the films with the thickness from 5 nm, 10 nm, 15nm, 50nm, and 1μm were 6^0, 5.3^0, 3.2^0, 2.5^0, and 1.5^0, respectively. The edge dislocation densities were $6.43\times10^9/cm^2$, $1.88\times10^{11}/cm^2$, $6.63\times10^{10}/cm^2$, $3.03\times10^{10}/cm^2$, and $7.55\times10^9/cm^2$. The edge dislocation density was one or two orders higher than the screw dislocation density and possessed the same trend of the screw dislocation density with changing the film thickness. When the film thickness is below the critical thickness, the edge dislocation is relatively small. Beyond the critical thickness, the dislocation density decreased with film thickness increasing. For the film with buffer, the twist angle was 0.13^0, and the edge dislocation density was $9.68\times10^7/cm^2$. The dislocation density could be measured by etching. However, this method is not suitable to extra thin films, which can not stand the etching. The 1μm samples with and without buffer were then etched in phosphoric acid at 160 ^{0}C for 30 seconds, and characterized by AFM. The etched surface morphology of samples are shown in Figure 4.14. The etch pit density of the sample without buffer is approximately $4\times10^8/cm^2$, and the one of the sample with buffer is approximately $2.5\times10^7/cm^2$. The measured decrease in etch pit density after insertion of a buffer is in good agreement with that estimated from Williamson-Hall plots. The buffer was a good filter for dislocations. All the data are listed in Table 4.3.

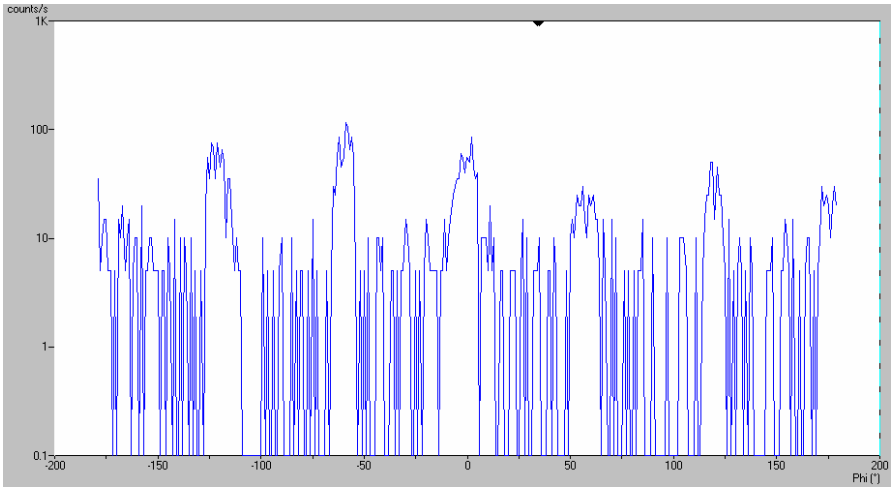

Figure 4.13. (10 $\bar{1}$ 5) ϕ scan of 15 nm GaN.

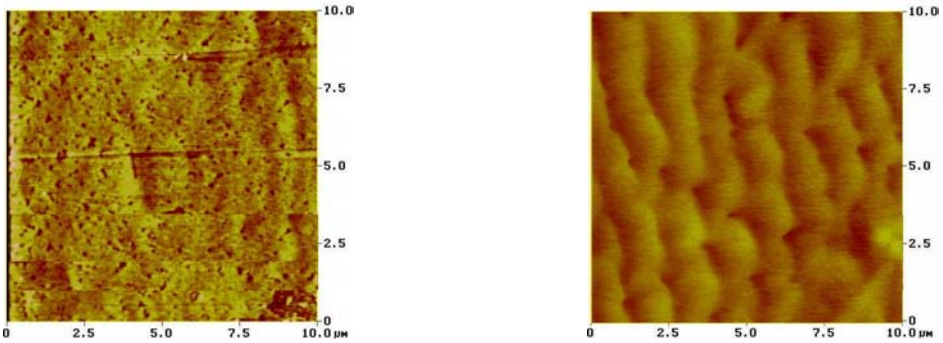

Figure 4.14 AFM images of etched surfaces (a) 1 µm sample grown without buffer, (b) 1 µm sample grown with buffer.

TABLE 4.3 Analysis summaries of XRD measurements for samples with different thickness.

Sample thickness	5nm	10nm	15nm	50nm	1um no buffer	1um w/ buffer
$L_{\parallel}$ (µm)	2.432	0.0715	0.126	0.215	0.687	3.393
Ns (cm^{-2})	3.38×10^{8}	1.65×10^{10}	4.03×10^{9}	1.30×10^{9}	5.50×10^{7}	1.80×10^{6}
NE (cm^{-2})	6.43×10^{9}	1.88×10^{11}	6.63×10^{10}	3.03×10^{10}	2.55×10^{9}	9.68×10^{7}
tilt angle (arcsecond)	409	1416	810	474	160	30
twist angle (degree)	6	5.2	3.2	2.5	1.5	0.13
etch pits (cm^{-2})	x	x	x	x	4×10^{8}	2.5×10^{7}

In summary, x-ray diffraction was used to measure the lattice constant of GaN grown on LGO by MBE. Because of the asymmetric structure of the substrate, the lattice constants of GaN are asymmetric. The growth kinetics of elastically strained GaN are found to be significantly different from that of plastically deformed GaN as determined by RHEED analysis. The critical thickness was measured to be ~93Å, which is close to the predicted critical thickness 102 Å. We also studied the dislocation density by XRD measurement. It was found that when the film thickness was below 10nm, the dislocation density was small, which increased two degree order higher when the film thickness was 10nm. The change in dislocation density supports our conclusion that the critical thickness is approximately 10 nm. When the film thickness was above 10nm, the dislocation densities decrease with increasing film thickness. We also found that GaN buffer provides a better template for lower dislocation density growth. Comparing to the other substrates, the smaller lattice mismatch of LGO relative to GaN resulting lower dislocation density demonstrates that LGO is an excellent substrate for GaN growth, and due to the comparatively large critical thickness, the use of lithium gallate substrates affords a unique tool for examining the growth kinetics of elastically strained GaN.

4.4 Appdendix

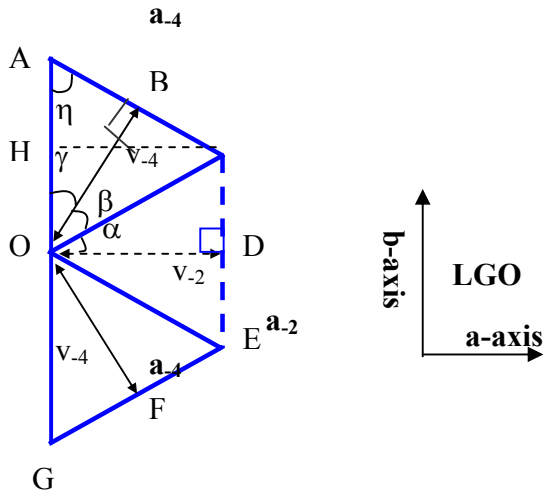

Figure 4a.1Half of the distored GaN crystal structure.

The crystal structure of asymmetric GaN is shown in Figure 2.2 To simplify the explaination of calculation, only half of the crystal structure is drawn in Figure 4a.1, in which AC and EG are the lattices a_{-4}, CE is the lattice a_{-2}, OB and OF are the vectors V_{-4}, and OD is the vector v_{-2}.

We assume all the vectors are perpendicular to the lattices, though the vectors are not exactly perpendicular. The difference from 90^0 is less than 1^0, thus the error is less than 0.15%. Since this is a half-symmetric structure, it is obvious that AG=2CE and AO=CE.

In the triangle of AOD : $\gamma=90^0-(\alpha+\beta)$.(4a.1)

In the triangle of AOB: $\eta=90^0-\gamma=\alpha+\beta$.(4a.2),

Thus , $2\tan^{-1}\eta=\tan(\alpha+\beta)$ (4a.3)

In the triangle of ACH, because CH is perpendicular to AO: $\sin\eta=v_{-2}/a_{-4}$, (4a.4)

Also $\cos\eta = 0.5a_{-2}/a_{-4}$, (4a.5)

In the triangle OCD, $\tan\alpha = a_{-2}/2v_2$ (4a.6)

From Equations (4a.4) and (4a.5): $\tan\eta = a_{-2}/2v_2$ (4a.7)

Combine Equation (4a.7) with (4a.6), $\tan\eta = \tan\alpha$ (4a.8)

combine Equation (4a.8) with (4a.3), $\tan(\alpha+\beta) = 2\tan^{-1}\alpha$ (4a.9)

Because the triangles OBC and ODC share the same side OC, $v_{-2}/\cos\alpha = v_{-4}/\cos\beta$, or $\cos\alpha/\cos\beta = v_{-2}/v_{-4}$ (4a.10)

From Equation.(4a.9) and (4a.10), the angle of α and β could be calculated.

Then from Equation. (4a.6): $a_{-2} = 2v_{-2}\tan\alpha$ (4a.11)

And in the triangle AOC, $a_{-4} = v_{-4}(\tan\beta+\tan\gamma)$ (4a.12)

Finally the values of lattice constants a_{-2} and a_{-4} can be calculated from the vectors that were directly measured from x-ray, and the angles that are calculated based on the above equations .

Drawing software was used to testify this mathematical model. By setting the values of the vectors that are obtained from the x-ray measurements, a distorted GaN crystal structure was drawn, and the length of each side could be obtained from this drawing software.

For example, from measurement of a 5 nm sample, the two vectors v_{-2}=0.26980nm, and v_{-4}=0.27446 nm. Using the above equations, the lattice constants are calculated as a_{-2}= 0.31876 nm, and a_{-4}=0. 31336 nm

The structure was drawn with the value of v_{-2} and v_{-4}, as shown in Figure 4a.2. The length of each side given by the software is in good agreement with our calculation. Our calculation is proved to be correct**.**

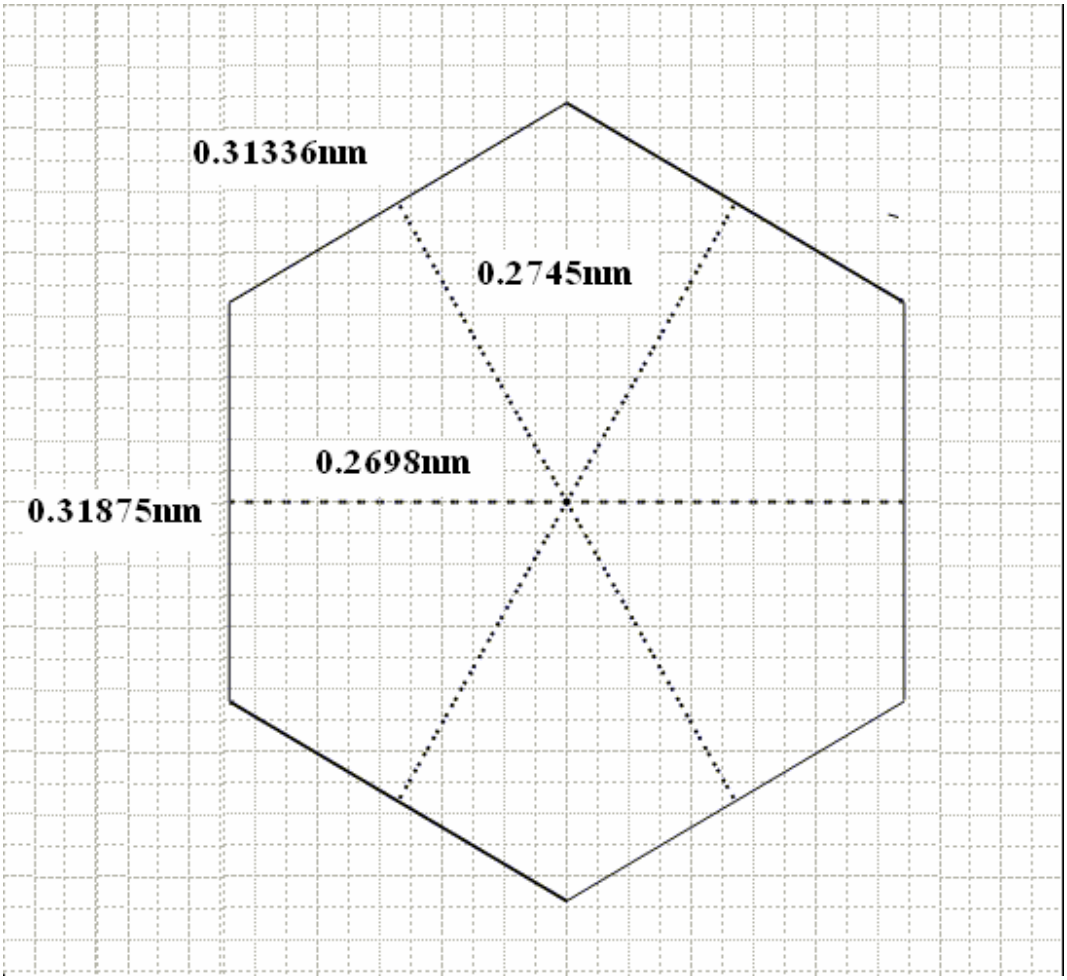

Figure 4a.2 A drawing of the GaN distorted crystal structure from software.

4.5 References:

[1] Personal communication with Prof. Tom Kuech.

[2] C. Kim, I. K. Robinson, J. Myoung, K. Shim, M.Yoo, and K. Kim, Appl. Phys. Lett., Vol. **69**, 2360, (1996*)*.

[3] P.F. Fewster, X-Ray Scattering from Semiconductors, Oxford; Inst. Phys. Conf. Ser. No **164,** 197 (1999).

[4] S. W. Seo, K. K. Lee, Sangbeom Kang, S. Huang, William A. Doolittle, N. M. Jokerst, and A. S. Brown, Appl. Phys. Lett. **79**, 1372-1374 (2001).

[5] J. Perry. Thin solid films, **324**, 107-114.

[6] K. Wang, R.R. Reeber, Mat. Res. Soc. Symp. Proc., **482**, 863, (1998).

[7]. H. Neumann, E. Pirl, G. Kühn, J. Mat. Sci.,Lett., **6**, 495, (1987).

[8] S. Perkowitz, Optical Characterization of Semiconductor: Infrared, Rama, and Photoluminescence Spectra, Academic, London, P 325, (1990).

[9] D.M. Hansen, P.D. Moran, K.A. Dunn, S.E. Babcock, R.J. Matyi, and T.F. Kuech, J. of Crys. Growth, **195**, 44, (1998).

[10] J. W. Matthews and A. E. Blakeslee, J. Cryst. Growth **32**, 265, (1974).

[11] B. W. Dodson and J. Y. Tsao, Appl. Phys. Lett.**52**, 52 (1988).

[12] A. Fischer, H. Kuhne, and H. Richter, Phys. Rev. Lett. **73**, 2712, (1994).

[13] A. Kelly and G. W. Groves, *Crystallography and Crystal Defects (*Addison-Wesley), Reading, MA, (1970).

[14] L. T. Romano, B. S. Krusor, M. D. McCluskey, D. P. Bour, K. Nauka, Appl. Physics Letters, **73**, 1757, (1998).

[15] W. G. Perry, T. Zheleva, M. D. Bremser, R. F. Davis, W. Shan, and J.J. Song, *J. of Electronic Materials,* **26**, 224, (1997).

[16] T. Metzger, R. Hoppler, E. Bom, O. Ambacher, and M Stutzmann et al. Phys. Status Solidi A **77**, 1013 (1998).

[17] G.K. Williamson, and W.H. Hall, Acta. Metall. **1**, 22, (1953).

[18] P. Gay, P.B. Hirsch and A. Kelly, Acta Metall. **1**, 315 (1953)

[19] C. Dunn and T. Koch, E.F. Acta Metall., **5**, 548 (1957).

[20] P.F. Fewster J. Appl. Crystallogr., **22**, 64, (1989).

C H A P T E R 5

THE MICROSTRUCTURE AND DISLOCATION DENSITIES OF GAN GROWN WITH SUPERLATTICE BUFFERS

As discussed in Chapter 3, it has been found that AlGaN/GaN superlattices (SL) can filter impurity diffusion from the LGO substrate. An outstanding research question is what Al composition in SL would mostly relieve the strain and decelerate the dislocation density in the resultant GaN films.

5.1 Strain Simulation

The lattice constants of GaN and LGO at room temperature and growth temperature are shown in Table 4.2. The in-plane lattice constant of AlN is 3.112nm [1]. The lattice constants of $Al_xGa_{1-x}N$ were calculated on the basis of the lattice constants of GaN and AlN and their composition. It has found that at room temperature the average strains of $Al_{0.44}Ga_{0.56}N$ to LGO are almost the same as the negative of the strains of GaN to LGO. The total strains are therefore balanced, and the "frozen-in" defects caused by thermal expansion differences are minimized. At growth temperature, $Al_{0.12}Ga_{0.88}N$ is strain balanced with GaN grown on LGO, and the defects formed during growth are minimized. The lattice constants of $Al_{0.12}Ga_{0.88}N$, $Al_{0.44}Ga_{0.56}N$, GaN and LGO listed in Table 5.1 are converted to a_{LGO} and b_{LGO} directions for comparison.

TABLE 5.1 Lattice constants of $Al_xGa_{1-x}N$ at room and growth temperature [1-3].

	$Al_{0.12}Ga_{0.88}N$		$Al_{0.44}Ga_{0.56}N$		LGO		GaN	
	a (Å)	b (Å)	a (Å)	b (Å)	a (Å)	b (Å)	a (Å)	
RT (298K)	5.494	6.299	5.5445	6.291	5.407	6.379	5.521	6.376
GT (900K)	5.522	6.356	5.470	6.317	5.451	6.455	5.538	6.395

To find out the effect of Al composition in the superlattices, three groups of samples were grown with different superlattices. Usually, a buffer layer was first grown. The thickness of the buffer was 16 nm, larger than the critical thickness of GaN, as calculated in Chapter 4. A 5-period GaN/AlGaN SL follows. The total thickness of SL was approximately 16nm. The first group has $Al_{0.12}Ga_{0.88}N$ in SL, the second group has $Al_{0.28}Ga_{0.72}N$, and the third group has $Al_{0.44}Ga_{0.56}N$. Finally a bulk GaN film was grown on the top, with thicknesses from 5 nm, 10 nm, 15 nm, 50 nm, to 1 μm. The material structure is shown in Figure 5.1.

In the last section, the strains and lattice constants were calculated from the x-ray symmetric and asymmetric scan by determining the GaN peak's position. However, the strains are complicated with SL grown, as shown in Figure 5.1. The total strains include the strains between the buffer and substrate, between SL and the buffer, and between bulk GaN and SL. The rocking curves of the films with 10nm GaN grown on SL are shown in Figure 5.2. With different Al composition in SL, the GaN peak positions are different. But since the GaN peak position reflects both the total strain and the change in Al composition, the strain change inside bulk could not be read from x-ray scan directly.

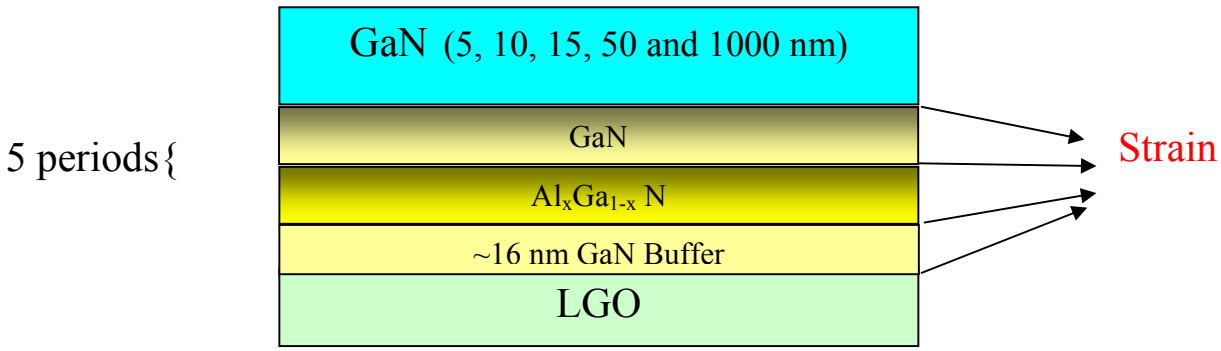

Figure 5.1 The material structure and the strain distribution.

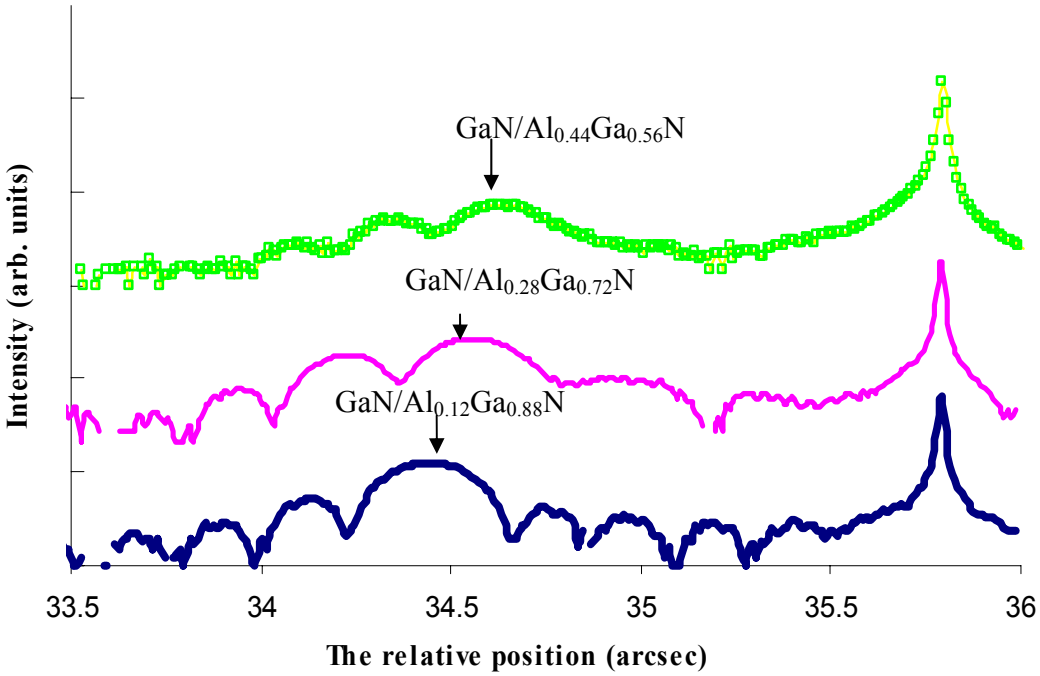

Figure 5.2 The 2θ-ω scan of 10nm GaN grown with superlattices.

To find out the individual strains, simulations on the rocking curves were performed. During simulations, the lattice constants listed in Table 5.1 were used in the substrate and layer's model. Since the symmetric (002) scan is only related with the perpendicular lattice constant, the in-plane directions of the crystal were not considered in the simulation. The strain was calculated as

$$\varepsilon=(a^{*}-a_s)/a_s \tag{5.1}$$

where a^{*} is the distorted lattice constants of the layer, and a_s is the unstrained lattice constant of the layer beneath.

The samples discussed in the last chapter were first simulated to test the reliability of the software. The error of the strains was ~2%, caused by both the calculation method of the software and the fitting method of the user. Though the values are not accurate, the trend of the strain's change was correct. Thus, the simulation could help us to obtain the information of how the strains changed when SL was inserted between the bulk film and substrate.

The simulation for the 10nm GaN on $Al_{0.12}Ga_{0.88}N$ is shown in Figure 5.3 (a). The simulated curve is below the original rocking curve. From simulation, the strain of the buffer was determined to be -1.03%, the strain of AlGaN in SL was -0.77%, the strain of GaN in SL was -1.10%, and the stain of the bulk GaN layer was -0.45%. It has been found that the strain of the buffer affected the GaN peak position of the rocking curve the most, while the strain of the top GaN layer affects it less. As shown in Figure. 5.3 (b), when the buffer strain changes 50% relative to the one in (a), the simulated GaN peak

shifted, compared to the simulation in (a). In Figure 5.3(c), the stain of the top layer changes 50% relative to the one in (a), the shift of simulated GaN peak is not significant, but the shape of the fringes changed. The change in simulated GaN peak position proved that the GaN peak in the original rocking curve represents the strains of the buffer layer rather than the strains of the bulk layer, because the thickness of the buffer is larger than the bulk layer. Therefore, the conventional way to analyze strains is not suitable in this chapter. The strain analysis must depend on the simulation.

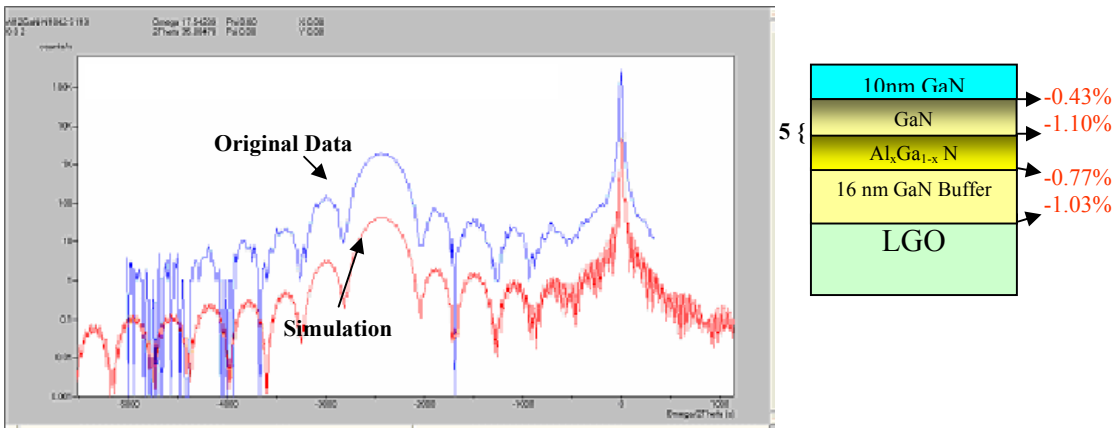

(a)

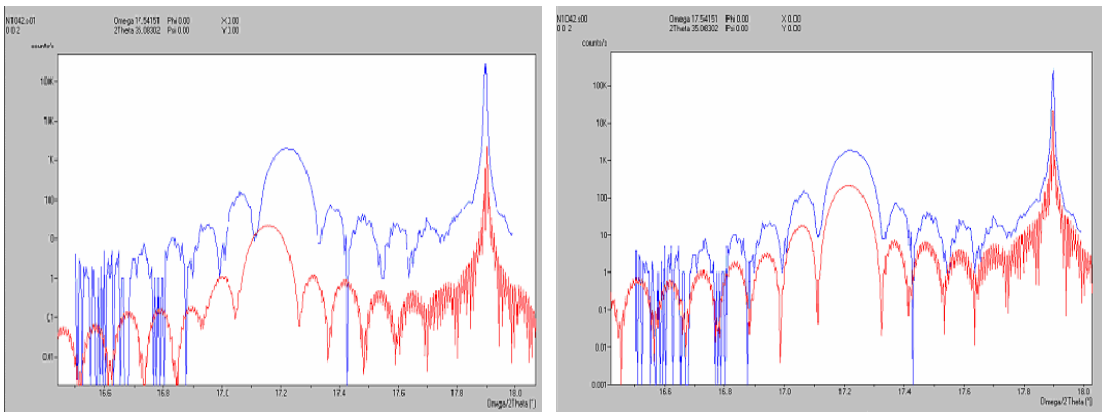

(b) (c)

Figure 5.3 (a) The simulated and original curve of 10nmGaN with $Al_{0.12}Ga_{0.88}N$ SL, and the strained obtained from simulation; (b) the simulation when the strains in the buffer changed 50%; (c) simulation when the strain in the bulk changed 50%.

The simulations of 10 nm GaN grown with the other two SL are shown in Figure 5.4. When the epitaxy film thickness was thicker than the buffer, the GaN peak position was affected by the strains of the bulk layer more than by the strain within buffer layer. The simulation of the 1 μm films are shown in Figure 5.5. The strains of all the films are listed in Table 5.2.

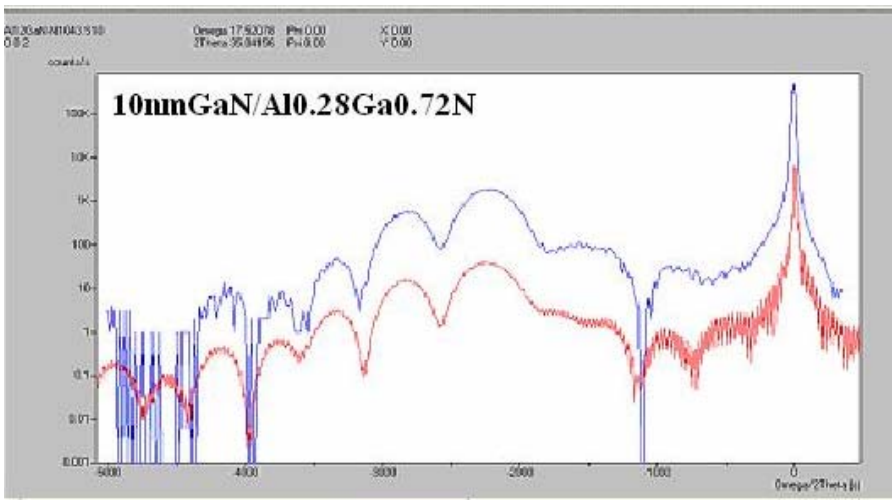

(a)

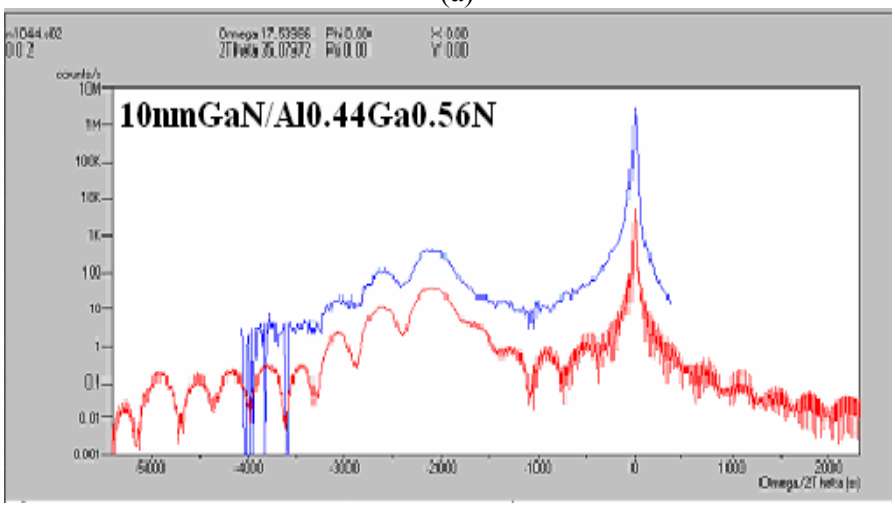

(b)

Figure 5.4 Original curves (upper one) and simulation of 10nm GaN grown with (a) $Al_{0.28}Ga_{0.72}N$ superlattices; (b) $Al_{0.44}Ga_{0.56}N$.

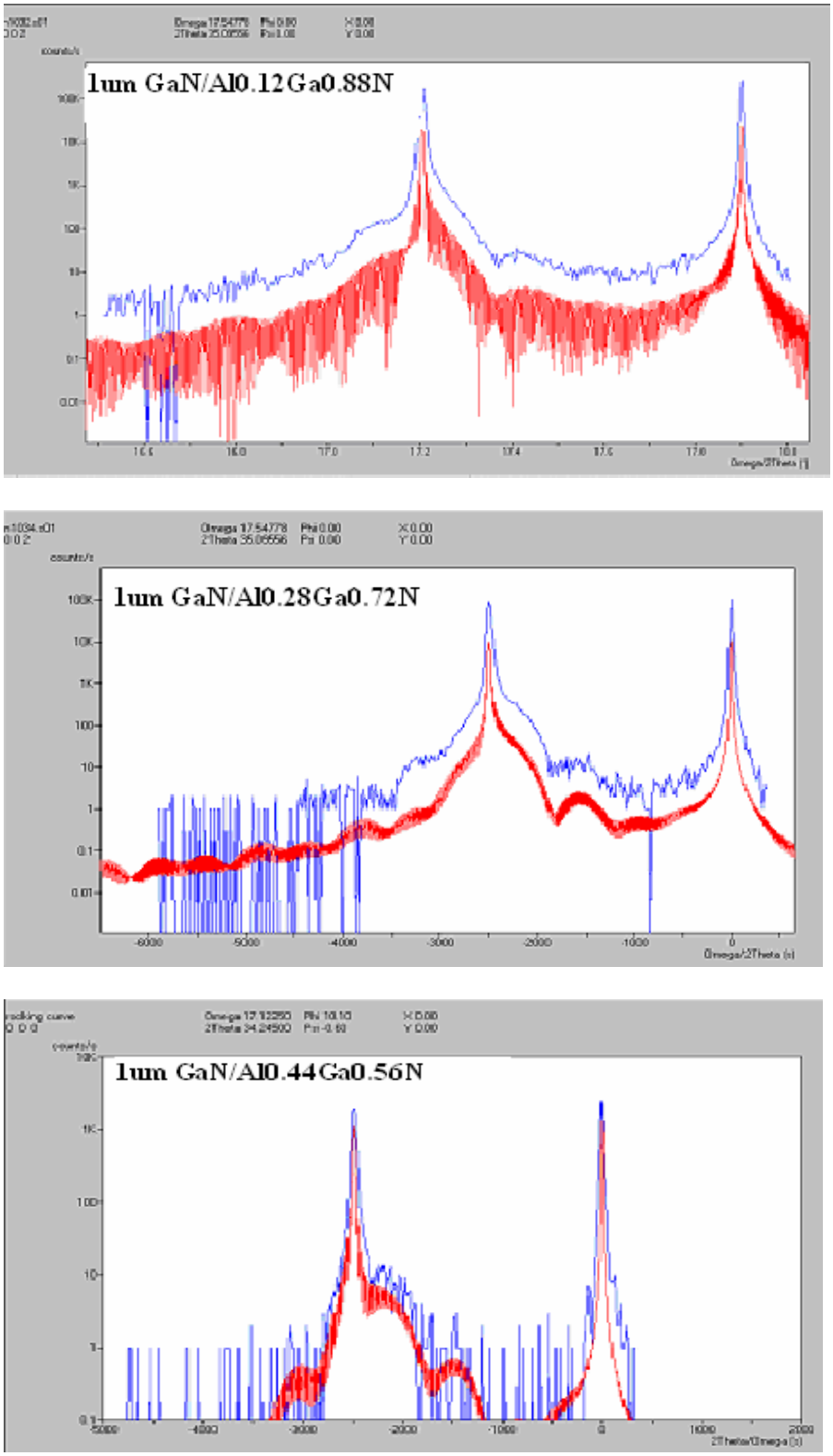

Figure 5.5 Original curve (upper) and simulation of the 1μm GaN grown with SL.

TABLE 5.2 Summary of the strains obtained from simulation.

Thickness (nm)	Al compo.	Buffer strain (%)	AlGaN SL strain (%)	GaN SL strain (%)	Bulk strain (%)
1000	0.12	0.4807	-0.2907	0.4807	0.52
1000	0.28	0.4210	0.2672	0.4339	0.50
1000	0.44	0.4791	0.6234	0.4632	0.40
50	0.12	0.5807	-0.2616	0.6069	0.57
50	0.28	0.6523	0.3000	0.7077	0.62
50	0.44	0.7694	0.3122	0.7878	0.70
15	0.12	0.6533	-0.3780	0.6945	0.36
15	0.28	0.6645	-0.2156	0.7460	0.19
15	0.44	0.6823	0.4038	0.6936	0. 60
10	0.12	0.6242	-0.3471	0.6611	0. 25
10	0.28	0.6097	-0.1624	0.6166	0. 26
10	0.44	0.7839	0.2970	0.8035	0.18
5	0.12	0.5516	-0.2485	0.5117	0. 08
5	0.28	0.6533	0.0230	0.7083	0. 46
5	0.44	0.8420	0.2314	0.8794	0. 21

5.2 Strain Analysis

It was noted in 1995 by Huang, FY and Wang, KL that the strain can be transferred between two epitaxial thin films with different lattice constants [4]. It was demonstrated that a bulk film grown on top of a thin buffer layer may release the strain to the buffer layer, leaving the bulk film dislocation free. A strain transfer model set up by them could explain the strains' change in our samples grown with SL.

When one of the thin films (with a stress-free lattice constant of a_2 and a film thickness of h_2) is grown on top of the other (with a relaxed lattice constant of a_1 and a film thickness of h_1), the two films will reach a common lattice constant a_0 given by

$$a_0 = \frac{b_1 h_1 / a_1 + b_2 h_2 / a_2}{b_1 h_1 / a_1^{\,2} + b_2 h_2 / a_2^{\,2}} \tag{5.2}$$

where b is the magnitude of Burgers vector. Thus, elastic strains ε_1 and ε_2 for the thin films are given by [5]

$$\begin{aligned} \varepsilon_1 &= \frac{b_2 h_2 (1/a_1 - 1/a_2)}{a_2 (b_1 h_1 / a_1^{\,2} + b_2 h_2 / a_2^2)} \\ \varepsilon_2 &= \frac{b_1 h_1 (1/a_2 - 1/a_1)}{a_1 (b_1 h_1 / a_1^{\,2} + b_2 h_2 / a_2^2)} \end{aligned} \tag{5.3}$$

It can be seen that the elastic strains are related with both the film thickness and lattice constants. A decrease in h_1 will lead to an increase of strain in the first film and a decrease in the second. With a small thickness of the first film, the strain may be transfered from the second grown film to the first film as the epitaxial growth proceeds, leaving the second film dislocation free. To enable the strain transfer, the thickness of the second film has to be kept below the critical thickness. An increase in h_2 will result in an increase of strain in the first film and decrease of strain in the second film.

Once the bulk film exceeds the critical thickness h_{c2}, dislocations may be generated. However, this critical thickness is different from the conventional critical thickness as determined by the lattice mismatch between the film and the substrate. When the critical thickness of the epitaxy film and buffer layer are larger than the corresponding film thickness, both films are both strained without dislocation,. Then besides the lattice constants, h_{c2} is also dependent on the thickness of the film:

$$h_{c2} = \frac{b_2}{2\pi}\left(k_{12}\frac{h_2}{h_1} + \frac{a_2}{a_1 - a_2}\right)\left(\frac{1 - \nu_2 \cos^2\alpha}{(1+\nu_2)\cos\gamma}\right)\left[\ln\left(\frac{h_{c2}}{b_2}\right) + 1\right] \tag{5.4}$$

where α is the angle between the dislocation line and the Burgers vector, γ is the angle between the Burgers vector and the direction normal to the surface, ν is the Poisson's ratio, and k_{12} is a constant related to burger's vector and lattice constants of the two films, $K_{12} = \frac{a_1^2 b_2}{a_2(a_1 - a_2)b_1}$. If the first film is a semi-infinite substrate and h_1 is infinite, this equation is as the same as Equation. 4.6. According to this equation, h_{c2} increase as h_1 decreases and h_2 increases. For a sufficiently small h_1, h_{c2} may become large enough that h_{c2} can be kept larger than h_{c2} for possible strain transfer.

Huang and Wang did not give out how the critical thickness of buffer changes with the bulk film thickness. But from the above equations, an expression similar to Eqn (5.4) can be driven out

$$h_{c1} = \frac{b_1}{2\pi}(k_{21}\frac{h_1}{h_2} + \frac{a_1}{a_1 - a_2})(\frac{1 - \nu_1 \cos^2 \alpha_1}{(1+\nu_1)\cos\gamma_1})[\ln(\frac{h_{c1}}{b_1}) + 1] \qquad (5.5)$$

The critical thickness of the buffer layer decreases as the bulk layer thickness increases.

The diagram of the critical thickness for the bulk film versus its film thickness in a $Si_{0.9}Ge_{0.1}$ alloy is shown in Figure 5.6 [4].

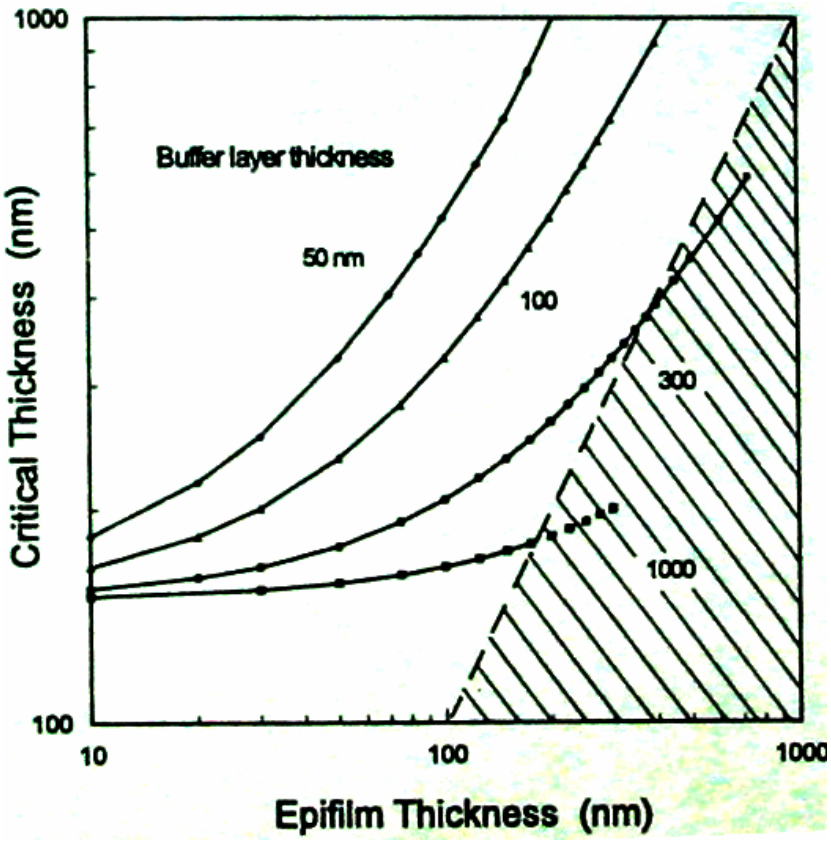

Figure 5.6. Diagram of the critical thickness h_{c2} of the bulk film versus the bulk film thickness h_2 for $Si_{0.9}Ge_{0.1}$ with different Si buffer thicknesses [4].

It can be seen that the critical thickness of the bulk film (indicated as epifilm in Figure 5.6) increases as the buffer layer thickness decreases and the bulk layer thickness increases, and Equations 5.3 and 5.4 are valid. The conventional critical thickness with a semi-infinite substrate is given by the condition that the bulk film has a small layer thickness and the buffer layer has a large thickness. In the diagram, the area defined by h_{c2} larger than $h_{2,}$ indicates the bulk film is dislocation free and strained whether the buffer is strained or relaxed. The area defined by h_{c2} less than h_2 indicates that the bulk film has a larger thickness than the critical thickness; however, whether it is strained or relaxed will be determined by the thickness of the buffer layer compared with its own

critical thickness h_{c1}. For a buffer layer whose thickness is less than h_{c1}, the bulk film reaches its critical thickness while the buffer layer is still strained; therefore, the bulk film will generate misfit dislocations and relax. It is then possible to grow thick and relaxed bulk film on top of a buffer layer whose thickness is less than $h_{c1.}$ On the other hand, for a buffer whose thickness is larger than h_{c1}, the buffer will first reach its critical thickness and starts to relax. As a result, the buffer layer will generate misfit dislocations, leaving the bulk film dislocation free and strained.

From the above description, the bulk's strain is not only related with its thickness and critical thickness, but also with the critical thickness of the buffer. If the thicknesses of the buffer (h_1) and bulk (h_2) are less than their critical thickness ($h_{c1,}$ h_{c2}), both films are strained and have the same lattice constants. Therefore, their strains' changes are the same. If h_1 is larger than h_{c1}, the buffer is relaxed and generated dislocations and the bulk will have fewer dislocations. The strains are also dependent on the film thicknesses, the thicker one usually determines the strain change of the thinner one.

The strain of multiple-layer structures would be more complicated than that of two-layer model. If we take the buffer and superlattice layer as film 1, and the bulk GaN film as film 2, the two-layer model can be used to analyze our data. The shortcoming of Huang's discussion is that he did not consider the effect of the substrate when both buffer and bulk are grown. He simply assumed that the substrate can be looked as a buffer with infinite large thickness. Knowing the truth of buffer's effects, we can try to explain our data.

Since the strains of the bulk and buffer are related with each other, they are drawn in the same diagram, as shown in Figure 5.7-5.9. The strain of the buffer was actually the

sum of the strains of buffer and all SL layers. Each group of samples will be explained individually.

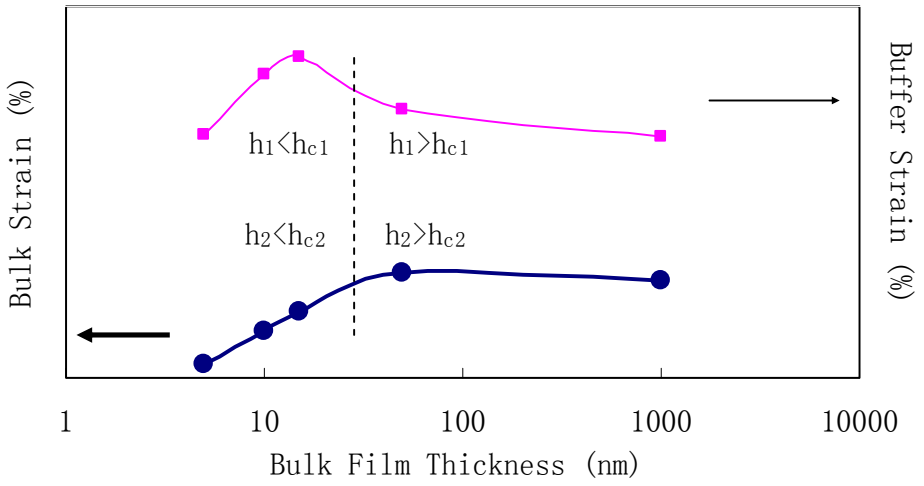

Figure 5.7 For GaN with $Al_{0.12}GaN$ SL, the absolute value of the strains of the bulk (bottom) and the strain of the buffer versus the bulk GaN thickness.

For the group with $Al_{0.12}GaN$ SL, the stains' change of the buffer and bulk against the thickness of the bulk layer are shown in Figure 5.7. GaN bulk film was more relaxed with smaller thickness. It is different from the strains of GaN grown directly on LGO in the previous chapter, which relaxed with increasing film thickness. Based on the previous discussion, when h_2 in the range of 5nm to 15nm, the buffer's strains increased with increasing film thickness; h_1 must be less than h_{c1}. If h_2 is less than h_{c2}, the bulk is also strained. Because h_2 is less than h_1, the bulk is as strained as the buffer, and its strain change is as the same as the buffer's. When h_2 is larger than 15nm, the strain of the buffer sharply decreased, indicating that it has reached h_{c1} and generated dislocations. Around this point, if h_2 is larger than h_{c2}, the bulk GaN is relaxed. But because of the strain transfer and more dislocations generated inside buffer, fewer dislocations are generated in

the bulk, then the strains of the bulk increased. With increasing h_2, finally, h_2 is larger than h_1, the bulk's strain change affect the buffer's instead of being affected. Thus, the bulk relaxed with increasing thickness, and the buffer followed bulk's change in the strains.

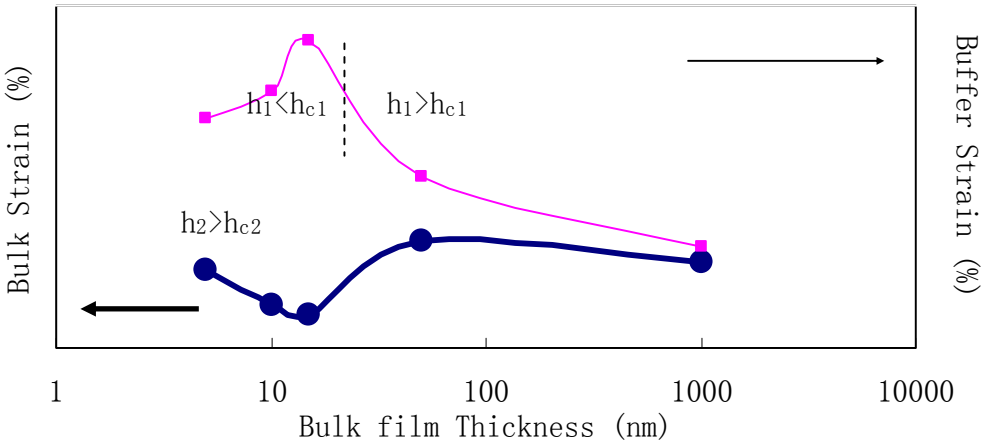

Figure 5.8 For GaN with $Al_{0.28}GaN$ SL, the absolute value of the strains of the bulk (bottom) and the strain of the buffer versus the bulk GaN thickness.

For the group with $Al_{0.28}GaN$, the strains' changes are shown in Figure 5.8. The buffer strain's change is similar to the previous one: when h_2 is less than 15nm, h_1 is less than h_{c1}; when h_2 is larger than 15nm, h_1 beyond h_{c1}. But the bulk's strain change is different from the previous one.

Because the lattice constants in the buffer changed with different Al composition, h_{c2} is also changed. For $Al_xGa_{1-x}N$ SL, when x is small, the lattice constant of $Al_xGa_{1-x}N$ is closed to GaN, h_{c2} is large. When x is equal to zero, h_c is infinite. On the other hand, with larger x, h_{c2} is smaller. Therefore, h_{c2} of the samples with $Al_{0.28}GaN$ must be smaller than the samples with $Al_{0.12}GaN$. It is reasonable that h_2 is always larger than h_{c2} in GaN bulk film with $Al_{0.28}GaN$ SL. It can also be concluded from Figure 5.8, from the strain

transfer between the buffer and bulk. When h_{c2} is less than 50nm, the bulk reached h_{c2}, strain transfer happens. It changed in the opposite way of the buffer's change. Finally, when h_2 is larger than h_1, the bulk is relaxed with large thickness, and the buffer followed the bulk's change.

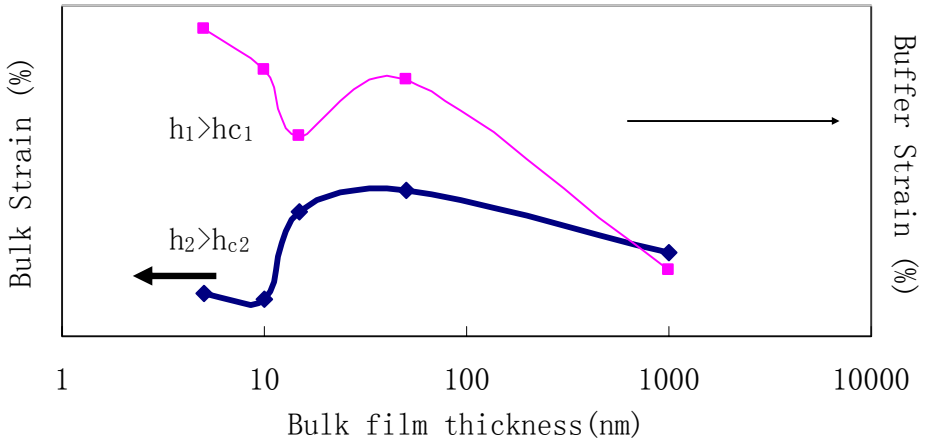

Figure 5.9 For GaN with $Al_{0.44}GaN$ SL, the absolute value of the strains of the bulk (bottom) and the strain of the buffer versus the bulk GaN thickness.

The strains of the samples with $Al_{0.44}GaN$ SL are shown in Figure 5.9. The buffer's change is different from the others. Initially its strain decreased with increasing film thickness; h_1 must be larger than h_{c1}. Only when h_2 is larger than h_{c2}, strain transfer happens and the bulk strains' change is in the opposite direction of the buffer. But between 15 nm and 50 nm, the buffer's strain increased and fell down again. This bump probably is caused by the bulk's change. At that point, h_2 is already larger than h_1 and determines the buffer's change. If one more sample is grown with the thickness between 15nm and 50 nm, the strain's change maybe clearer. After that, the bulk relaxed with increasing thickness.

If the strains of the three groups' are all shown in one graph (Figure 5.10), there is not big differences among the groups. Thus, it is hard to tell which Al composition is the best to relieve the strain. Probably with the extreme thin bulk, the one with $Al_{0.12}GaN$ SL would relieve the strain most, and with the thick bulk, the one with $Al_{0.44}GaN$ SL would relieve the strain most. It is interesting to find out how the buffer affects the bulk. If the research on a simple structure, for example, the GaN film grown on $LiGaO_2$ with only one layer of buffer (which has different lattice constants with GaN), could be processed in the future, there would be more interesting results on this topic.

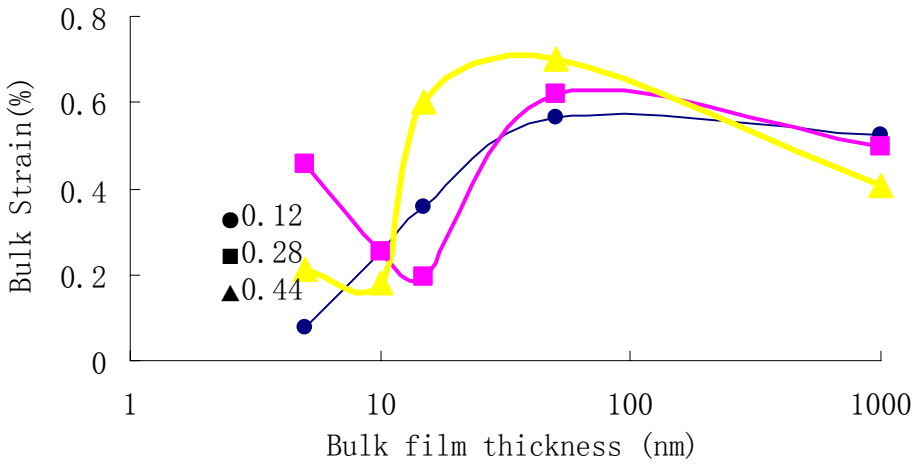

Figure 5.10 Bulk strain of all the films with different SL.

5.3 Dislocation Density

The dislocations inside the thin bulk films can't be calculated with the method as the same as discussed in Chapter 4, because the information obtained from x-ray represents the buffer when the buffer thickness is larger than the bulk. Only the 1 μm

samples were measured and calculated. The results are listed in Table 5.3. Comparing the films grown with different Al composition in the superlattice, it was found that the film grown with the $Al_{0.12}Ga_{0.88}N$/GaN SL have the least dislocation densities (both screw and edge) and longest coherence length. The dislocation of the film with $Al_{0.44}Ga_{0.56}N$/GaN SL is slightly fewer than the one with $Al_{0.12}Ga_{0.88}N$/GaN SL. The film grown with $Al_{0.28}Ga_{0.72}N$/GaN SL has the dislocation densities as high as twice of the other two samples. This proved our assumption at the beginning, because $Al_{0.12}Ga_{0.88}N$ and $Al_{0.44}Ga_{0.56}N$ reached the strain balance with GaN at growth temperature and room temperature, respectively, the formation of defects are minimized.

TABLE 5.3 Dislocation density of the 1 μm samples, with different buffer and SL condition.

Samples	N1032	N1034	N1035	N999	N901
buffer condition	12% Al	28% Al	44% Al	buffer only	no buffer/SL
$L_{\parallel}$ (μm)	3.486	2.069	3.352	3.393	0.687
Ns (cm^{-2})	1.72×10^{6}	4.80×10^{6}	1.85×10^{6}	1.80×10^{6}	5.50×10^{7}
NE (cm^{-2})	8.97×10^{7}	3.16×10^{8}	1.01×10^{8}	9.60×10^{7}	2.55×10^{9}
tilt angle (arcsecond)	29.2	49	30.3	30	160
twist angle (degree)	0.12	0.251	0.13	0.125	1.5
etch pits (cm^{-2})	2.2×10^{7}	9.5×10^{7}	2.3×10^{7}	2.8×10^{7}	4×10^{8}

The samples were also etched in phosphorous acid, the AFM images of etched surfaces are shown in Figure 5.11. Figure 5.11(a) is the AFM image of the sample with $Al_{0.12}Ga_{0.88}N$ SL, the etch pits density is approximately 2.2×10^{7}/ cm^{2}. Figure 5.11(b) is

the one with $Al_{0.28}Ga_{0.72}N$ SL, its the pit density is approximately 9.5×10^7/ cm^2. The difference in pits density is in good agreement with our calculation.

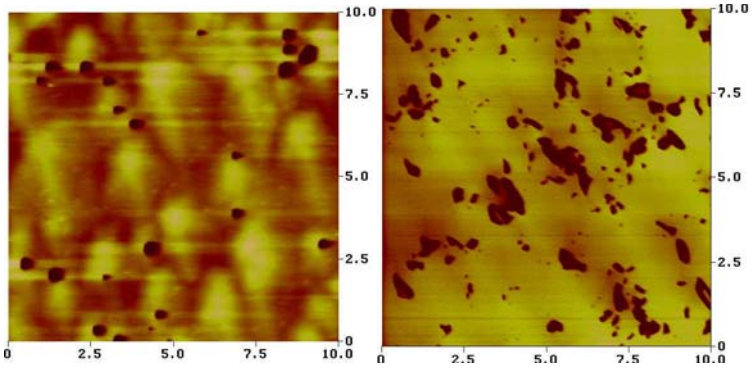

Figure 5.11. AFM images of 1-μm sample etched in phosphorus acid, (a) with $Al_{0.12}Ga_{0.88}$NSL, (b) with $Al_{0.28}Ga_{0.72}N$ SL.

These three samples are also compared with the samples mentioned in Chapter 4, the 1μm samples with buffer only and without buffer/SL. The dislocation density of the one grown with SL is one degree lower than the one grown directly on LGO. But the dislocation density of the film grown with the buffer is in the same range as the ones with $Al_{0.12}Ga_{0.88}N$/GaN SL and $Al_{0.44}Ga_{0.56}N$/GaN SL. Thus, obviously, an insertion of buffer decreases dislocations significantly. Insertion of superlattice buffers do not decrease dislocation density further. If the Al composition in the superlattices is other than 0.12 or 0.44, more defects are even introduced into the epitaxy film.

In summary, an insertion of AlGaN/GaN buffer complicates the strain analysis. The simulation of x-ray measurement helps to obtain the strain of each layer. It was found that the strains within GaN bulk film is related with the thicknesses and critical thicknesses of both bulk and buffer layers. The Al composition does not significantly affect the strains, but it is better to be 0.12 and 0.44 than 0.28 for less dislocation density.

5.4 References:

[1] S. Shur Michael, and M. Asif Khan, Mat. Res. Bull. **22 (2)**, 44, (1997).

[2] K. Wang, R.R. Reeber, Mat. Res. Soc. Symp. Proc., **482**, 863, (1998).

[3]. H. Neumann, E. Pirl, G. Kühn, J. Mat. Sci.,Lett., **6**, 495, (1987).

[4] F.Y. Huang, and K.L. Wang, Philo. Maga.Lett. **72**, 231, (1995).

[5] J. W. Matthews, *Epitaxial Growth,* Part A and Part B (New York: Academic Press), (1975).

C H A P T E R 6

THE GROWTH AND DEVICE INTEGRATION OF HIGH-SPEED InGaAs MSM

High-speed MSM devices were studied in the wavelength of 1.3-1.5 μm for the applications different from the UV photodetectors. $In_{0.53}Ga_{0.47}As$ was used as the active material, which was grown lattice matched to InP, using solid phosphorus MBE. The fabrication and integration process was similar to the GaN MSM with high speed as the target.

.

6.1 InGaAs High Speed MSM Devices

High-performance GaAs MSMs have been thoroughly investigated and found to have excellent performance in the 0.8-μm wavelength region [1,2]. InGaAs has been under intensive examination for wavelengths in the low-loss window of silica fiber-optic communication lines (1.3-1.5 μm), because of its advantage of lower band gap and lattice matched to InP [3]. However, the low barrier height on undoped InGaAs (0.2 V) yields unacceptably large dark currents in photodetectors, leading to poor device performance.

Research activities in GaAs MSM photodetectors have, so far, been mainly stimulated by high-speed potential of these devices. For transit-time-limited detectors, the

intrinsic speed response depends strongly on the finger spacing and applied bias. A simple scaling rule to design high-speed MSMs is to reduce the finger spacing to decrease the intrinsic response time, thereby increasing speed and achieving a very high electric field between the fingers with a low bias [4].

Finger spacing has been decreased to the submicrometer and even the nanometer scale. A device with a 25-nm finger width and spacing was fabricated using electron beam lithography [5], which represents the smallest interdigited MSM devices fabricated to date. However, for a given external bias, the electric field in the active region of the diode structure strongly increases as the finger spacing is decreased. The strong redistribution of the internal electric field in the MSM-PD with small separation between the fingers gives rise to a corresponding modification of the field-dependent carrier velocities [5]. When the photon penetration depth is larger than the finger spacing, large numbers of carriers are generated deep inside the semiconductor bulk. The drift distances are mainly determined not by the finger separation, but by the penetration depth of the incoming light and are equal to the gap between fingers only for the carriers, which are photo generated just near the surface. The remaining carriers will have much longer drift distances and times to reach the corresponding electrodes. Thus, the impulse response, as the sum of electron and hole currents, is greatly influenced by the slow current component of the holes. Therefore, to take full advantage of small finger spacing, the generation of the carriers has to be restricted only to the surface region of the MSM device, and a thinner active layer is desirable.

In order to reduce the device dark current, several schemes have been suggested to enhance the effective barrier height of InGaAs MSM, such as by growing a thin layer

of a high-barrier height material on top of the active InGaAs layer [6, 7]. One of these designs incorporates a thin lattice-matched InAlAs top layer that has a barrier height of 0.65 eV. The effective barrier height obtained from the InAlAs layer limits the dark current. However, the collection of the photogenerated carriers is limited, because InAlAs layer introduces higher barriers in the band structure for electrons and holes, and the performance of the device is degraded.

By increasing the responsivity, it is feasible to manufacture photodiodes sensitive to low-light levels [8]. This can be accomplished by suppressing surface recombination through passivation to minimize surface reflections. Therefore, a greater percentage of the incident light is collected to improve the carrier lifetime and to better understand the internal gain mechanisms. To minimize the effect of carrier trapping, which maybe caused by a large band discontinuity at the InAlAs/InGaAs interface, a graded superlattice (200 nm thick) is incorporated between the InAlAs and InGaAs layers. This superlattice is composed of pairs of ultra-thin (one to nine atomic layers) InAlAs/ InGaAs layers, where the width ratio varies so that the effective bandgap is graded linearly in depth, as shown by dotted lines in Figure 6.1 [9, 10].

Both InAlAs and InGaAs layers are lattice matched to InP substrate, which avoids the nonradiative recombination centers originating from strained layers or superlattice interfaces.

From the above, we know that a thin active layer is necessary to improve the speed, a thin surface InAlAs reduces the dark current, and a superlattice is helpful for increasing the responsivity. The interaction of each layer and the thickness of the layers

on the characteristics are still being investigated. Such a high-speed MSM will be used in for high-speed optical interconnections.

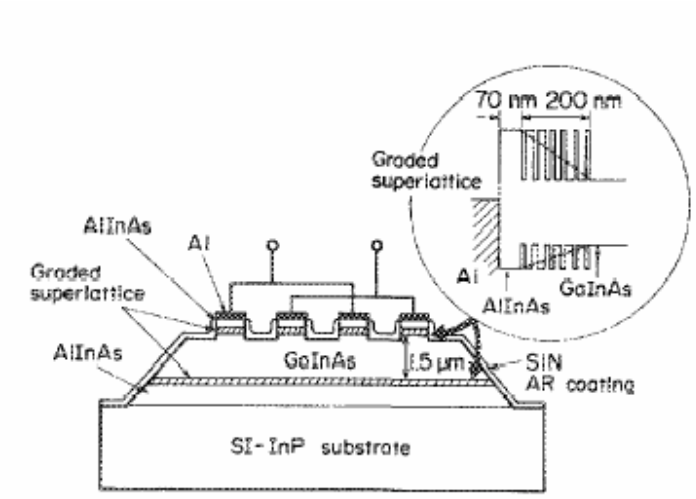

Figure 6.1. Structure and band diagram of InGaAs MSM [10].

6.2 The Growth of InGaAs MSM Devices

A generic InGaAs MSM structure is shown in Figure 6.2. The etch stop layer is used to protect the material during the lift-off process and stop the etching to remove the substrate. The supporting layer increases the total thickness of the material for convenient fabrication. The InAlAs layer is used to increase the barrier height of MSM. The big band gaps between InGaAs and InAlAs can trap defects. A graded layer is used to modify the band structure, and minimize the trapping defects. The interaction of each layer and the thickness of the layers on the relevant device characteristics are investigated in this work.

The growth temperature is 400^0C, and the growth rate is ~0.4 μm/hour, which has to be carefully calibrated, because the digital layer is ultra thin, as mentioned in previous

section. A detailed structure of 20nm grade layer was shown in Figure 6.2. It takes only a few second to grow one layer. The growth rate is determined by chemical selective etching, measuring the film thickness grown in a certain time.

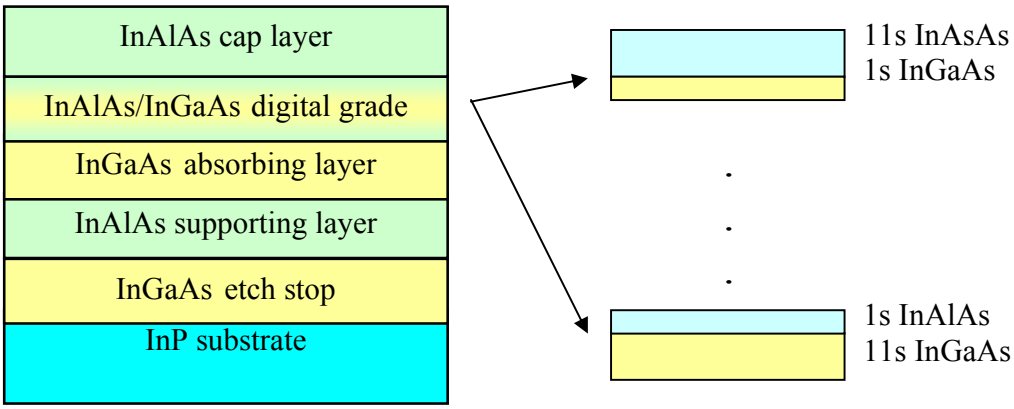

Figure 6.2. Material structure of InGaAs high-speed MSM.

All the materials are lattice matched: $In_{0.53}Ga_{0.47}As$ and $In_{0.52}Al_{0.48}As$ are lattice matched to the InP substrate. They are all n-type materials. The carrier concentration and mobility are $5\times10^{-15}/cm^3$ and $6000cm^2/v\text{-}s$ for InGaAs, and $5 \times 10^{-14}/cm^3$ and $1000cm^2/v\text{-}s$ for InAlAs, respectively.

A series of samples was grown; some were grown by Jeng-Jung Shen [11].The detailed structure of each sample is listed in Table 6.1. The cap InAlAs is used to increase the barrier height and the grade layer can minimize the dislocation density, thus both can decrease the dark currents of MSM device. But their thicknesses on speed and responsivity are not clear, which varied in our experiments for further investigation. Thin InGaAs absorbing layer improves the speed but degrades the responsivity. It thickness is varied from 0.5-0.7 μm to find the balance. The effect of InAlAs supporting layer on the

device property is unknown, and the thickness is from 0.5 to 1 μm in our experiment . The etching stop layer is 0.2 μm.

TABLE 6.1.Material structures of high-speed MSM for optimization.

thickness (nm) / structure	R159	R217	R218	R317	R318	R223	R232	R226
InAlAs	10	40	40	40	40	40	50	50
Grade	0	20	20	20	20	50	50	50
InGaAs	100	100	200	300	300	500	200	100
InAlAs	500	1000	1000	1000	500	500	700	700
InGaAs	200	200	200	200	200	200	200	200

6.3 Characterization and Integration of High-speed MSM Device

The devices are fabricated and tested by Prof. Nan M. Jokerst's group [11]. The picture of MSM detector was shown in Figure 6.3, the sizes of the finger and gap are both 1 μm. The active area is a circle with 20 μm diameter. The detector was bonded on a high speed pad for testing.

The dark currents were first measured and shown in Figure 6.4. The difference is obvious for different material structures. The one without digital grade layer (R159) has

the maximum dark current, proved that grade layer could minimize the defects caused by the big bandgap between InGaAs and InAlAs.

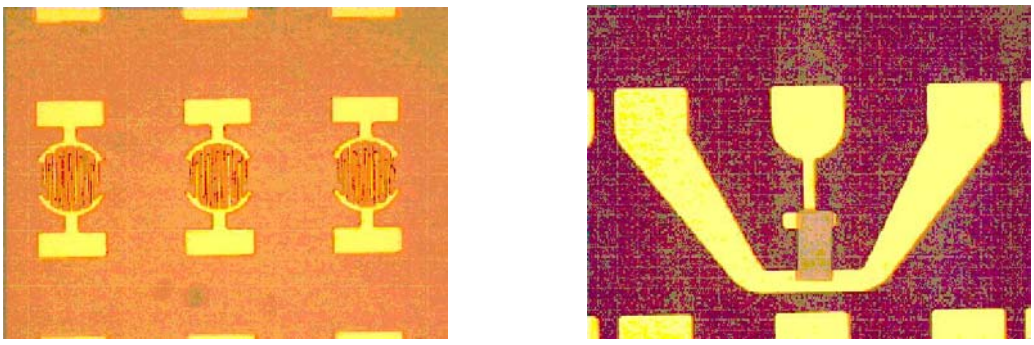

(a) (b)

Figure 6.3 (a) Thin film I-MSM detector 20 mm diameter 1/1 mm finger/gap. (b)Thin film I-MSM detector on high speed GSG pad for device testing.

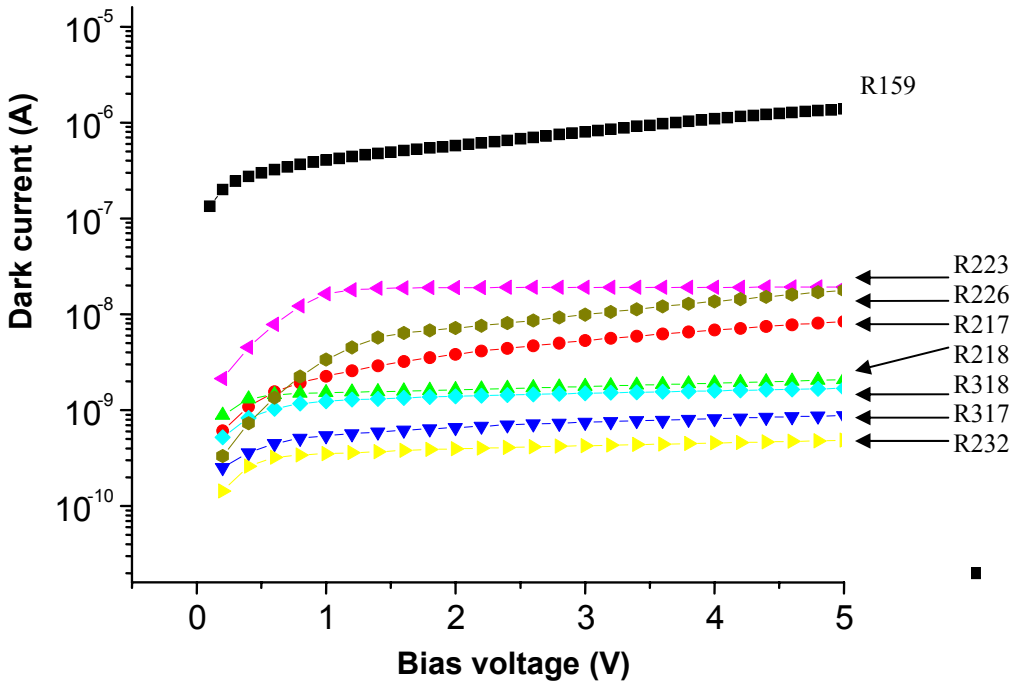

Figure 6.4. Dark currents of all the samples.

The difference between R317 and R318 is the thickness of the InAlAs supporting layer. The one with thinner supporting layer (500nm of R 318) has larger dark current, which is as twice as of R317.

The difference in the material structure for sample R217, R218 and R317 is the thickness of absorbing layer. The one with thickest InGaAs layer (300nm of R317) has the lowest dark current, which is 1.68 nA at 5 volts of bias voltage.

Compared R223 and R318, the dark current of R223 is higher, though it has a thicker absorbing layer, it also has a thicker grade layer. Thus the thicker grade layer results in larger dark current.

Compared R223 and R232, the absorbing layer and cap layer of R223 are thicker and thinner than R232, respectively, and its dark current is higher than R232, indicating that the thicker cap layer results in larger dark current.

For a device with low dark currents, the requirements for the material structure are thicker InAlAs supporting layer and InGaAs absorbing layer, and thinner grade layer and cap layer. So R232 has the lowest dark current.

The responsivity was also measured. The comparison showed that thick InGaAs absorbing layer, and thin grade layer and cap layer are helpful to improve the responsivity; but the effects of the InAlAs supporting layer is not obvious.

The impulse response was measured using a set up of a 50 GHz sampling oscilloscope, as shown in Figure 6.5 (a), and the measured impulses response of one sample was shown in Figure 6.5 (b).

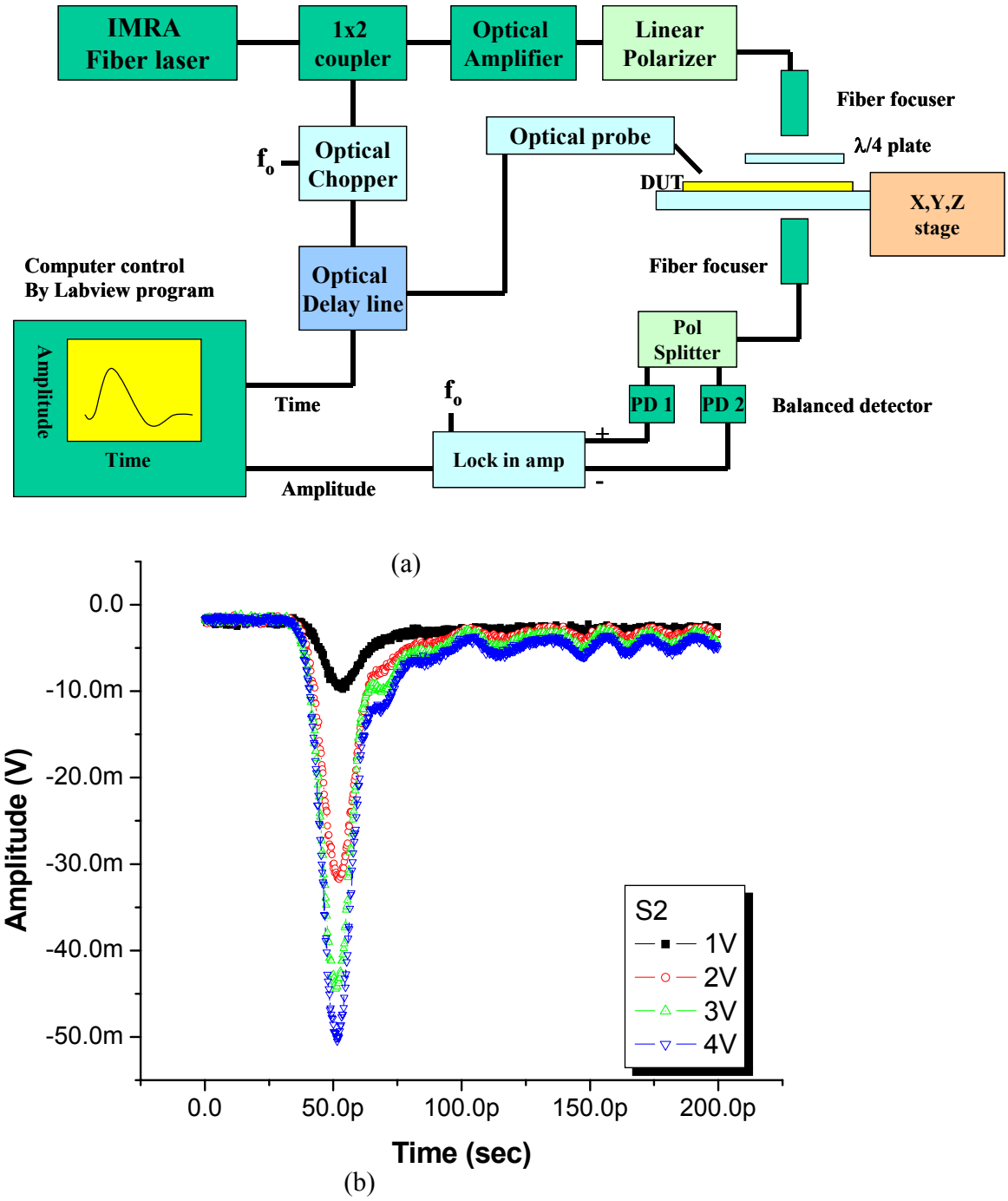

Figure 6.5 (a) Impulse response measurement set up, using a 50 GHz sampling oscilloscope. (b)The measured impulse of R217, FWHM=14.3 ps, rise time (10% to 90%)= 10.4 ps and fall time (90% to 10%)= 22.85 ps [11].

The rising time is defined as from where the intensity is 10% of the peak to when 90% of the peak. The falling time is defined as the opposite. The speed of the device is determined by the sum of rising time, falling time and FWHM. High-speed devices require short time response. The experiments showed that the response time was affected by applied voltage, and high voltage results in fast speed, as the same as indicated in previous section. All the measured results are listed in Table 6.2. By comparison, it is found that the sample with thin InGaAs absorbing layer, thin InAlAs supporting layer, thin grade layer, and thick cap layer result in short time and high speed.

Table 6.2 Characteristics of high-speed MSM with different material structure.

Material structure and characteristics	R217	R218	R317	R318	R223	R232	R226
InAlAs Cap (nm)	40	40	40	40	40	50	50
Grade (nm)	20	20	20	20	50	50	50
InGaAs Absorbing (nm)	100	200	300	300	500	200	100
InAlAs Supporting (nm)	1000	1000	1000	500	500	700	700
InGaAs (nm)	200	200	200	200	200	200	200
Dark current (nA) (5V)	8.4	2.1	0.87	1.68	3.71	0.48	17.82
Responsivity (A/W) (5V)	0.094	0.164	0.376	0.39	0.42	0.29	0.093
FWHM (psec)	14.3	13.2	14.5	16.9	13.9	14.05	15.65
Rise time (psec)	10.4	9.45	10.9	11.3	9.7	9.86	11.23
Fall time (psec)	22.85	45.5	48.5	36.45	77.9	34.05	95

Sample R217 has the shortest response time (47.5 ps), its responsivity is 0.09 A/W. With increasing the thickness of absorbing layer (R318), the response time

increases to 64.2 ps, but the responsivity increased to 0.39 A/w. Our device is comparable with the commercial ultra-fast MSM [12], which has the response time at 10V from 40 to 100 ps, and responsivity from 0.2 to 0.4 A/w.

The integration was as the same as the integration of GaN MSM, except that it was bonded on metal/BCB/glass substrate. The properties after bonding were not degraded.

In summary, from the above measurements and discussion, low dark current, high responsivity and high speed could not be achieved at the same time, as shown in Table 6.3. Two of the desired properties for photodetectors in current telecommunication technologies are high quantum efficiency and short response time. But high efficiency, high speed and large detection area involve trade offs, due to the facts that increasing the absorbing layer thickness for high responsivity is inversely proportional to the response time of the photodetectors. Depends on the application as optical interconnects, the optimized material structure should insure the device with high speed but reasonable responsivity. It was also found that thick supporting layer is hard for integration because of curling. So for future research, the supporting layer is targeted at 500nm, the cap layer at the thickness of 200nm, grade layer at 20nm, and absorbing layer at 100-300nm.

Table 6.3 Summary of the relationship between device characteristics and material structure.

Material structure and characteristics	**Low** dark current	**High** responsivity	**High** speed
InAlAs	Thin	Thin	Thick
Cap	Thin	Thin	Thin
Grade InGaAs Absorbing	Thick	Thick	Thin
InAlAs Supporting	Thick	x	Thin

6.4 References:

[1] L. Figueroa and C. W. Slayman, IEEE electron Device Lett. **EDL-2**, p208-210, (1981).

[2] M. Ito and Owada, IEEE J.Quantum Electron., **QE-22**, pp1073, (1986).

[3] D. Soole and H. Schumacher, IEEE J. Quantum Electron., **27**, 737 (1992).

[4] S.Y. Chou, and M.Y. Liu, IEEE, J. of Quantum Electron., **28**, 2358-2368, (1992).

[5] B. S. Averin, R. Sachot, J. Hugi, M. De Fays, and M. Illegems, J. Appl. Phys. **80** (3), 1553, (1996).

[6] O. Wada, H. Nobuhara, H. Hamaguchi, T. Mikawa, A. Tackeuchi, and T. Fujii, Appl. Phys. Lett. **54**, 16, (1988).

[7] H.T. Griem, S. Ray, J. L. Freeman, and D.L. West, appl. Phys. Lett. **56**, 1067, (1990).

[8] D. Leonard, M. Krishnamurthy, C. M. Reaves, S. P. Denbaars, and P. M. Petroff, Appl. Phys. Lett. **63,** 3203 (1993).

[9] D. Pan, E. Towe, and S. Kennerly, Appl. Phys. Lett. **73**, 1937 (1998).

[10] S. Sauvage, P. Boucaud, J. M. Ge´rard, and V. Thierry-Mieg, Phys. Rev. B **58**, 10562 (1998).

[11] S. Seo, unpublished thesis.

[12] The report from Hamamatsu company.

C H A P T E R 7

DESIGN, GROWTH, AND CHARACTERIZATION OF INAS QUANTUM DOT PHOTODETECTORS

Along with the continued shrinking of device dimensions in Si VLSI, the task of exploring and understanding new device structures that are based on quantum mechanical effects has become increasingly important. These devices possess critical dimensions smaller than the phase coherent mean free path of electrons, which is estimated to be on the order of 500 Å in Si at room temperature. The need for novel device structures and technology is well recognized by the semiconductor industry which has called for the research and development of novel device structures that are non-lithographically defined. One such group of devices is based on semiconductor islands that are formed during hetero epitaxial growth, also known as self-assembled quantum dots (SAQD). Quantum dot or island formation is driven by the compressive strain that is present in hetero-structures such as InAs on GaAs substrate and Ge on Si substrates. In this chapter, the history and fundamental theory of QDs' are introduced. A study on the growth conditions and material structures for far-infrared photodetector is then presented.

7.1 Introduction of Quantum Dot

It is called “particle in a box” in elementary quantum mechanics: a particle such as an electron in a potential that is zero within some region and finite outside of the region. The wavefunction of the electron can take on only certain standing-wave patterns, with a corresponding discrete set of energy levels. In other words, the energy of the electron is quantized by the potential well [1], as shown in Figure 7.1.

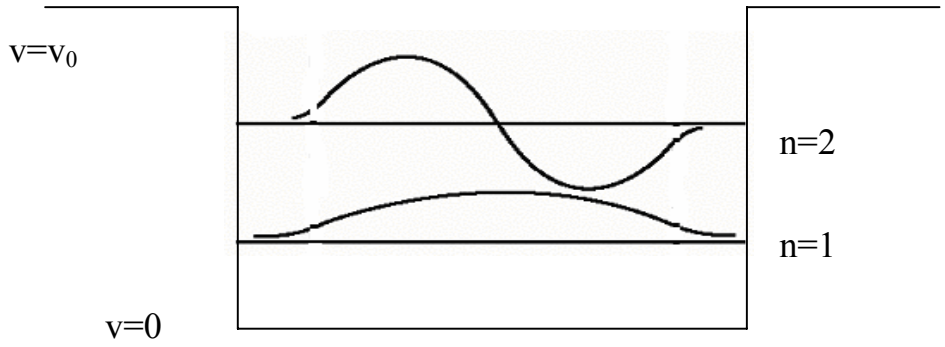

Figure 7.1.Quantized energy for a particle in box.

Remarkably, it is possible to fabricate semiconductor structures that are well approximated by this potential-well model with semiconductor heterostructures of more than one semiconductor material. The states of electrons and holes in these structures can be described using a modified version of Bloch's theorem, where the particle wavefunction $\varphi(\vec{r})$ is written as a product of a periodic part $u(\vec{r})$ and an envelope wavefunction $\chi(\vec{r})$ [2]:

$$\varphi(\vec{r}) = u(\vec{r})\ \chi(\vec{r}) \tag{7.1}$$

The Bloch function repeats with the periodicity of the lattice. For the material GaAs and

InAs, $u(\vec{r})$ is an s-like wavefunction for electrons in the conduction band, and is a p-like wavefunction for holes in the valence band. The envelope function $\chi(\vec{r})$, on the other hand, can often be described using the effective-mass approximation:

$$(-\frac{\eta^2}{2m^*}\nabla^2 + V(\vec{r}))\chi(\vec{r}) = E\chi(\vec{r}) \qquad (7.2)$$

where E is the carrier energy. This equation of motion is equivalent to the ordinary Schrödinger equation, except that the particle mass is replaced by an effective mass m^*, and the potential $V(\vec{r})$ corresponds to the energy of the appropriate band edge, which is the bottom of the conduction band for electrons, and the top of the valence band for holes.

Thus, the potential profile of the "particle in a box" can be simulated by a variation in bandgap. A quantum well consists of a thin sheet of a semiconductor material with a lower bandgap inserted between layers of a semiconductor material with a wider bandgap. Carriers are trapped in the low-bandgap material by the effective potential well. If the thickness of the layer is small enough, carriers form standing waves can only occupy discrete energy levels. The quasielectric fields created by bandgap variations allow both electrons and holes to have potential minima in the same location that sometimes is not possible with real electric fields.

All the carriers (electrons and holes) in a quantum well will be in the lowest quantum-confined state at low enough temperatures. The carriers are free to move, however, in the plane of the well. The well is referred to as a quasi-two-dimensional system, since the carrier motion has been effectively restricted to a plane. The corresponding density of states shows a staircase pattern. The density of states can be

made more singular if the effective number of dimensions is reduced to one, in a quantum wire, or zero, in a QD, as shown in Figure 7.2.

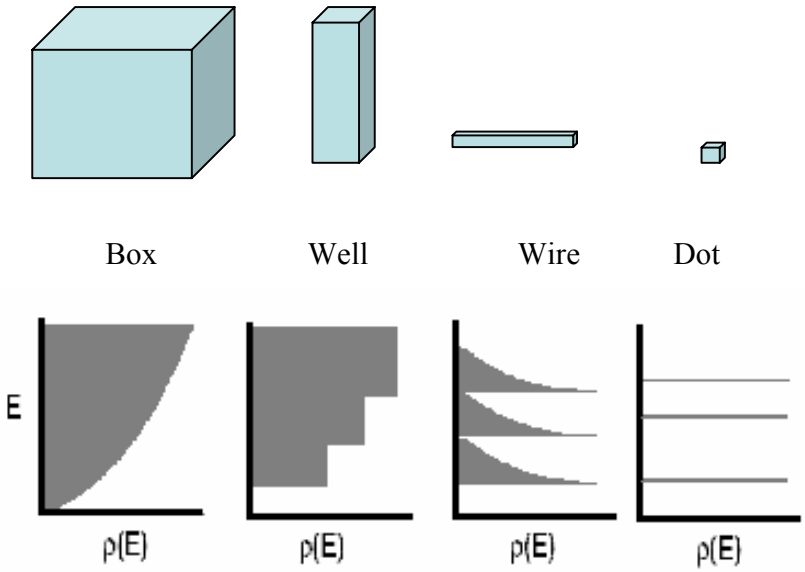

Figure 7.2 Semiconductor heterostructures and corresponding densities of states.

In a quantum dot, the energy levels are fully quantized, as in an atom. Optical transitions between the valence band and the conduction band can thus occur only at discrete energies. The bound electron states of the quantum dot take the form of a set of discrete atom-like orbitals. Unlike atoms, however, the confining potential of a quantum dot takes the form of a three-dimensional box, rather than the central nuclear potential of the atom. In addition, electrons in a quantum dot are subject to scattering by phonons in the crystal lattice.

Modern lithographic techniques have made possible the fabrication of quantum dots with sizes as small as 50-100 nm [3]. One problem with the etching process used to define such dots is that it introduces defects into the crystal lattice. An alternative way of

producing nanometer-sized QDs was developed based on crystal growth techniques (MBE or MOCVD) [4].

Epitaxial growth of lattice-matched material can proceed according to two different growth modes, as illustrated in Figure 7.3. Layer-by-layer growth is also known as Frank-van der Merve growth. It occurs when the sum of the epitaxial surface energy and the interface energy is less than the substrate surface energy. If the energy balance is reversed, it is favorable for the epitaxial material to form small islands on the surface. This is known as the Volmer-Weber growth mode.

For epitaxial growth of lattice-mismatched material, it is necessary to consider strain energy as well as surface and interface energies. Growth can initially proceed in a layer-by-layer mode. However, the unit cells of the epitaxial material will be distorted in order to conform to the lattice constant of the substrate, leading to strain in the epitaxial layer. The energy associated with this strain increases as the layer thickness increases. Island formation will be favorable if the energy lost by strain reduction is greater than the energy associated with the additional surfaces [6]. Deposition of a planar wetting layer followed by three-dimensional islands is known as the Stranski-Krastanov (SK) growth mode. Islands compete with dislocation as a mechanism for relieving strains. If the energy lost by forming islands is greater than that lost by formation dislocations, coherent islands are possible to grown. Under certain conditions, deposition of InAs on GaAs leads to just such dislocation-free islands. The islands have dimensions on the order of several nanometers, making them suitable for use as quantum dots [7-9]. GaAs deposited on top of the dots forms a planar layer, resulting in a small inclusion of InAs inside a matrix of GaAs. Such self-assembled dots have been extensively studied recently, both

for their physical interest and potential applications [10].

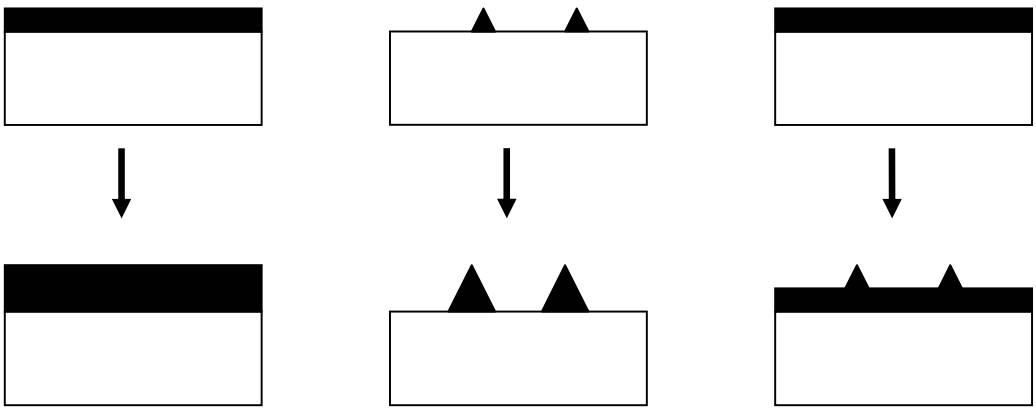

Figure 7.3 Modes of epitaxial crystal growth: (a) Frank-van der Merve, (b) Volmer-Weber, (c) Stranski-Krastanov (S-K)

The equilibrium picture of quantum-dot formation presented above is not a complete account of how dots form in MBE. It is also necessary to consider the atomic kinetics involved.

The driving force for the SK growth is the reduction of the elastic strain energy due to lattice mismatch. It is counter-balanced by the increase in the surface energy. The wetting layer far away from the island experiences the misfit strain: $\varepsilon=(a_0-a_{wetlayer})/a_0$, where $a_{wetlayer}$ is the lattice constant of the wetting layer, and a_0 is the lattice constant of the layer beneath the wetting layer. The islands are formed to decompose the thick wetting layer and relieve the strain. The strains and energy around the island is shown in Figure7.4 [11]. The strain beneath the island area is low, while higher strain exists around the island. Correspondingly, there is a peak in the strain energy distribution, as shown in Figure 7.4 (c). The low strain and strain energy well along the surface layer of the island

is formed due to the strong relaxation underneath QD, and the strain transformation between region A and region B. The peak in the strain energy distribution forms an energy barrier of height E_1 to mass transport on the surface. The atoms form the outside region must overcome this barrier to diffuse onto the island (island growth). By the same time, the atoms also have to overcome a barrier E_2 to diffuse away from the island. (island shrinkage). When the island grows bigger, the energy barrier increases, and fewer atoms are able to surpass the barrier. As a result, the growth of the larger islands is decreased in comparison to the smaller ones, narrowing the island size distribution.

When the island size is small, there is a great amount of surface energy in the dot structure. This causes the dot structure to have a strong tendency towards the thermodynamically stable state. The minimization of surface energy is realized via ostwald ripening. Due to the self-limiting effect, smaller island grow faster and hence a narrow size distribution may be expected. The phenomenon of the changing in the island size may be related to the reduction of the critical thickness of the wetting layer. Reduction of the critical thickness caused larger island size [12].

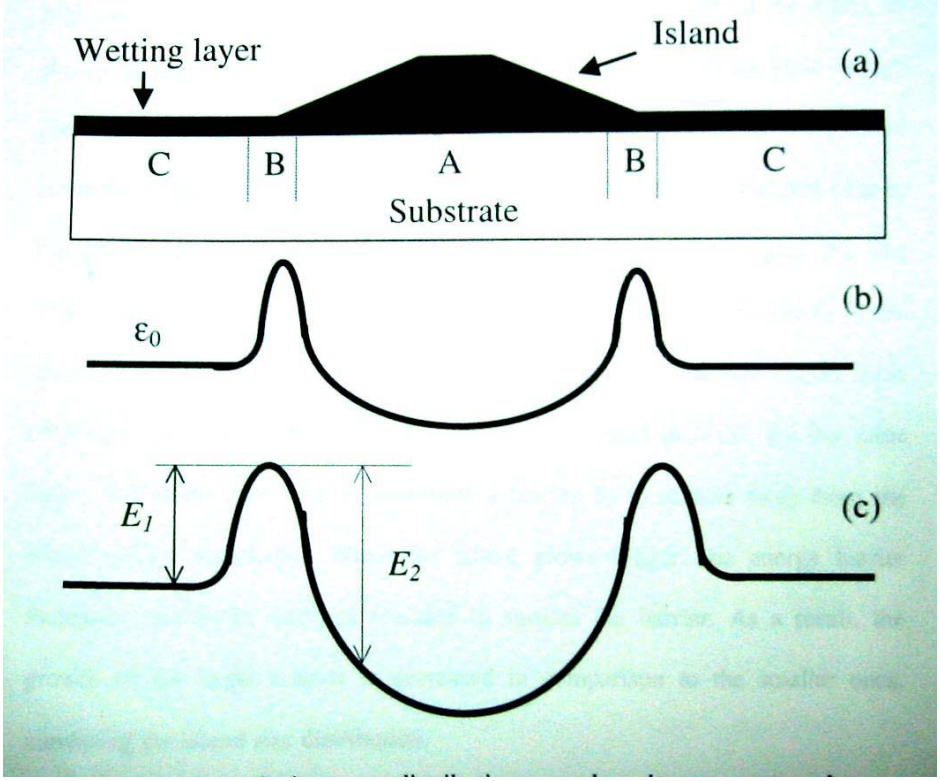

Figure 7. 4. Strain energy distribution around a coherent quantum dot [11].

Three factors that strongly influence the size and density of self-assembled dots: the temperature, the deposition rate and the surface diffusion constant. All these parameters are coupled, and it might not be possible to vary them independently to get a clear picture of the growth. However, by hand-waving arguments it is possible to gain some basic feeling for the overall trends.

The island density increases rapidly with increasing amount of deposited material, up to a saturation point, after this point the density is rather constant [13]. With a constant deposition rate, the following relations are of importance: the distance between nuclei will follow the surface diffusion length, when the wetting layer has passed the critical thickness and 3D nucleation is possible. Since the surface diffusion length in most cases

will increase with increasing temperature and decrease with increasing deposition rate, the density will increase with increasing deposition rate and decreasing temperature.

The density and size of quantum dots is partially determined by the balance between the rates of adsorption and diffusion of In atoms on the sample surface. If adsorption occurs slowly compared to the surface diffusion, the surface approaches thermal equilibrium at each moment during growth. This leads to a layer of dots with relatively low density and large diameters. On the other hand, if adsorption is faster compared to diffusion, the kinetics is frozen out. In atoms will tend to aggregate into dots with additional atoms and they are adsorbed nearby rather than with more distant atoms, resulting in a higher density of smaller dots for the same amount of adsorbed material. The balance between adsorption and diffusion can be changed by increasing the InAs growth rate, or by increasing the V/III ratio, which leads to a lower diffusion rate. However, more dramatic differences occur when the substrate temperature is changed. A higher substrate temperature leads to a higher diffusion rate. At the same time, it increases the inter-diffusion of adsorbed In atoms and underlying Ga atoms. The epitaxial quantum-dot layer is thus an InGaAs alloy, with a Ga fraction that increases with temperature. A higher Ga content means that the epitaxial layer has an effective lattice constant closer to that of the GaAs substrate. This, in turn, means that the strain energy that drives the islanding process is reduced. This combines with the decreased surface diffusion to produce larger, sparser islands.

Surface roughness is another parameter that greatly influences the density of islands. A rough surface affects both the diffusion constant and the number of favorable

nucleation sites. The result is that the density of dots increases with increasing surface roughness, the height of the dots is correspondingly smaller.

7.2 Quantum Dot Far Infrared Photodetector (QDIP)

The interest in infrared photodetectors is connected to the development of a class of devices based on intersubband transitions, including quantum-well and -dot infrared photodetectors. The advantages of quantum dot infrared photodetectors (QDIP) are its normal-incidence detection, high-temperature operation, high gain, high differential gain associated with low threshold currents, good high-speed characteristics, etc. The main disadvantage of the QDIP is the large inhomogeneous linewidth of the quantum-dot ensemble resulting from random variation of dot size in the SK growth mode. As a result, the absorption coefficient is reduced [14-18].

The basic structure of QDIP is shown in Figure 7.5. A relaxed buffer layer is grown first. A superlattice layer is also preferred to relieve stress. Incidentally, the wavelength of a quantum structure could be tuned by changing the residual strain [19]. For the quantum-dot structure, the first barrier has to be wide enough to reduce spatially indirect absorption between the quantum dot plane and the first quantum well. The barrier between the two quantum wells has to be thin enough to reduce the time spent by the electron in the first quantum well and thus reducing the chances of the electron being scattered [20]. If the quantum dots layers are repeated over several periods, the responsivity will increase. However, it is suggested that a superlattice structure with as small a number of quantum dot layers as possible can avoid the dislocations in practical

device structures [21]. It is shown that the ratio of the responsivity and the dark current pronouncedly decreases with decreasing QD densities [22]. A current blocking barrier is necessary to decrease the dark current [23]. A contact layer of GaAs is finally grown.

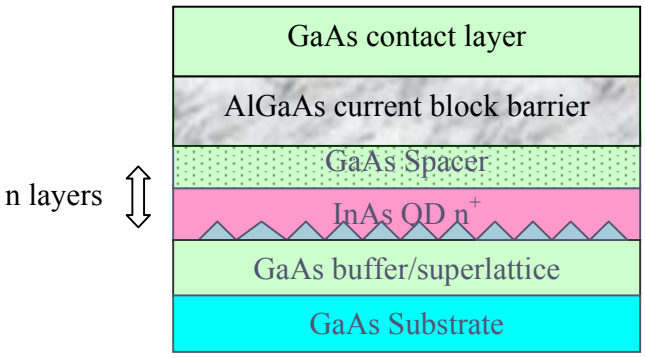

Figure 7.5. A basic structure of QDIP.

Far-infrared (5-20μm) photodetectors are found useful in the application of night vision, navigation, flight control, thermal imaging, early warning systems, and space research. Narrow-bandgap materials are the state of the art in long-wavelength far-infrared photodetectors [24,25]. Quantum dot photodetector and laser have been reported by a few groups to be operated at very low temperature with wavelengths around 13 μm [26, 27].

Quantum dots should fulfill the following requirements in order to make them useful for devices at room temperature [10]:

(1) Sufficiently deep localized potential and small dot size is a prerequisite for obdervation and utilization of zero-dimensional confinement effects.

(2) Quamtum dot ensembles should show high uniformity and a high volume filling factor.

(3) The material should be coherent without defects like dislocations.

The lower size limit of a quantum dot is due to the condition that at least one energy level of an electron or hole is present. The critical diameter depends strongly on the band offset of the corresponding bands in the material system used. An electron level exists in a spherical quantum dot if the confinement potential, defined by the conduction band offsets ΔE_C, exceeds the value [10]:

$$D_{\min} = \frac{\pi\eta}{\sqrt{2m_e^*\Delta E_C}} \tag{7.3}$$

where m_e^* is the effective electron mass. Assuming a condition band offset value of ~0.21 eV [28] for InAs/GaAs heterostructures, the diameter of the quantum dot should be larger than 5nm. This is the lower limit of the dot size. Within a quantum dot with this or slightly larger size, the separation between the electron level and the barrier energy is very small. At finite temperature, thermal excitation of carrier from quantum dots will result in their depletion. This is one potential disadvantage. In reality, the shape of quantum dot is more like a pyramid rather than a perfect round.

The issue of uniformity exists when a device is operated on the base of multiple quantum dots. Ideally, a dense array of dots with the same size and shape is desired. The main effect of size fluctuation is the variation in the energy position of electronic levels, which will affect the wavelength of the quantum dot photodetector. Such variation is typically Gaussian. For the device that relies on the integrated gain in a narrow energy range, the inhomogeneous energetic broadening should be as small as possible. Thus, for a given average size of the dots, the smallest possible size and shape fluctuation values are the major concerns. Furthermore, if wavelength multiplexing is desired, a certain width of the distribution of energetic levels is critical. Typically, a minimum number of

dots is necessary to obtain a given performance and overcome the losses.

The density of defects in a quantum dot material and its interface to the surrounding material should be as low as possible. Through SK growth mode, MBE-grown quantum dots have been proved the ability to produce defect-free quantum dots [26].

Severe problems are still associated with epitaxial growth and nonuniformities. The random variation of dot size causes poor device performance, and the far-infrared quantum dot laser and photodetectors can be operated only at low temperature. The wavelength of QDIP needs to be tuned. The size of the dots size determines the electron levels, and the wavelength of the photodetector. By controlling the dot size, the wavelength can be tuned.

Many research efforts have reported on modifying dot sizes, improving the uniformity, and tuning the wavelength of the detector. Examples are to:

- Vary the growth rate and substrate orientation [29]
- Vary the thickness and change the annealing conditions of the dots[30];
- Vary the thickness of the spacer [31];
- Change the superlattice cycles and modify the interface roughness[32,32];
- Optimize the structure by adding an InAlAs/InGaAs/AlGaAs top layer [34,35]

Much research is still needed in this field.

7.3 Optical Transitions in Self-Assembled Quantum Dots

The GaAs crystal is a zinc blende structure. The Ga atoms occupy the sites on one of the sub-lattices, and As occupies the sites on the other. The in-plane lattice constant is 0.5653 nm [5]. The band gap between the bottom of the conduction band and the top of the valence band is 1.42 eV at room temperature. InAs has the same crystal structure as GaAs and has a lattice constant of 0.6058 nm. InAs has a direct bandgap of 0.354V, which allows for efficient optical transitions.

The bandgaps of InAs and GaAs the two materials line up such that a large potential well is formed for both electrons and holes. The dipole moment of the atoms in the dot effectively adds up to create a single dipole with large oscillator strength. Finally, the energy of transitions between confined states in the dots lies in the near infrared, allowing for efficient photon detection.

Our principle tool for investigating optical emission from quantum dots is photo-luminescence (PL). This process is illustrated schematically in Figure 7.6. Laser light is directed towards the sample, leading to the production of electron-hole pairs. The energy of the incident light may be larger than the GaAs bandgap; this is what we call above-band excitation. In this case, many electron-hole pairs are created in the GaAs matrix surrounding the dot. The carriers diffuse towards the dots. At low temperature, they are rapidly trapped by the dots, and quickly relax to the lowest-energy confined states [34]. They then recombine to emit a photon with a characteristic energy. Alternatively, the incident light can be tuned such that the photon energy is equal to the energy difference between higher-lying states in the dot; this is called resonant excitation. In this case, the diffusing and trapping steps from the GaAs are avoided, and electrons

and holes are always created in equal numbers directly in the dot.

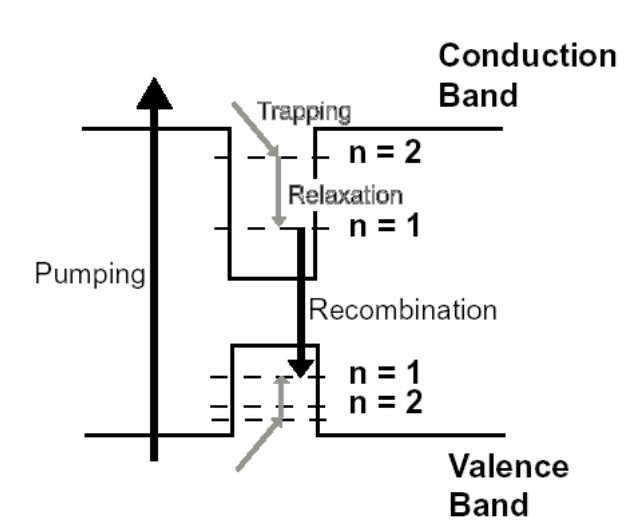

Figure 7.6 Schematic of transitions in an InAs/GaAs quantum dot.

Figure 7.7 shows a schematic of the experimental apparatus used for PL measurements. The sample is held at a low temperature of 77-150 K in vacuum. The low temperature is maintained by a continuous flow of liquid nitrogen. The laser beam is incident on the sample, and lenses are used to focus pump light onto the sample. The pump source is a Ge laser. Following the lenses, the light is received by a detector array, which is cooled with liquid nitrogen to minimize noise. The array consists of several columns of pixels, so that a range of wavelengths can be detected simultaneously.

The PL measurement is related to the wavelength of the fabricated quantum dot photodetector. It has been demonstrated that with changing the formation of dots, when the intersuband absorption wavelength for InAs/GaAs quantum-dot infrared photodetectors is blue shifted, the PL peak is red shifted [35]. Thus, PL is an important tool for characterization of quantum dot materials.

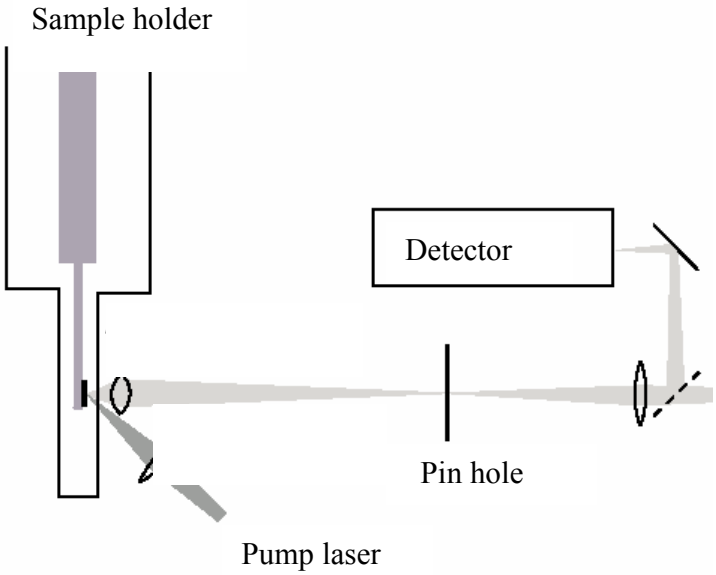

Figure 7.7 Schematic of Photoluminescence measurement.

7.4 Annealing Experiments

Many experiments have been reported on the annealing of InAs quantum dots. Annealing dot layers under similar and dissimilar anion fluxes can help to understand the fundamental relationship between strain and surface exchange kinetics [11]. Since quantum dot formation is strain-dependent, understanding and exploiting the strain kinetics help us better able to control the influence of strain on mismatched epilayer during MBE growth.

In this work, we performed a series of experiments by annealing the spacer, the layer between two quantum dots. The dot size was affected, as was the observed PL transitions. X-ray simulation show that the annealing step changes the quantum dot size

and density. The current blocking layer, AlGaAs layer used to enhance the bandgap, was also annealed.

In our experiments, InAs quantum dots were grown by MBE on semi-insulating GaAs substrates using solid arsenic and phosphorus sources to produce As_4 and P_2. The deoxidation temperature was determined by RHEED observation and assumed to be 580 ^{0}C. A 2500Å GaAs buffer was first grown at the substrate at the deoxidation temperature. A V/III (As_4/In) flux ratio of 18 was used to grow the quantum dots. The growth rate was 0.45 Å/sec. Approximately 3 ML InAs was deposited at 500 ^{0}C; the shutter was closed immediately when observing the spotty RHEED pattern. A 125Å GaAs spacer was grown between the dot layers. The quantum dot layer and spacer were grown for two periods. Finally a 800 Å GaAs cap layer was grown. That is the standard sample for comparison. The material structure is shown in Figure. 7.8 (a).

For some of the samples, after the growth of spacer, the Ga shutter was closed immediately, and the spacer was annealed under As_4 for three minutes at a temperature of 580^{0}C (R461), 500^{0}C (R450), or 350^{0}C (R446). For other samples, the spacer was annealed under P_2 for three minutes at the temperature of 580 ^{0}C (R460), 500^{0}C (R452), or 350^{0}C (R454). The dots and spacer were grown with 2 periods, and the spacer in each period was annealed. The beam equivalent pressures (BEP) of As_4 and P_2 during the anneal period were 2 $\times 10^{-6}$ Torr. Finally the cap layer was grown. These samples are grown for specifically for characterization using PL and x-ray.

To observe the dots formation with AFM, other samples were grown without the top cap layer and spacer, and with a bare quantum dot layer on the annealed or non-annealed spacer, as shown in Figure 7.8 (b).

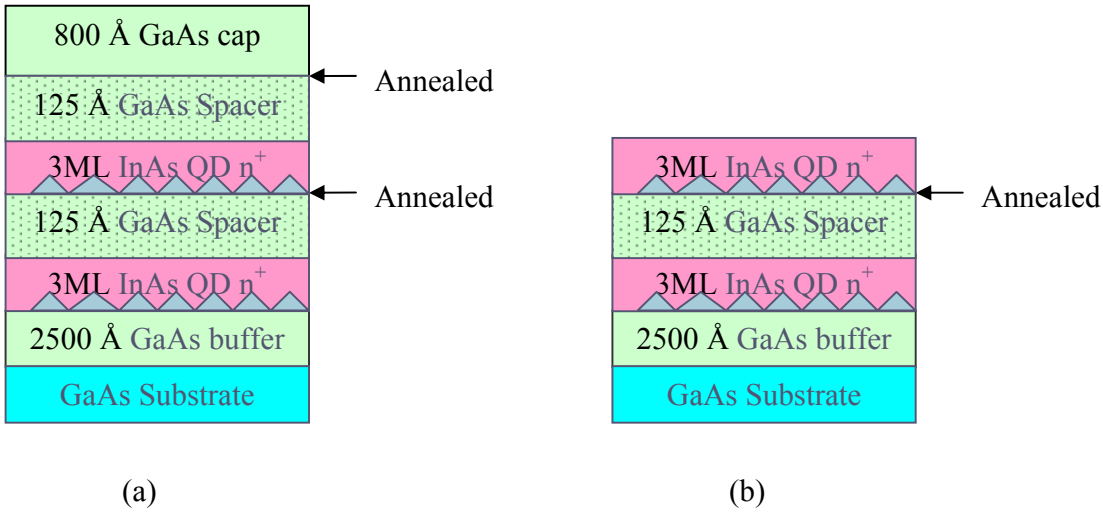

Figure 7.8 (a) Schematics of the material structure for x-ray and PL measurements. The spacer was non-annealed or annealed under different conditions for comparison.(b) Schematics of the material structure for AFM characterization.

It was mentioned earlier that a current blocking barrier is necessary to decrease the dark current [39]. After the growth of two periods of InAs/GaAs, a 500Å $Al_{0.3}Ga_{0.7}As$ layer was grown. The AlGaAs layer was annealed under As_4 or P_2 at 580^0C and 500^0C. Finally a 800Å GaAs cap layer was grown. The schematic of material structure is shown in Figure 7.9. X-ray and PL were used to characterize the effects of annealing the current block layer on the properties of the QD material.

The characterization will be introduced in the following sections.

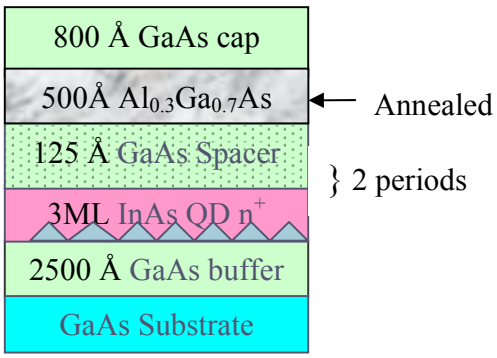

Figure 7.9. Schematics of material structure grown with a current block layer, which was annealed under different conditions.

7.5 Characterization of the Samples with Spacer Annealed under As_4

AFM images of the samples annealed under As_4 are shown in Figure.7.10

Figure 7.10 (a) is the standard surface morphology of 3 ML InAs quantum dots grown on the non-annealed spacer. The dots' diameters are in the range of 35 nm. The dot density is 160/μm^2.

Figure 7.10 (b) is the dots grown on the spacer annealed at 350^0C for three minutes. The diameters of the dots are approximately 50 nm. The dot density is 90/μm^2. Fig. 7.10 (c) is the dots grown on the spacer annealed at 500^0C. The dot sizes are in the range of 35-60nm. The dot density is larger than 250/μm^2. The dots are very dense, but not uniform.

Figure 7.10 (d) is the dots grown on the As_4 annealed spacer. The annealing temperature was increased to the deoxidation temperature, 580^0C, for three minutes. The dots are less uniformed. The diameters are in the range of 30-60nm. The dot density is about 60/μm^2. Compared with the non-annealed sample, this one obviously has the larger

and less dense dots. It has been shown that quantum dot experience an Ostwald ripening process, in which larger islands grow at the expense of smaller island [38].

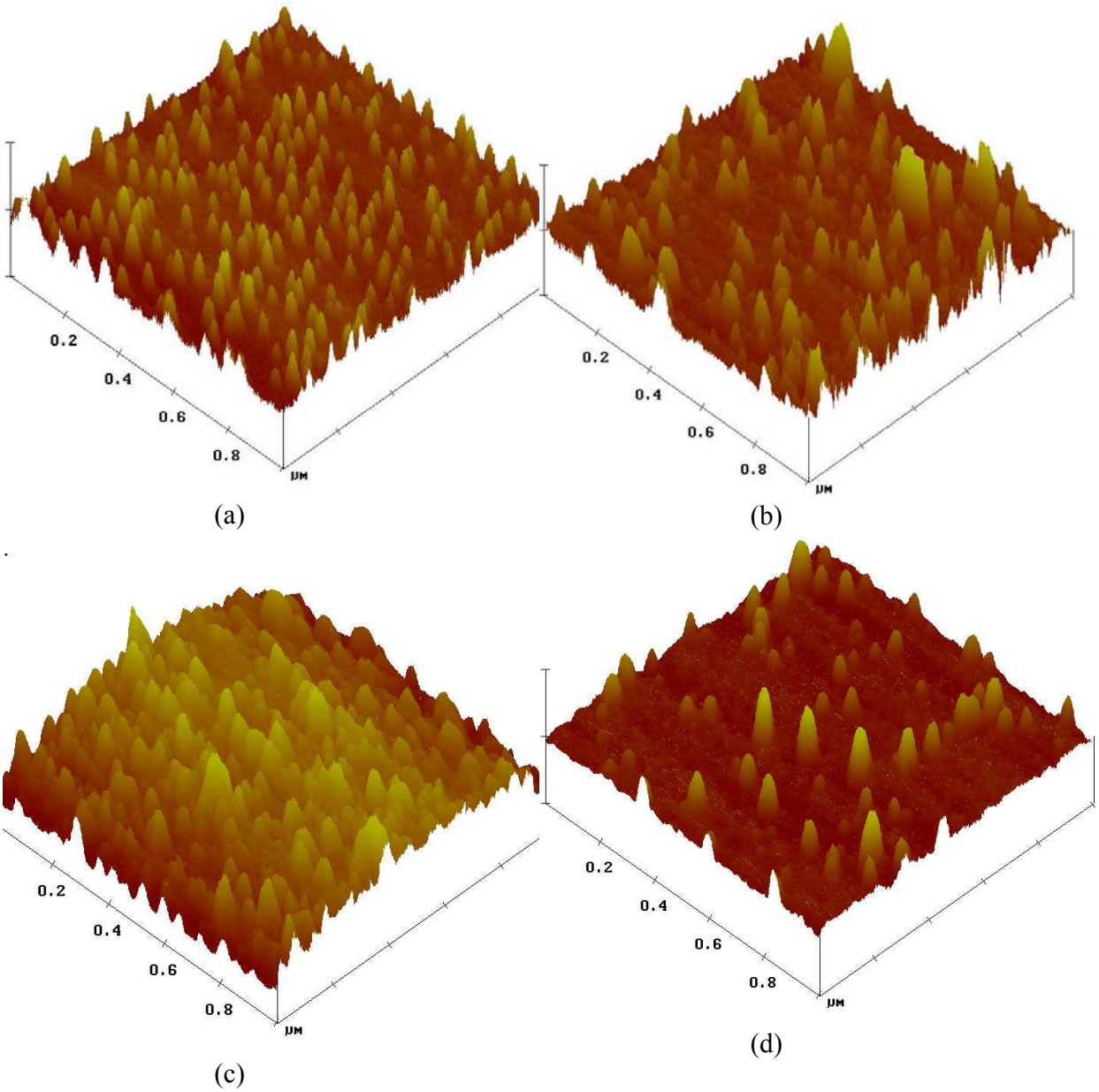

Figure 7.10 AFM pictures of quantum dots grown on the spacer, which was (a) non annealed, (b) annealed under As_4 at 350^0C, (c) at 500^0C, (d) and at 580^0C.

The dot size distribution was shown in Figure 7.11, from where it is found that the one annealed at 500^0C is mostly uniformed.

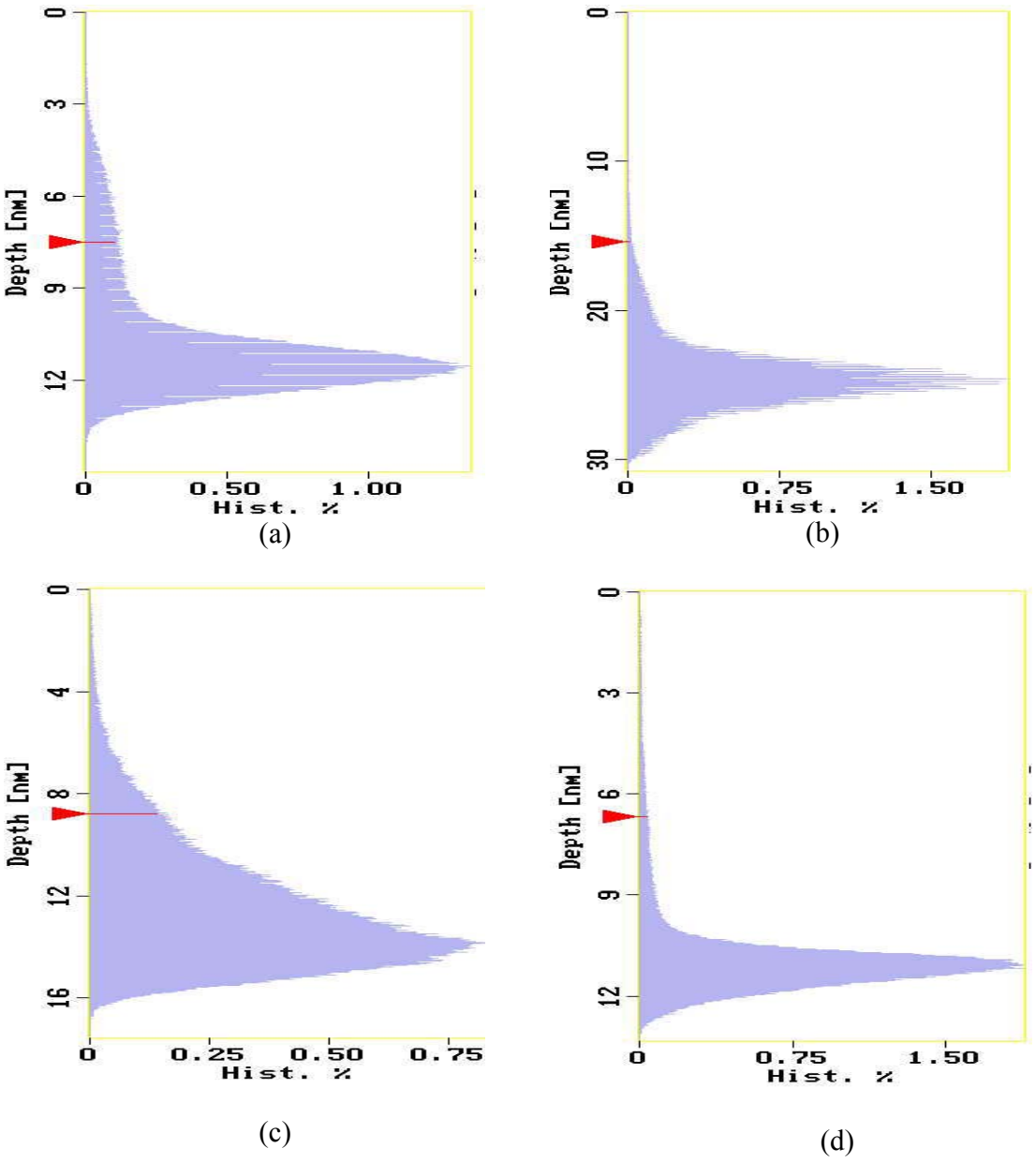

Figure 7.11 Dot size distribution, (a) non annealed, (b) annealed under As_4 at 350^0C, (c) at 500^0C, (d) at 580^0C.

When the spacer is annealed under As_4 at 350^0C, the sample has larger dot size and fewer dot densities. When annealed under As_4 at 500^0C, it has smaller QD size and more QD density. When annealed at 580^0C, Ostwald ripening happened to minimize the strain energy within the small dots. Dots are growing larger (in the diameter), and less dense.

The capped samples were analyzed with x-ray to support the analysis. The ω-2θ x-ray scans of the capped samples in the (0004) direction were shown in Figure 7.12 (a). The peak is the GaAs substrate. The samples with As_4 annealed spacer were compared with the standard, non-annealed sample. The partially strained dots give rise to diffuse scattering in the vicinity of the coherent SL satellites, which to the wetting layer and the spacer layers. The total period of each sample is different, indicating that the thicknesses are different. Simple simulations were carried out for these samples. The simulation of R450 is shown in Figure 7.12 (b).

Simple simulations show that the InAs layer thicknesses are modified. Only the non-annealed sample has a 3ML QD layer. The samples annealed at 350^0C and 580^0C have thinner QD layers, approximately 2-2.3 ML. The one annealed at 500^0C has the thickest layer, more than 3ML.

The samples are also measured with PL at 78K, as shown in Figure 7.13. The intensity of the non-annealed sample is beyond the limitation of our instrument. Its energy level is estimated to be 1.29 eV. The sample annealed under As_4 at 500^0C has the energy level of approximately 1.27 eV, the sample annealed at 580^0C has 1.21 eV, and the one at 350^0 has 1.16eV. The energy level shifted with different annealing conditions. As discussed in Section 7.2, the energy of the electrons within dots is related with the

dots' sizes. Larger diameter results in less energy. The dots size of non-annealed sample is the smallest one among these four samples, which thus has the highest energy. The one annealed at 350^0C processes largest dots, which has the lowest energy. The PL measurements are in good agreement with the AFM images. Therefore, the tuning of the wavelength of quantum dot photodetector can be realized by annealing the spacers under As_4 at different temperatures. The characterization data are all listed in Table 7.1.

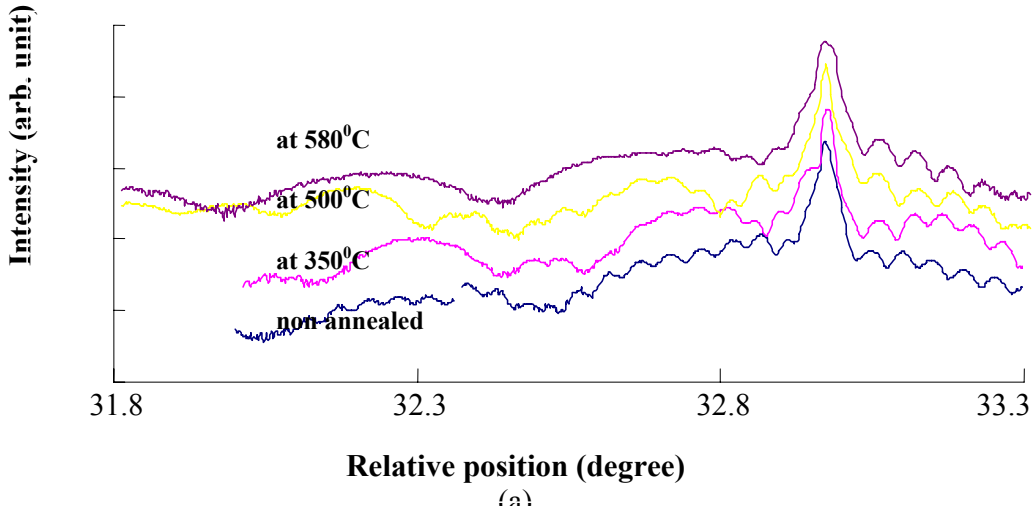

(a)

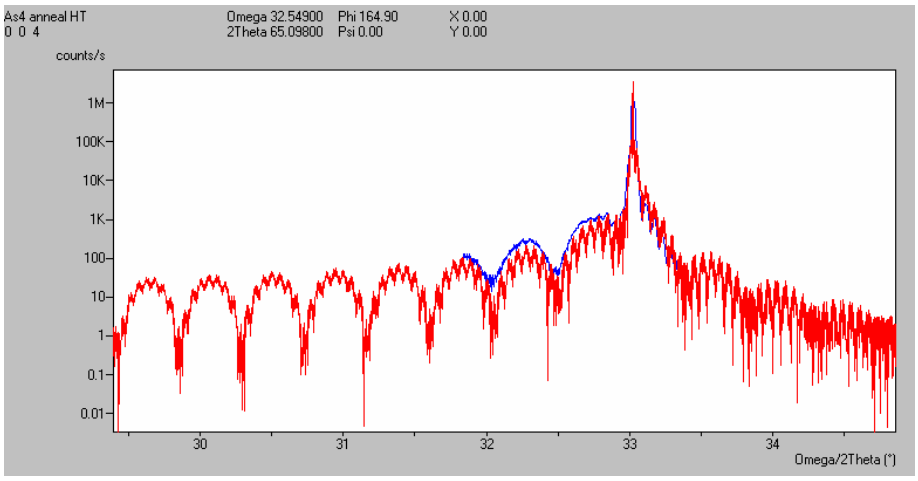

(b)

Figure 7.12 (a) ω-2θ x-ray scan of the samples with the spacer annealed under As_4, (b) simulation of one sample.

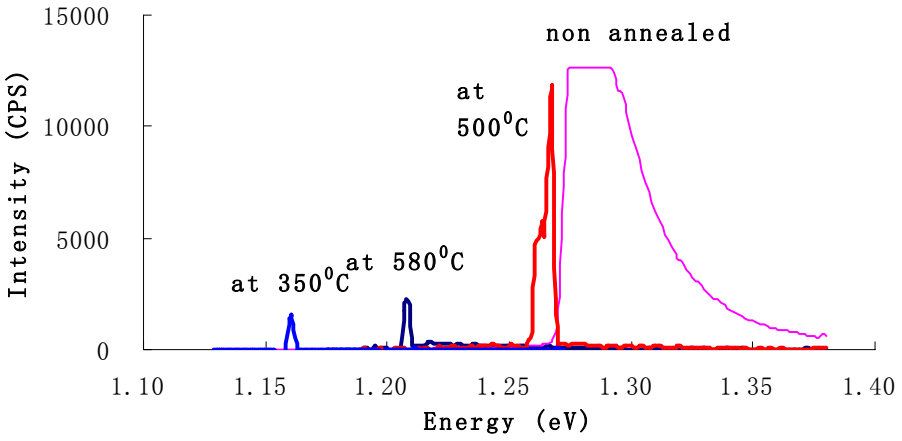

Figure 7.13 PL measurements of the samples, which are not annealed, or with spacer annealed under As_4 at 350^{0}C, 500^{0}C, and 580^{0}C.

TABLE 7.1 Summary of properties of sample with spacer annealed under As_4.

properties / Anneal condition	AFM		x-ray simulation	PL
	QD diameter(nm)	QD density (/μm^2)	QD layer thickness (nm)	Energy (eV)
non annealed	35	160	0.9	1.29
As_4 350 ^{0}C	50-100	90	0.75	1.16
As_4 500 ^{0}C	35-60	250	1	1.27
As_4 580 ^{0}C	30-60	60	0.7	1.21

7.6 Characterization of the Samples with Spacer Annealed Under P_2

AFM images of samples annealed under P_2 were shown in Figure 7.14.

Figure 7.14(a) is that of the InAs dots grown on the non-annealed spacer. The dots grown on the spacer annealed at 350^0C are shown in Figure 7.14 (b). The diameters are about 30-50 nm; with a dot density of $200/\mu m^2$. The sample annealed at 500^0C are shown in Figure 7.14 (c), with dots' sizes in the range of 30-50nm and dot density is about $35/\mu m^2$. The sample grown under P_2 at 580 ^{0}C was shown in Figure 7.14 (d).

The dot size distribution is shown in Figure 7.15. The one annealed at 580 ^{0}C is most uniformed. However, it is suspicious if the particles shown in the graph are real quantum dots. Another AFM picture scanned in a smaller range is shown in Figure 7.6 It is clearly shown that no coherent quantum dots are formed on the spacer annealed under P_2 at 580^0C. With increasing annealing temperature, fewer dots are formed. The dots' sizes of the sample annealed at 500^0C are mostly random.

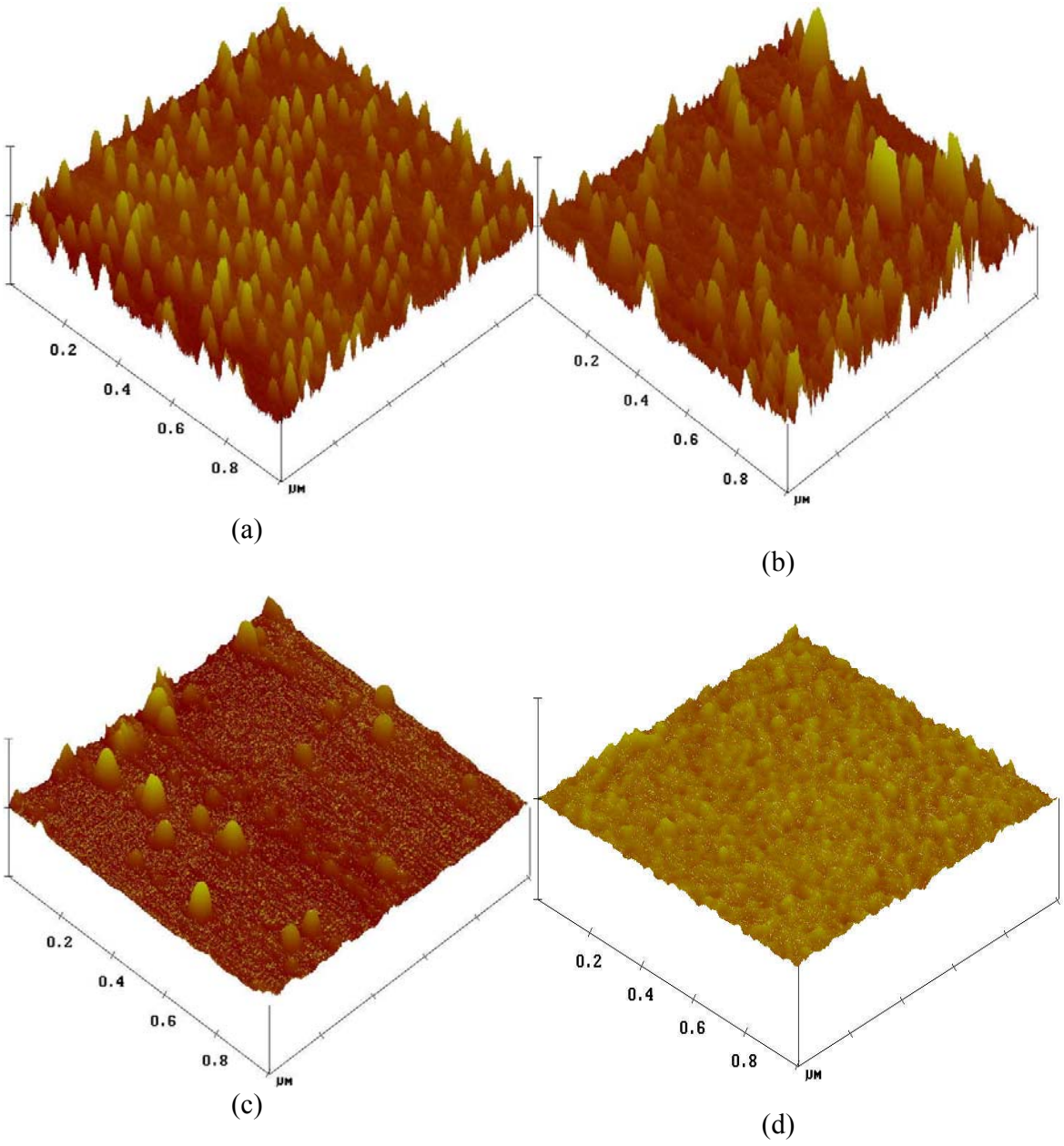

Figure 7.14. AFM pictures of quantum dots grown on the spacer, which was (a) non annealed, (b) annealed under P_2 at 350^0C, (c) at 500^0C, (d) and at 580^0C.

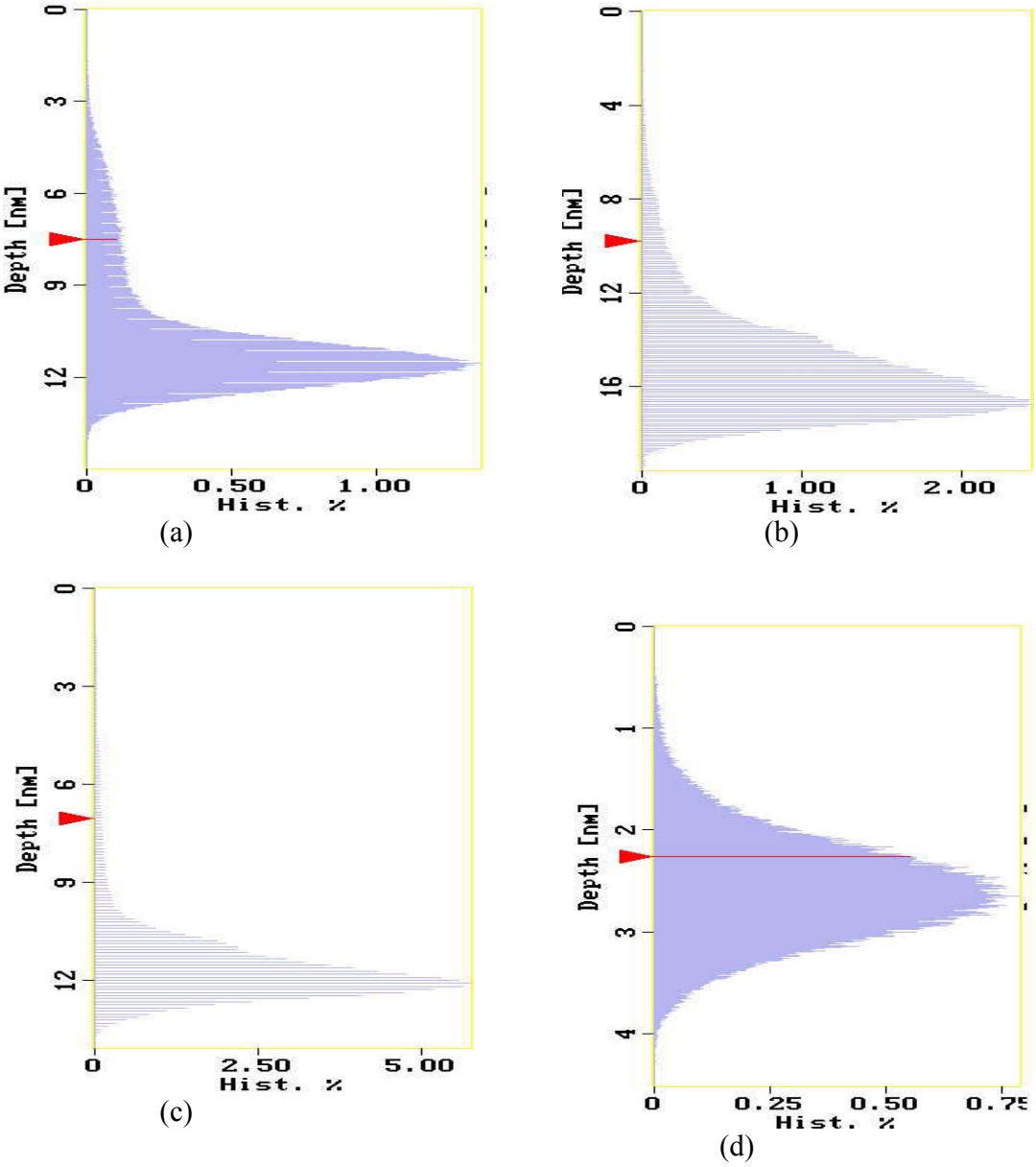

Figure 7.15 Dot size distribution, (a) non annealed, (b) annealed under P_2 at 350^0C, (c) at 500^0C, (d) at 580^0C.

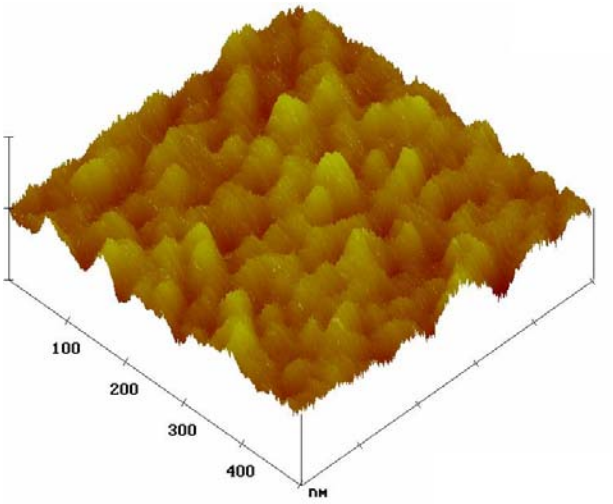

Figure 7.16 AFM pictures of quantum dots grown on the spacer, which was annealed under P_2 580^{0}C.

A P-for-As exchange reaction occurs when the spacer is annealed under P_2. The process is shown below [40]:

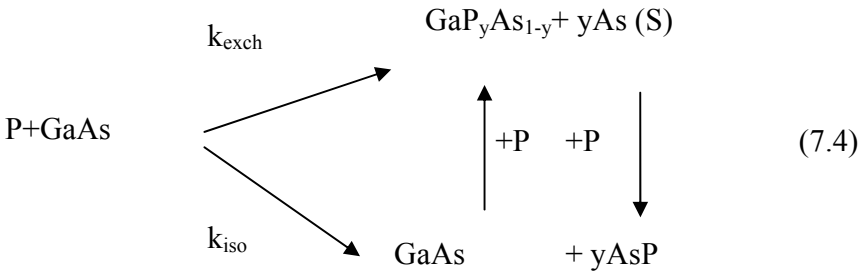

(7.4)

AsP does not aggregate because it has a high vapor pressure [41]; hence, the higher the surface temperature, the more desorption; but it acts as a sink for P that is scavenged to the exchange reaction P-for-As anion. Thus, this exchange reaction is thermodynamically favorable. The spacer was GaP_yAs_{1-y} instead of GaAs and the number

of y increased with increasing temperature. When InAs was grown on the spacer, some atoms were combined with P, so the alloy of InP_xAs_{1-x} was grown instead of InAs. Because the lattice constant of InP_xAs_{1-x} (5.8688Å for InP) are smaller than that of InAs (6.0590Å), the misfit energy is reduced, providing an additional driving force for the anion exchange reaction. The P-for-As exchange will prefer to occur along the island perimeter to reduce the energy barrier [42]. The exchange in the surface of the wetting layer increases its critical thickness. The reduction of the energy barrier and the increase of the critical thickness will decrease the stability of the islands, and enhance the mass transport from the islands to the wetting layer, leading to shrinkage of the islands. It has been found that during annealing, two opposite process occur simultaneously [3]. One is island coarsening via Ostwald ripening; the other is island shrinkage due to anion exchange.

At the early stage of annealing, coarsening dominates the whole process and hence the island size grows with annealing temperature (as shown in Figure 7.14 (c), annealed under P_2 at 500^0C). When higher temperature was applied, the degree of anion exchange will become so high, that the island will shrink until complete disappearance, as shown in Figure 7.14 (d), annealed under P_2 at 580^0C.

The phenomenon of surface exchange happened under P_2 anneal can be verified with x-ray scan. The (0004) ω-2θ scan was shown in Figure 7.17.

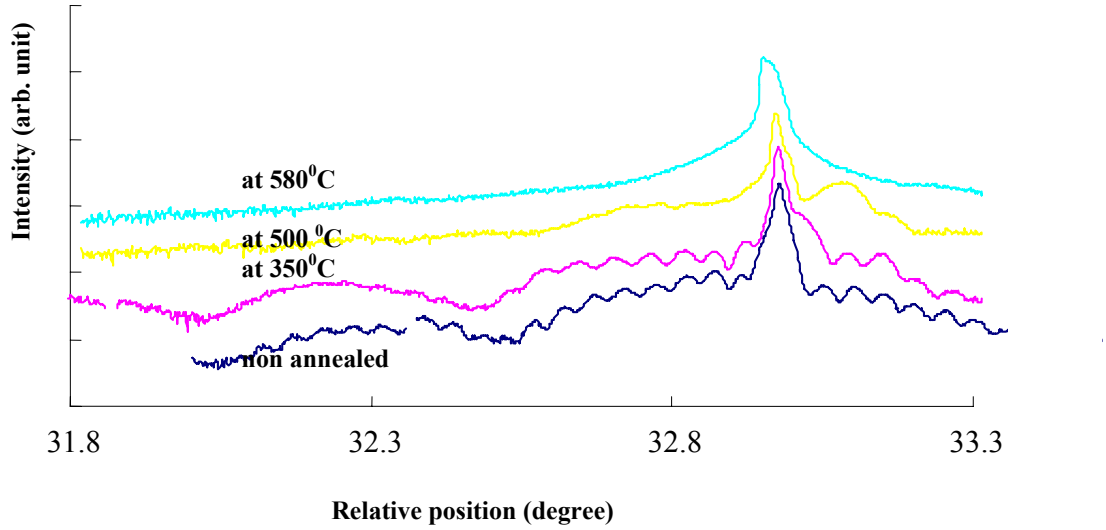

Figure 7.17. X-ray scan of QD samples with the spacer was annealed under P_2 at different temperature.

From the graph, when the samples are annealed under P_2 at the temperature above 500 ^{0}C, the fringes around the substrate peak disappear. That is because the lattice constant of GaP is 5.4505Å, that of GaAs is 5.6537 Å, and that of InP is 5.8688Å, the lattice constants of GaPAs and InPAs are similar to GaAs. It is hard to distinguish each single ultra-thin layer with the substrate. At higher annealing temperatures, more P atoms are exchanged with As. The result from the x-ray measurements is in good agreement with AFM images and our analysis.

PL measurements are shown in Figure 7.18. It can be seen that the peak position of the spacer annealed under P_2 at 350^{0}C is 1.21 eV, blue-shifted from the non-annealed sample. The PL of the sample annealed at 500^{0}C was a broad peak, indicating that the dots are randomly distributed in sizes. No strong signals were detected for the sample annealed at 580^{0}C since no coherent quantum dots are formed.

The PL measurements show that with the spacer annealed under P_2 at low temperature, the energy level did change to a position different from the non-annealed one. So the wavelength of a detector can be tuned by annealing under P_2 at low temperature.

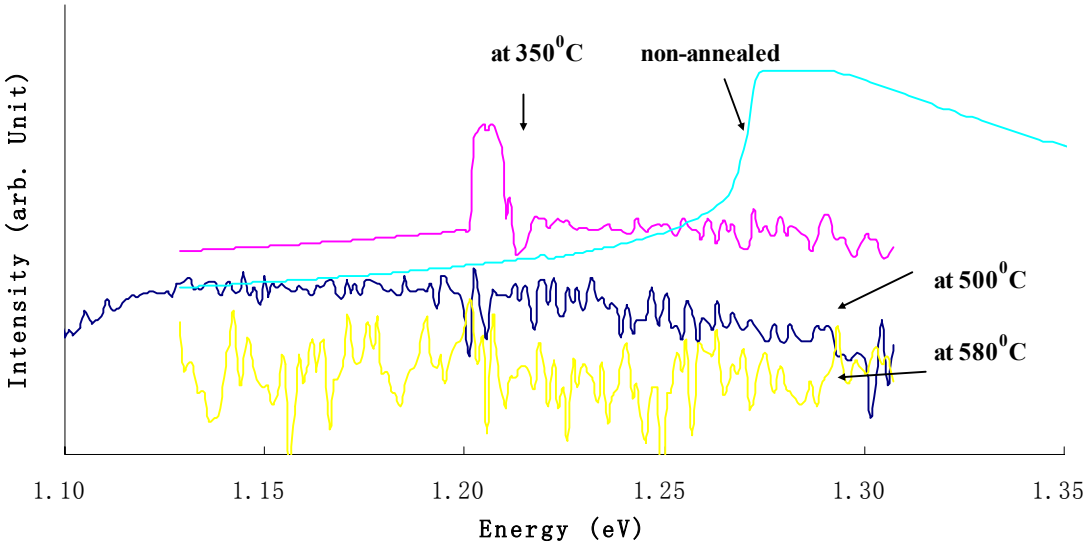

Figure 7.18 PL measurement of non annealed sample , the sample with spacer annealed under P_2 at 350^0C, 500^0C , and 580^0C.

TABLE 7.2 Summary of properties of sample with spacer annealed under P_2.

properties / Anneal condition	AFM		PL
	QD diameter(nm)	QD density (/μm^2)	Energy (eV)
non annealed	35	160	1.29
P_2 350 ^{0}C	30-50	200	1.21
P_2 500 ^{0}C	30-50	35	~1.20
P_2 580 ^{0}C	x	x	x

7.7 The Samples Grown with Current Block Layer

To study the current block layer, we grew the samples with an AlGaAs layer, which was non-annealed or annealed under different conditions. The material structure was shown in Figure 7.9. The spacers are all not annealed. The (0004) ω-2θ scan was shown in Figure 7.19.

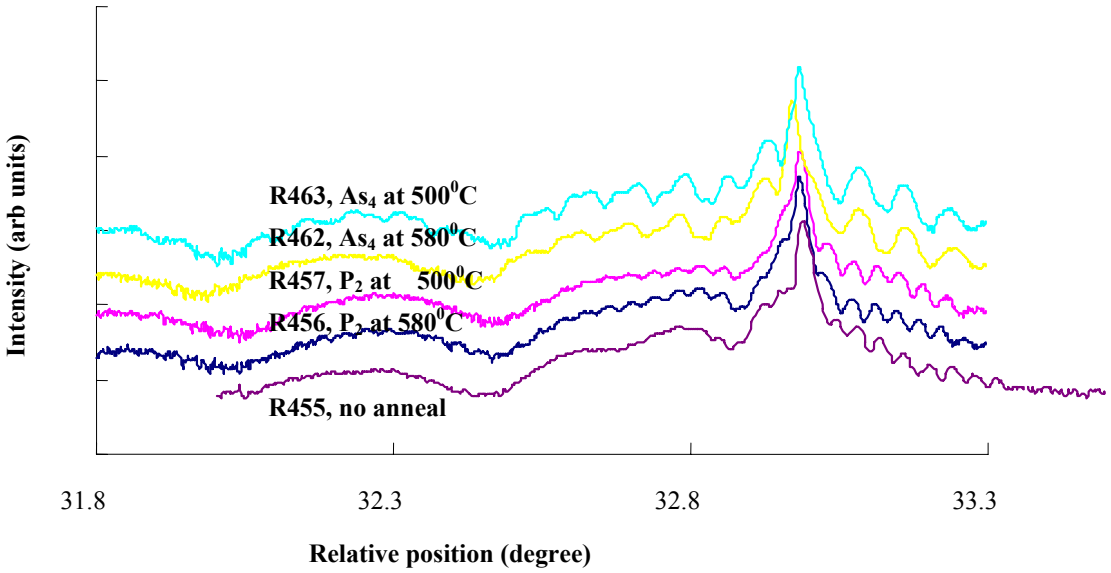

Figure 7.19 X-ray scan of the samples with the current block layer.

From the simulation, compared the samples of R463 and R462 with R455, the difference is that the strain of AlGaAs changed. The As_4 annealing relieves the strain within AlGaAs layer compared with the non-annealed sample.

The simulation of the samples of R457 and R456 showed that a layer of $Al_{0.3}Ga_{0.7}P_xAs_{1-x}$ was formed between AlGaAs and cap GaAs layer, indicating that

surface exchange happens with P_2 annealing. Higher temperature results in thicker AlGaPAs layer and larger value of x.

PL measurements are shown in Figure 7.20 The annealed samples are peaked approximately at the same position that is hardly distinguished from each other, at 1.21 eV. The peaks are blue-shift to the non-annealed one, which is 1.26 eV. The annealing on the AlGaAs layer changes the layer strains and affects the energy level of the quantum well. However, the energy level of the dots does not change much with different annealing conditions.

Compared to the PL measurement of the standard non annealed sample without the AlGaAs layer, which has the energy level of 1.29 eV, as mentioned in the previous two sections, the sample with insertion of an AlGaAs layer is blue shifted.

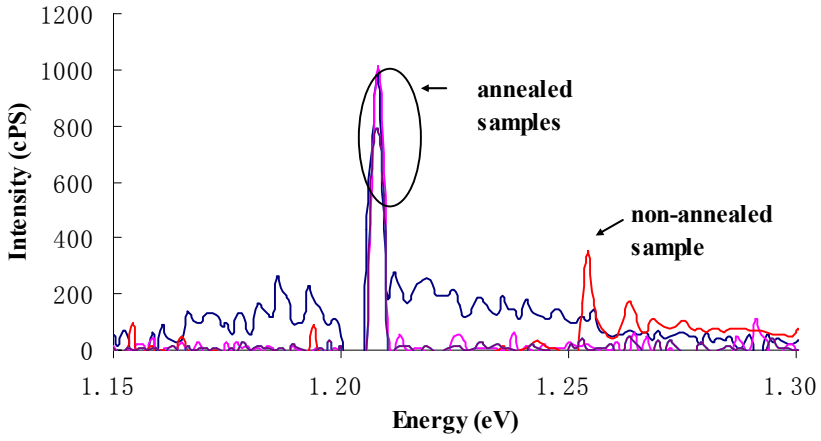

Figure 7.20 PL of the samples with AlGaAs layer annealed and non-annealed.

In summary, the size and density of self-assembled QD's is a very complex topic that up to today is not fully understood. The change in the dot size and density helps us to better understand the mechanism of dot formation.

The case of QD structure got involved with P_2 annealed is particularly complicated due to As/P exchange reactions. These exchange reactions means that, if an GaAs/AlGaAs surface is subjected to phosphors pressure at an elevated temperature (~500°C), As-atoms will be exchanged for P. When InAs layers were grown on such a surface, some P atoms will also react with InAs. High temperature results in more active P atom and more P/As exchange reactions, making the two layers are more lattice matched and fewer quantum dots are formed.

The As_4 annealing changes the InAs QD size, resulting changes in the electron energy. To tune the wavelength, anneal the spacer under As_4 at different temperature is efficient.

No research efforts report the integration of quantum dot photodetectors yet. For further research, different growth conditions resulting in changes in the energy are still our main focus.

7.8 References:

[1] D.A. Neamen, Semiconductor Physics and devices, Irwin, 1997.

[2] C. Weisbuch and B. Vinter. Quantum Semiconductor Structures. Academic Press Inc., San Diego, (1991).

[3] U. Meirav, and E. B. Foxman, Semicond. Sci. Technol. **11**, 255 (1996).

[4] R. NÄotzel, Semicond. Sci. Technol. **11**, 1365 (1992).

[5] D. Bimberg, M. Grundman and N.N. Ledentsov Growth, spectroscopy and laser application of self-ordered III-V quantum dots. MRS Bulletin February p. 31 (1998).

[6]V. A. Shchukin, N. N. Ledenstov, P. S. Kop'ev, and D. Bimberg, Phys. Rev. Lett., **75**, 2968, (1995).

[7] M. Tabuchi, S. Noda, A. Sasaki., S. Namba, C. Hamaguchi, and T. Ando, editors, Science and Technology of Mesoscopic Structures, Tokyo, Springe r-Verlag, (1992).

[8] D. Leonard, M. Krishnamurthy, C. M. Reaves, S. P. Denbaars, and P. M. Petroff, Appl. Phys. Lett., 63:3203, (1993).

[9] J.-Y. Marzin, J. M. Gerard, A. IzraÄel, D. Barrier, and G. Bastard. , Phys. Rev. Lett., **73**, 716, (1994).

[10] D. Bimberg, M. Grundmann, and N. N. Ledentsov, Quantum Dot Heterostructures. John Wiley & Sons, Chichester, (1999).

[11] J. J. Shen, "Heterogeneous Integration and the Exploitation of strain in MBE growth: Engineered Substrate, unpublished thesis, (2002).

[12] Y.Furukaawa, S.Noda, M. Ishii, A. Wakahara, and A. Sasaki, J. Electronic Mater. **28**, 452 (1999).

[13] M. Sugawara, editor. Self-Assembled InGaAs / GaAs Quantum Dots. Academic Press, San Diego, (1999).

[14] H. T. Dobbs, D. D. Vvedensky, Azangwill, J, Johansson, N. Carlsson, W. Seifert, Phys. Rev. Lett **79**, 897 (1997).

[15] S. Sauvage, P. Boucaud, J. M. Ge´rard, and V. Thierry-Mieg, Phys. Rev. B **58**, 10562 (1998).

[16] A. Weber, O. Gauthier-Lafaye, F. H. Julien, J. Brault, M. Gendry, Y. De´sieres, and T. Benyattou, Appl. Phys. Lett. **74**, 413 (1999).

[17] J. Phillips, P. Bhattacharya, S. W. Kennerly, D. W. Beekman, and M. Dutta, IEEE J. Quantum Electron. **35**, 936 (1999).

[18] S. Lin, Y. Tsai., and S. Chen, Jpn. J. Appl. Phys. **40** L 1290 (2001)

[19] D. Pan, E. Toweb, and S. Kennerly, Appl. Phys. Lett., **75**, 2719 (1999).

[20] J. L. Jimenez, L. R. C. Fonseca, D. J. Brady, J. P. Leburton, D. E. Wohlert and K. Y. Cheng, Appl. Phys. Lett. **71,** 3558 (1997).

[21] D. Pan, E. Toweb, and S. Kennerly, Appl. Phys. Lett., **73**, 1937, (1998).

[22] V. Ryzhii, J. Appl. Phys. **40**, L 148 (2001).

[23] A. D. Stiff-Roberts, S. Krishna, P. Bhattacharya, and S. Kennerly, J. Vac. Sci. Technol. B **20**, 1185 (2002).

[24] G. Destefanis, P. Audehert, E. Mottin, and P. Rambaud, *Proc. SPIE* **3061**, 111, (1997).

[25] Y. C. Cheng, C. M. Yang, W. H. Lan, J. N. Yang, and L. B. Chang, *Jpn. J. Appl.Phys.,* Part 1 **41** (part 1, 3A), 1386, (2002).

[26] T.C. Cheng, C. M. Yang, J. N. Yang, W. H Lan, L. B. Chang, and L. Z. Hsieh, Opt. Eng. **42** (1) 119, (2003).

[27] S. Krishna, O. Qasaimeh, P. Bhattacharya, P. McCann and K. Namjou, App. Phys. Lett, **76**, 3355, (2000).

[28] I. Vurgaftman, J.R. Meyer and L.R. Ram-Mohan, Band parameters for III-V compound semiconductors and their alloys. J. Appl. Phys.**89**, 5815, (2001).

[29] J. Maes, M. Hayne, V.V. Moshchalkov, A. Patane, M. Heini, L. Evaves, and P.C. Main, J. Appl. Phys., **81**, 1480 (2002).

[30] J.J. Shen, A.S. Brown, Y. Wang, and Z.L.Wang, J. Vac. Sci. Technol. B **19(4)**, 1463, (2001)

[31] F.Ferdos, S. Wang, Y. Wei, A. Larsson, M. Safeghi, and Q.zhao, Appl. Phy. Lett. **81**, 1195,(2002)

[32] K. M. Kim, Y.J. Park, Y. M. Park, C.K. Hyon, E.K. Kim, and J.H. Park, J. Appl. Phys., **92**, 5453, (2002),

[33] J. Brault, M. Gendry, G.Grenet, G. Hollinger, J.Olivares, B. Salem, T. Bentattou, and G. Bremond, J. Appl. Phys., **92**, 506, (2002).

[34] K. kamath, J. Philipps, h Jiang, J. Singh, and P. Bhatttacharya, Appl. Phys. Lett. **70**, 2952, (1997).

[35] Z. Ye, J. Campell, Z. Chen, E. Kim, and A. Madhukar, J. Appl. Phys., **92**, 7462, (2002).

[36] B. Ohnesorge, M. Albrecht, J. Oshinowo, A. Forchel, and Y. Arakawa. Phys.Rev. B, **54,** 11532, (1996).

[37] D.Pan, E. Towe, S. Kennerly, and M.Kong, Appl. Phys. Lett., **76**, 3537, (2000).

[38] A. D. Siff-Roberts, S. Krishna, P. Bhattacharya, and S. Kennerly, J. Vac. Sci. Technol., **B20**, 1185, (2002).

[39] N. Carlsson, K. Georgsson, L. Montelius, L. Samuelson, W. Seifert, and R. Wallenberg, J.cryst. Growth **156**, 23 (1995).

[40] Y.Furukaawa, S.Noda, M. Ishii, A. Wakahara, and A. Sasaki, J. Electronic Mater. **28**, 452 (1999).

[41] A.Brown, M. Losurdo, G. Bruno, T. Brown, and G. May, " A chemical and Kinetic Study of P-for-As Anion Exchange Reactions in GaAs/GaAsP superlattice structures, EMC conference, Salt Lake city, (2003).

[42] Y.Q. Wang, Z. L. Wang, T. Brown. A. Brown and G. May, *J. Cryst. Growth*, **242**, 5-14, (2002).

CHAPTER 8

CONCLUSION

In this thesis, three different photodetectors are designed and grown. They are important for different applications as described below.

GaN MSM photodetectors detect light in UV range. Our work concentrates on decreasing the defect density in the material and consequently dark currents in the devices. Because we use a near lattice-matched substrate, after optimization of the growth conditions, the defect densities in GaN grown on LGO is in the range of $10^7/cm^2$. The device grown on LGO has the dark current in the range of 10^{-12}A. Even after bonding and integration, the performance of the device did not degrade.

Due to the asymmetric structure of the substrate, asymmetric strains exit in the grown GaN film, making integration difficult. The strains analysis can be partially relieved by the growth of thick films (more than 1μm). The use of superlattices can stop substrate outdiffusion. However, it creates a more complicated strain profile. For thin GaN films, $Al_{0.12}GaN$ superlattice buffer would relieve the strain most, and for the thicker layers, the $Al_{0.44}GaN$ superlattice buffer relieves the strain most.

Further research is expected on this topic. The dislocation densities should be verified by TEM. It will be interesting to determine how the dislocation densities change before and after the film thickness has reached its critical thickness and with different Al composition.

InGaAs MSM PD has optoelectronic applications at wavelengths of 1.3 and 1.55 μm, and it is attractive due to the high speed. The challenge is to improve the speed of devices and maintain low dark current and high responsivity at the same time, which could be achieved by optimizing the material structure. Finally, devices were fabricated that achieve speeds as high as 50-70GHz, comparable with the commercial ultra-fast MSM.

In summary, GaN MSM and InGaAs MSM have similar process of integration, but the integration of InGaAs MSM is easier because all the layers are lattice matched. The asymmetric strains within GaN caused by the substrate make the integration more difficult. Two MSM detectors have applications at different wavelengths. Low noise is preferred for GaN MSM, and high speed and high responsivity are preferred for InGaAs MSM.

The research in this thesis related with quantum dot was to control the formation of the dots, and tune the wavelength of quantum dot photodetector. The wavelength of quantum dot photodetector is in the infrared (λ= 4-20μm) range of the optical spectrum. The function of growth condition on the wavelength was tested by PL characterization. It was found that the annealing under P_2 results in surface exchange, and the annealing under As_4 mostly changes dots' sizes, causing the changes of energy level.

Further experiments are expected on the fabrication, integration, and characterization of the devices.

V I T A

Sa Huang was born on September 25, 1974 in Tongliao, China. She graduated with her Bachelor degree in Electronics Engineering from Peking University in 1996. She went to University of Nebraska, Lincoln, from where she completed her Master degree in Physics in 1998. In 1999, she came to Georgia Institute of Technology, where she was under the direction of Dr. April S. Brown and Dr. Nan M. Jokerst. She received the degree of Doctor of Philosophy in Electrical and Computer Engineering in 2003. Her thesis work was entitled "GaN-Based and High-Speed Metal-Semiconductor-Metal Photodetector: Growth and Device Structures for Integration". Besides the research, she enjoys the family life with daughter and husband. Her interests include traveling, hiking, movie, reading, and cooking.